UNIVERSITY OF SOUTHAMPTON

Turbulence and Macro-turbulence in the Bottom Boundary Layer Downstream of Large-Scale Bedforms; Implications for Sediment Transport.

by

Magali Lecouturier
M.Sc, B.Eng

Submitted for the Degree of Doctor of Philosophy
in October 2000

School of Ocean and Earth Science

A mes parents, Elisabeth et Michel,
et à mes soeurs, Edwige et Valerie,

à qui je dois une ribambelle de souvenirs merveilleux,
et qui me donnent un bel ancrage dans cette vie.

The fish doesn't think, because the fish knows, everything.

(Goran Gregovic)

Abstract

Effects of large-scale topographic features on the benthic boundary layer (BBL) flow characteristics and on sediment transport are analysed in a natural shallow coastal site and in a laboratory flume. The main signature of flow/bedform interaction processes consists of large-scale flow structures, generated downstream of the bedforms; these are characterised by alternating modules of lower and higher streamwise speeds than the mean flow.

These structures modify the suspended sediment transport, generating high turbidity levels within macro-scale features of low flow speed, and the bedload transport, generating more frequent and larger bedload movements during macro-scale features of high flow speeds. These particularities result from variations in the turbulent bursting process within the macro-turbulence structures. Ejection events generate increases in suspended sediment concentration ; these are more frequent and more intense within the macro-scale structures of low flow speed. Sweeps are shown to generate most of the bedload transport ; these events are dominant and are magnified during modules of increasing horizontal velocity.

Enhanced (negative) contribution of outward and inward interaction events to the Reynolds stress, downstream of large-scale bedforms, compared to those reported for uniform BBLs, are observed in the field and laboratory investigations. This induces 'abnormally' low Reynolds stress values, which are believed to invalidate the use of the Reynolds stress parameter to predict sediment transport. Other aspects of the turbulence are little affected by the presence of bedforms upstream, such as the coupling between the turbulent velocities and the Reynolds stress, or, at the field site, the turbulent energy dissipation rate.

Acknowledgements

Michael Collins employed me for four years on European research projects, leading me to start a PhD in the second year. This provided me with more hard times and good moments, than I had hoped for. I thank him for entrusting me with these different tasks.

This thesis has been completed with the generous help of Carl Amos. I thank him warmly for his contagious motivation in research, for providing my last year income, and for supporting me in the new adventure opening in Rimouski. With her supportive and fighting attitude, Osanne Paireau has helped greatly in the last year: slaving in the laboratory, advising the writing up and providing general enthusiasm. Merci Osanne ! I thank Anthony Heathershaw for his very helpful advise in the organisation of this thesis and for his collaboration in the writing of a paper. I think dearly about the work done with John Davis, particularly on the sea campaign on the research vessels *Aegeo* and *Cote d'Aquitaine*. Kate Davis's talents have, once more, served me greatly in the preparation of the Figures.

I have shared some of the richest moments of my life with Stéphanie Retournay. Her unconventional outlook at life, has been of the best support in many aspects of my life. I address lots of love to my dear god-daughter Salomé Piatyszek, as well as my friend and her mum, Dominique Mathis. Alan Hughes, and his precious loving presence, Andreas Thurnherr, Luca Centurioni, Cristina Belpassi, Rob Potter and Dave Quick, have become particularly dear to me over these past years. The numerous office-mates who have passed through 164/21 over these 4 years (in particular Beth Greenaway), have provided much needed relaxation and fun moments in my working hours.

Contents

List of Figures

List of Tables

List of Annexes

Introduction

In marine environments with complex topography, the bottom flow may be subject to large three-dimensional distortions. The generation and the characteristics of the turbulence structures in such flows is subject to a plurality of mechanisms, such as mean current shear, flow vorticity in the wake of bedforms, kelvin-helmholtz instabilities at the free-shear layer interface, etc.. Few detailed studies have investigated the hydrodynamic mechanisms controlling sediment transport in such flows; it is generally assumed that the mechanisms are similar than the better-known processes over a flat bed. However, it is observed that most current numerical models, which are based on the theory of uniform two-dimensional flows over a flat bed, do not provide accurate predictions of sediment transport in flows over bedforms (McLean *et al.*, 1996). The insufficient precision of sediment transport models in flows over bedforms can be attributed to an inadequate representation of: (i) the turbulence structures and processes controlling sediment transport; and/or (ii) the relationships between the mean flow and the turbulence parameters (*e.g.* shear stress and mean flow speed); and/or (iii) the relationships between flow parameters and the sediment transport quantities (*e.g.* threshold of sediment movement and the Reynolds stress).

The aims of the present work are to undertake detailed experiments, in flows influenced by large-scale bedforms, in order to: (i) determine the hydrodynamic mechanisms controlling sediment transport; (ii) describe the detailed flow structures characterising the BBL downstream of bedforms and compare them with those over a flat bed; and (iii) investigate the validity of some of the assumptions made in sediment transport models. Large-scale bedforms considered in this work consist of isolated bedforms, which have a large height H compared to the water depth d ($H/d > 0.2$), such as sandbanks or estuarine bars. The measurements and data analysis concentrate upon: (i) the turbulence and macro-turbulence flow structures generated downstream of large-scale bedforms; (ii) the influence of the turbulence and macro-turbulence flow structures on the sediment dynamics; and (iii) the parameterisation of the turbulence and its scaling with the mean flow.

Two reasons motivated this work. Often hidden, turbulence is an ubiquitous and intriguing feature of the natural world, where it erodes the land and the ocean floor, slows down flows through its dissipative friction actions, and mixes and diffuses contaminants and heat. Its apparently chaotic and random nature contradicts with its intrinsic organisation and universal characteristics. The study responds also to a need of improving our predictions of sediment transport processes in the coastal zone, where increasing natural and human pressures are applied. This relies, partly, on a better understanding of processes occurring over topographic features, which often characterise the near-shore environment.

The thesis is organised into four Chapters. In Chapter 1, the general theory of uniform BBL turbulent flows is described. The information presented is used as a reference, for comparison with the observations collected in the present work. A review of the present knowledge on flow and sediment dynamics over large-scale bedforms is presented also in Chapter 1. Chapter 2 investigates data collected in a natural BBL of a shallow coastal region, downstream of sandbanks and sand-dunes. It aims at describing the natural processes occurring in environments of complex topography. Chapter 3 presents laboratory investigations, undertaken in open channel flow, over a single two-dimensional large-scale bedform. The objectives are to verify the processes observed *in situ* and to explore further the flow processes and sediment dynamics downstream of bedforms. In Chapter 4, the field and laboratory findings are synthesised and discussed. The implications of the findings for sediment transport modelling downstream of large-scale bedforms, are investigated in this last Chapter.

Chapter 1

Literature review: BBL flows and sediment transport

1.1 Definitions

1.1.1 Laminar and turbulent flows

A flow is laminar when the viscous forces are sufficient to dampen any irregular (turbulent) motions that may appear in the mean flow. Turbulence develops when the forces causing the flow exceed the viscous forces. This process results in the development of three-dimensional eddies, which move through the flow, creating a momentum exchange resistance which increases the total resistance to the forces causing the flow.

1.1.2 Benthic boundary layer

The benthic boundary layer (BBL) corresponds to the bottom layer of the water column influenced by bed frictional effects.

1.1.3 Large-scale bedforms

Large-scale bedforms refers to bedforms which have a large height compared to the flow depth. Large-scale bedforms disrupt deeply the mean flow structures throughout the BBL thickness and their effects onto the flow cannot be represented, as for small-scale bedforms (e.g. ripples), by an apparent bed roughness.

1.1.4 'Classic' flows

The term 'classic' BBL flows refers, in this thesis, to steady unidirectional flows over flat beds.

1.1.5 Reynolds number

The Reynolds number Re (Equation 1-1) expresses the balance between the inertia forces (mean flow velocity, U) and the viscous forces (ν) (Reynolds, 1883). Reynolds (*op. cit.*) found that turbulence appears without decaying rapidly, when the flow Reynolds number is above a critical value ($R_{e\,cr}$) of about 2000.

$$R_e = \frac{Ud}{\nu} \qquad \text{Equation 1-1}$$

where U is the mean flow speed in the pipe.

In BBL flows, the Reynolds number is expressed by replacing the water depth parameter d by the thickness of the BBL (δ). Reynolds numbers above about 10^4 characterise fully turbulent BBL flows (Stips *et al.*, 1998).

$$R_e = \frac{U\delta}{\nu}, \qquad \text{with } R_{e_{cr}} \approx 10{,}000 \qquad \text{Equation 1-2}$$

1.2 Theory of 'Classic' BBL flows

1.2.1 Mean flow structure

The mean flow structure of a classic BBL flow can be divided into a number of layers (Soulsby, 1983); these are presented in Figure 1-1 and are outlined below.

(i) A viscous sub-layer, which develops close to a smooth bed. In this region, the viscous forces are dominant. The flow velocity is determined entirely by the viscosity coefficient (ν) and the friction velocity u_* (Equation 1-3).

$$u(z) = u_*^2 z/\nu \qquad \text{Equation 1-3}$$

where $u_* = \sqrt{\tau_0/\rho}$ is the skin friction velocity, and

τ_0 is the bed shear stress

This layer disappears over rough beds.

(ii) A roughness sub-layer, which corresponds to the near-bed region influenced by the length-scales of the bed roughness. It extends about five times the height of the roughness elements.

(iii) A bottom logarithmic velocity layer, where turbulent processes resulting from the friction of the flow with the bed, dominate the dynamics of the flow. Within this layer, the mean horizontal velocity increases logarithmically with height above the bed (Equation 1-4) and depends only on the height above the bed, z, and the friction velocity u_*.

$$u = \frac{u_*}{\kappa}\log\left(\frac{z}{z_0}\right) \qquad \text{Equation 1-4}$$

where z_0 is the bed roughness length, and

κ is the von Karman constant; κ is usually assumed to be 0.41

The bottom part of this region is characterised by a Reynolds stress constant with height above the bed; this defines the constant stress layer (CSL). The turbulent motions in this layer are independent of the wall roughness, if the Reynolds number is sufficiently high ('wall similarity' hypothesis).

(iv) An outer layer, where the velocity is still controlled mainly by turbulent shearing, but where surface effects modify the mean and turbulent flow field. The velocity distribution in this region follows the velocity-defect law described by Prandtl (1925).

(v) A free-stream layer, where the current is not retarded by the bottom friction effect. In shallow (depth-limited) BBLs, this layer does not exist.

The thickness of a steady, unstratified and not depth-limited BBL lies within the range $(0.25 \text{ to } 0.40)u_*/f$ (where u_* is the friction velocity and f is the Coriolis frequency) (Blakadar and Tennekes, 1968). This layer extends usually throughout the water column in the coastal zone. In laboratory flumes, f can be neglected and the BBL thickness becomes a function of u_* and ν (kinematic viscosity). The thickness of the logarithmic layer is generally assumed to extend over 10 to 15 % of the BBL thickness δ (where δ = d, in depth-limited coastal zones) (Hinze, 1975; Tennekes, 1973). It can vary by an order of magnitude, depending upon the free-stream conditions (Soulsby, 1983).

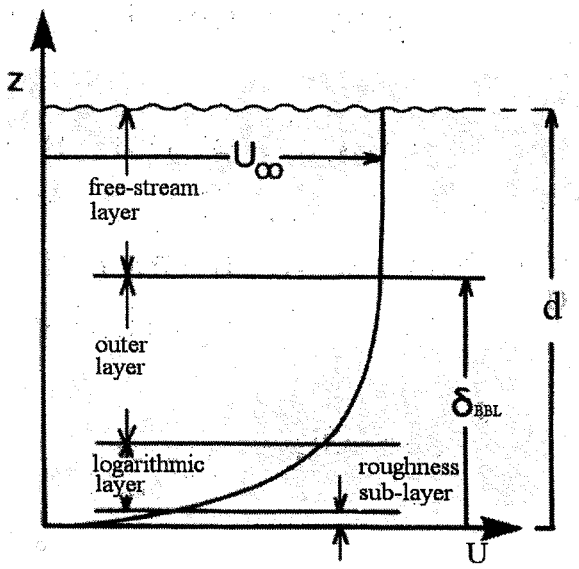

Figure 1-1: Vertical structure of a mean unidirectional flow over a level bed (from Soulsby, 1983).

1.2.2 Turbulence structures in 'classic' BBL flows

1) General turbulence processes

The friction of the flow with the bottom generates pressure instabilities. These results in small-scale coherent flow structures, or vortices, which are associated with irregular (turbulent) flow motions.

Over a smooth flat bed, the near-bed layer turbulence vortices form elongated streaky patterns of high-speed downward flows and low speed upward flows. The streaks were first described over smooth beds by Kline *et al.* (1967), using hydrogen bubbles as a flow tracer. Subsequently, Grass (1971) showed that these features are also present over hydrodynamically rough beds (Figure 1-2).

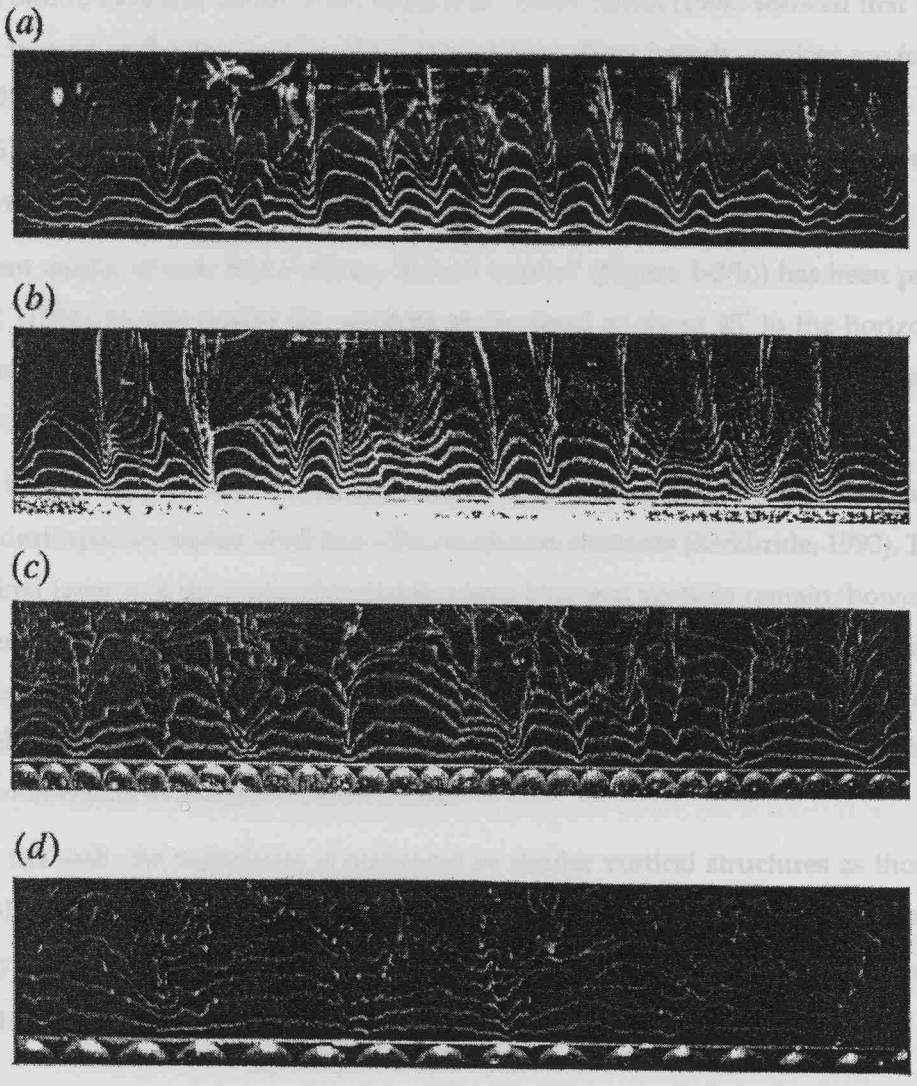

Figure 1-2: Streamwise vertical-view of the streaky organisation of the near-bed layer, over smooth to progressively rougher beds. The white streaks illustrate low-speed flow regions, visualised by hydrogen bubbles (from Grass *et al.*, 1991).

The precise nature of the vortices generating the near-bed streaky structures is still a matter of debate. Several authors have suggested that the streaky structure is generated by streamwise counter-rotating vortices (Blackwelder and Eckelman, 1979; Blackwelder, 1983). The dominant occurrence of quasi-streamwise vortices have been extensively observed, through measurements in real flows (*e.g.* Grass, 1971; Grass *et al.*, 1991) and, more recently, through numerical simulations (*e.g.* Jimenez and Moin, 1991; Robinson, 1991; Brooke and Hanratti, 1993; Bernard *et al.* 1993). Quasi-streamwise vortices are observed to originate close to the wall in response to intense spanwise shearing by pre-existing quasi-streamwise vortices through viscous/inviscid forces. The new vortices are counter-rotating to the parent ones; they are initially short and weak, but grow rapidly through stretching induced by the mean shear of the boundary layer flow.

It is now suggested widely that the near-bed vortices consist of hairpin vortices (Figure 1-3(a)), characterised by a 'horse-shoe-shape' head, and two long quasi-streamwise counter-rotating vortex legs, of usually different strengths (Smith *et al.*, 1991; Robinson, 1991; Grass *et al.*, 1991; Haidari and Smith, 1994 and Smith, 1996; Zhou *et al.*, 1999). Smith (1996) showed that streamwise vortices can be seen as the 'leg' section of hairpin vortices. New hairpin vortices are formed from low-speed fluid tongues, upwelled along the legs of hairpin vortices which are close to the wall (Smith, 1996). If the ejected 'tongue' is strong enough, it penetrates into higher regions of larger streamwise velocity and rolls up into a new hairpin vortex (Haidari and Smith, 1994).

A more recent model of near-bed vortices, 'funnel vortice' (Figure 1-3(b)) has been proposed by Kaftori *et al.* (1994). In this model, the vortices are inclined at about 45° to the horizontal plans, and have the shape of a spiral, whose transverse section increases as it develops away from the bed.

Over rough beds where the flow detaches from the roughness features, the near-bed layer streaky structure is destroyed by eddies shed from the roughness elements (Kirkbride, 1993). The vortices of the near-bed layer and the interaction mechanisms between vortices remain, however, similar to those over smooth beds. The main differences lie in: (i) the hairpin vortices being no longer the result of viscous/inviscid interactions with pre-existing vortices, but are shed from the bed roughness elements; (ii) the vortices, being larger and proportional to the bed roughness; and (iii) the overall momentum exchange being increased.

Away from the wall, the turbulence is organised in similar vortical structures as those found in the near-wall region. These structures are, however, more chaotic and are more broadly spaced ($\lambda u_*/\nu$ is, typically, between 600 and 1000 (Smith, 1993), instead of ~500 in the near wall region; where λ is the streamwise spacing between eddies).

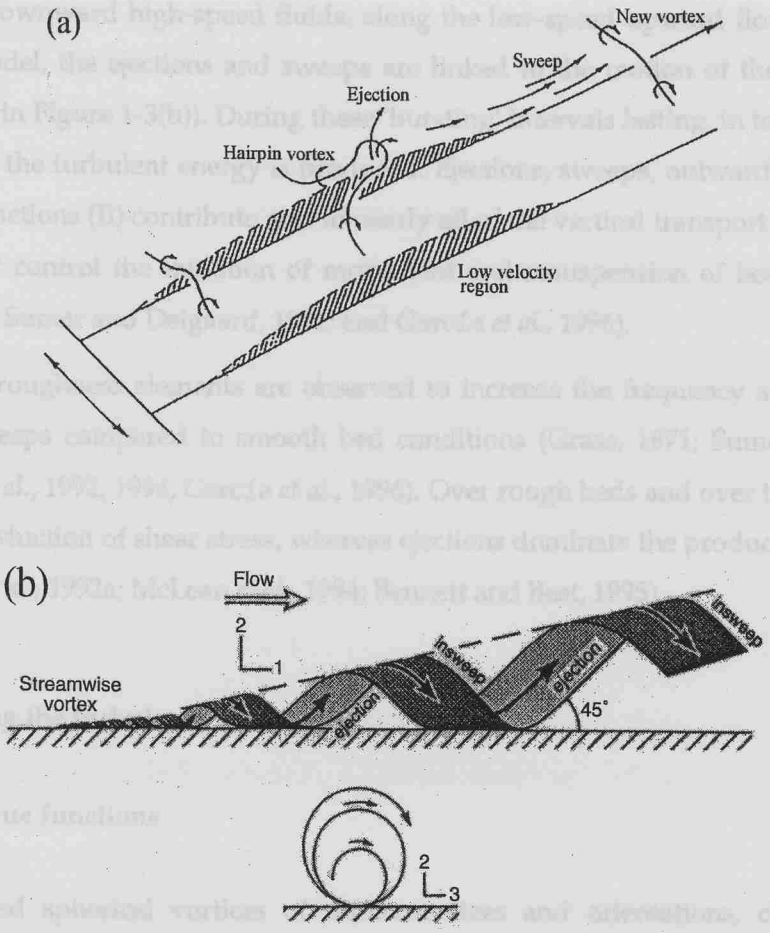

Figure 1-3: Proposed models of near-bed turbulence vortices: (a) hairpin vortex (from Sechet, 1996); (b) funnel vortex (from Kaftori *et al.* (1994)).

2) The bursting process

The period over which the flow is organised, as described above, corresponds to relatively quiescent moments. This structure is regularly, but briefly, disrupted by intervals during which strong turbulent motions are generated. Four types of motions are observed within these periods, which constitute the 'burst cycle' (defined originally by Kline *et al.* (1967)): ejections, characterised by a lower streamwise velocity than the mean flow speed ($u' < 0$) and an upward velocity ($w' > 0$); sweeps, characterised by $u' > 0$ and $w' < 0$; outward interactions, defined by $u' > 0$ and $w' > 0$; and inward interactions, characterised by $u' < 0$ and $w' < 0$. After these short interruptions, the near-bed layer recovers the streaky pattern.

The mechanisms generating the bursting events are not yet fully described; they appear to be related to the dynamics of the inner-layer vortices. Robinson *et al.* (1991a) and Bernard *et al.* (1993) have shown that sweeps and ejections are generated by the convection of vortices along the bed. Smith *et al.* (1991) have suggested that ejections correspond to the sudden 'break-down' of the upwelling (low streamwise speed water) tongues along the hairpin vortex legs, as they penetrate into the outer layer (Figure 1-3a). The sweeps, occurring just after the ejections, are regarded as

'compensating' downward high-speed fluids, along the low-speed upward flow regions. In the funnel-vortex model, the ejections and sweeps are linked to the motion of the fluid inside the vortex, as shown in Figure 1-3(b)). During these 'bursting' intervals lasting, in total, about 25% of the time, most of the turbulent energy is produced. Ejections, sweeps, outward interactions (OI) and inward interactions (II) contribute also to nearly all of the vertical transport of the mean flow momentum; they control the initiation of movement and resuspension of bed sediments (e.g. Sutherland, 1967; Sumer and Deigaard, 1981; and García *et al.*, 1996).

The presence of roughness elements are observed to increase the frequency and magnitude of ejections and sweeps compared to smooth bed conditions (Grass, 1971; Sumer and Deigaard, 1981; Krogstad *et al.*, 1992, 1994; García *et al.*, 1996). Over rough beds and over bedforms, sweeps dominate the production of shear stress, whereas ejections dominate the production over smooth beds (Krogstad *et al.*, 1992a; McLean *et al.*, 1994; Bennett and Best, 1995).

1.2.3 Measuring the turbulence structures

(i) Mean-value functions

The superimposed spherical vortices of different sizes and orientations, characterising the turbulence, are difficult to measure in their entirety. Analysis of the turbulence dynamics relies, mostly, on estimating initially the structures of the turbulent flow (*e.g.* symmetry in the shape) and then performing partial measurements of the turbulence (Townsend, 1976). The partial measurements of the turbulence include the estimation of mean-value functions, derived from high-frequency velocity records. These records provide one- or two-dimensional information on the spatial structure of turbulence and its evolution with time. The most commonly used mean-value functions are the correlation functions of velocity and the frequency energy distribution functions (also called energy spectra). The auto-correlation function of a velocity component u', $r_{u'u'}$ (Δt), describes the dependence of the values of a velocity component at one time t, on the values at another time t + Δt (where Δt is the time-lag between the two velocity measurements) (Equation 1-5).

$$r_{u'u'}(t) = \lim_{T\to\infty} \frac{1}{T}\int_0^T u'(t)u'(t+\Delta t)dt \qquad \text{Equation 1-5}$$

For a time-lag exceeding the time required for the eddy to travel across the measuring volume of the current-meter, the velocity values become statistically independent and $r_{u'u'}$ approaches zero. Eulerian time-scale (T) and length-scale (L) of the horizontal and vertical turbulent motions are, hence, defined using the auto-correlation functions of u' and w' respectively (Equation 1-6 to 1.9).

$$T_{u'} = \int_0^{\infty} r_{u'u'}(t)dt \quad ; \quad T_{w'} = \int_0^{\infty} r_{w'w'}(t)dt \qquad \text{Equations 1.6 and 1.7}$$

$$L_{u'} = T_{u'}\overline{U} \quad ; \quad L_{w'} = T_{w'}\overline{U} \qquad \text{Equations 1.8 and 1.9}$$

Energy spectra are useful for the analysis of the size-distribution of turbulent eddies. These functions express the amount of turbulent kinetic energy, contained within different frequency bands. The energy of u′(t) within the frequency band *df* is estimated by: (i) decomposing the time-series into its frequency components using a Fast Fourier Transform (Equation 1-10); and (ii) calculating the magnitude of the velocity squared within each frequency band, which is proportional to the energy in u′ (Equation 1-11). The energy spectrum has units of variance/frequency *i.e.* m^2/s.

$$u'(f) = \int_{-\infty}^{+\infty} u'(t)e^{-2\pi ift}dt \qquad \text{Equation 1-10}$$

$$E(f_i) = E([f_i, f_i + \Delta f]) = \int_{f_i}^{f_i+\Delta f} |u'(f)|^2 df \qquad \text{Equation 1-11}$$

The total energy contained in u′, v′ or w′ is obtained by integrating their energy spectra over the entire frequency range (0 Hz to F_N, where F_N = half the sampling frequency) (Parseval's theorem). This energy value corresponds also to the root-mean-square (rms) velocities (Equation 1-12 gives the example for u′) :

$$\left(\overline{u'^2}\right)^{1/2} = \left(\int_0^{F_N} S_{u'}(f)df\right)^{1/2} \qquad \text{Equation 1-12}$$

where $S_{u'}(f)$ is the frequency energy spectrum of u' and F_N is the Nyquist frequency (F_N = half the sampling frequency).

The total energy of the turbulence field $\overline{q^2}$ corresponds to the sum of the rms velocities (Equation 1-13). A total turbulent kinetic parameter TKE is also often used to express the energy in the turbulent velocity field (Equation 1-14).

$$\overline{q^2} = \overline{u'^2} + \overline{v'^2} + \overline{w'^2} \qquad \text{Equation 1-13}$$

$$TKE = 0.5\overline{q^2} \qquad \text{Equation 1-14}$$

Frequency energy spectra are converted into wavenumber spectra (energy versus wavenumber $k = 2\pi/\lambda$, where λ is a length-scale of turbulence), using Taylor's approximation of frozen turbulence (Section 1.3.1(5)). These spectra provide more direct information about the size distribution of the turbulence structures, than the frequency spectra .

(ii) Stationarity of the velocity signals

Mean-value functions of the velocity are representative of the turbulent velocity field, if the time-series are stationary *i.e.* if they do not include any mean trend (Bendat and Piersol, 1971). The length Δt of the records over which the quantities are averaged, must also exceed the time-scale of the turbulence, to include a statistically significant number of the Reynolds stress contributing events to be representative of the mean flow. Previous studies have shown that Δt is of the order of 8-12 min in tidal flows (*e.g.* Soulsby, 1980). Stationarity of the time-series can be tested by applying a *run test* on the rms velocities (Bendat and Piersol, 1971). This analysis determines the shortest record length where trends in the mean rms velocities are detected. Since any non-stationarity of interest is revealed by non-stationarity in the rms values (Bendat and Piersol, 1971), it is not necessary to test the stationarity of any other estimates.

(iii) Detection of the bursting events

The bursting events are detected in the velocity time-series using the method described in Soulsby (1983), based on the approach of Gordon and Witting (1977). This method selects the bursting events by retaining the most predominant peaks in the Reynolds stress time series, $-\rho u' w'_{peak_i}$, till their sum reaches 90% of the total Reynolds stress. The type of each selected event $-\rho u' w'_{peak_i}$ is determined from the sign of the u´ and w´ values; its duration is calculated by following the maximal $-\rho u' w'_{peak_i}$ value backward and forward in time, until the stress value decreases to 10 % of its peak value.

1.3 Typical properties of 'classic' flow parameters

1.3.1 Isotropy, equilibrium range and inertial sub-range

1) 'Gaussian' behaviour

In 'strictly' homogenous flows, the turbulent velocity magnitudes follow Normal (Gaussian) distributions, characteristics of random processes. Departures from the normal distribution are, however, an essential feature of turbulent motion (Townsend, 1976). Such departures can be expressed using the skewness and kurtosis parameters (Equations 1.15 to 1.18). The skewness reflects the asymmetry in the signal. It informs on the magnitude of the signal excursions from the local mean, and whether the excursions consist mainly in decreases or increases from the mean. A positive skewness means that large accelerations of the streamwise velocity, from the

local mean velocity are more frequent than large decelerations from the local mean. The kurtosis or flatness factor reflects the 'peakedness' in the velocity signal. It is related to the degree of intermittency in the turbulent velocity signal. The higher the kurtosis factor, the more intermittent and peaky the signal is. Typical skewness and kurtosis values for 'classic' flows are: $S_{u'} \sim S_{w'} \sim 0$ and $K_{u'} \sim K_{w'} \sim 3$; $S_{u'w'} = [-2.8 ; 0]$; $K_{u'w'} = [9 ; 12]$ (De Souza, 1995; Heathershaw, 1979).

$$S_{u'} = \frac{\overline{u'^3}}{\overline{u'^2}^{3/2}}, \qquad K_{u'} = \frac{\overline{u'^4}}{\left(\overline{u'^2}\right)^2} \qquad \text{Equations 1.15 and 1.16}$$

$$S_{u'w'} = \frac{\overline{(u'w')^3}}{\overline{(u'w')^2}^{3/2}}, \qquad K_{u'w'} = \frac{\overline{(u'w')^4}}{\left(\overline{(u'w')^2}\right)^2} \qquad \text{Equations 1.17 and 1.18}$$

2) Isotropic turbulence:

The hypothesis of local isotropy states that, at sufficiently high Reynolds number, the small-scale turbulence is independent of the large-scale flow structures and of the mean deformation rate (Kolmogorov, 1941, 1962). This hypothesis simplifies greatly the statistics and modelling of turbulence. In isotropic flows, the vertical, transverse and streamwise velocity spectra are related to each other, as in Equation 1-19:

$$E_{ww}(k)/E_{uu}(k) = E_{vv}(k)/E_{uu}(k) = 4/3 \qquad \text{Equation 1-19}$$

Various criteria have been proposed to test the isotropy of a flow, but no general agreement appears to exist on their validity (Mestayer, 1982; Saddoughi *et al.*, 1994).

$$\int E_{uw}(k_u)dk_u = -\overline{uw} = 0 \qquad \text{Equation 1-20}$$

$$R_{uw}(k_u) \equiv \frac{-E_{uw}(k_u)}{\left[E_{uu}(k_u)E_{ww}(k_u)\right]^{\frac{1}{2}}} \qquad \text{Equation 1-21}$$

Mestayer (1982) also questioned the existence of isotropic turbulence in boundary layer flows. He showed that turbulent boundary layers are isotropic only at scales smaller than 20 times the Kolmogorov micro-scale $\left(\eta \approx 0.27\times10^{-3}\ m\right)$. This result suggests that the commonly used assumption of Pond (1965), that turbulence is isotropic at wavenumbers $k > 2\pi/z$, is erroneous.

3) Equilibrium range:

Kolmogorov (1941) showed that the small eddies, which contain a negligible part of the turbulent energy, are in a state of absolute equilibrium *i.e.* the rate of receiving energy from the larger eddies equals the rate of energy loss to smaller eddies. At these scales, which define the equilibrium range, the rate of turbulent energy production P equals the rate of energy dissipation ε, except very close to the bottom wall, where P exceeds ε, and near the surface, where ε > P (Nakagawa and Nezu, 1975). The energy spectrum within the equilibrium range displays a 'universal' form .

4) Inertial sub-range:

If the Reynolds number of the flow is sufficiently large, there is a range of wavenumber within the equilibrium range where viscous dissipation is negligible. This range is called the inertial sub-range. Within the inertial sub-range, the energy spectrum of velocity takes the following ('universal') form:

$$E_{iii}(k) = \alpha_{iii}\varepsilon^{2/3}k^{-5/3} \qquad \text{Equation 1-22}$$

where $E_{iii}(k)$ is the three-dimensional spectrum of turbulent velocity,

α_{iii} is the three-dimensional Kolmogorov constant.

This expression may be separated into three expressions of the 1-dimensional spectra of the streamwise, cross-stream and vertical velocity fluctuations (Equation 1-23) :

$$E_i(k) = \alpha_i\varepsilon^{2/3}k^{-5/3} \qquad \text{Equation 1-23}$$

where i =1, 2 or 3 indicate the streamwise, cross-stream and vertical components respectively,

α_i is the 1-dimensional Kolmogorov constant. Note: Grant *et al.* (1962) measured α_1 in a tidal flow of very high Reynolds number (of order 10^6-10^7) and showed that α_1 = A×B, where A = 18/55 and B = 1.44. α_3 = 0.69 (Huntley, 1988).

The existence of a true inertial sub-range depends upon full separation of the scales at which turbulent energy is produced and of the scale at which energy is dissipated. The scale separation usually increases with the flow Reynolds number. Based upon field measurements of 1-dimensional horizontal velocity spectra in tidal flows, Gross and Nowell (1985) showed that the critical Reynolds number, above which an inertial sub-range exists, is around R_{ec} = 2500-3500. Corrsin (1958) proposed relationships between the time-scale (Equation 1-24) and length-scale (Equation 1-25) of energy production and dissipation, as conditions for the existence of an inertial sub-range. In these relationships, k_p may also be expressed using Equation 1-26 proposed by Soulsby (1983).

$$(\nu/\varepsilon)^{\frac{1}{2}} << |\partial U/\partial z|^{-1} \qquad \text{Equation 1-24}$$

$$k_d \approx 0.1k_\kappa >> k_p \approx |\partial U/\partial z|\left(\overline{u'^2}\right)^{-\frac{1}{2}} \qquad \text{Equation 1-25}$$

where $k_\kappa = 2\pi/\eta$ is the Kolmogorov wavenumber (η=0.27×10^{-3} m)

k_d is the dissipative wavenumber

k_p is the production wavenumber

$$k_p = \pi/z \qquad \text{Equation 1-26}$$

5) Taylor's hypothesis of 'frozen turbulence'

Taylor's hypothesis is used to derive wavenumber spectra from frequency spectra. In flows where the turbulence structures are advected past the sensor by the mean flow, much more rapidly than their rate of change, the frequency spectra can be converted into wavenumber spectra using Equation 1-27.

$$E(k) = E(f)\frac{U}{2\pi} \qquad \text{Equation 1-27}$$

Lumley (1965) and Wyngaard and Clifford (1977) showed that this hypothesis can be applied in shear flows, with only minor errors, if the turbulent velocities fluctuations are small compared to the mean velocity U (Equation 1-28).

$$\sqrt{u'^2}/U < 0.1 \qquad \text{Equation 1-28}$$

1.3.2 Horizontal and vertical turbulence intensities

Horizontal and vertical turbulent intensities, expressed as ratios of rms turbulent velocities to mean flow speed ($\sqrt{u'^2}/U$ and $\sqrt{w'^2}/U$), or as ratios of rms velocities to friction velocities ($\sqrt{u'^2}/u_*$ and $\sqrt{w'^2}/u_*$), are found to be similar in a variety of uniform marine and atmospheric BBL flows (Table 1-1). Soulsby (1983) suggested standard ratios for marine BBLs turbulence intensities (Equation 1-29)

$$\sqrt{\overline{u'^2}}/u_* : \sqrt{\overline{v'^2}}/u_* : \sqrt{\overline{w'^2}}/u_* = 2.4 : 1.9 : 1.2 \qquad \text{Equation 1-29}$$

The scaling of the turbulent velocities with the Reynolds stress friction velocity is assumed in numerical models. Models do not solve directly the turbulent motions but estimate, instead, the action of the turbulent velocity field (for example on the sediments), from the shear stress parameter (see Section 1.6.1) (Celik and Rodi, 1988).

1.3.3 Reynolds stress to turbulent kinetic energy ratio: $-\overline{u'w'}/\overline{q^2}$

In unidirectional BBL flows, the ratio of the Reynolds stress to total turbulent energy remains approximately constant. Soulsby (1983) suggested an averaged value for $-\overline{u'w'}/\overline{q^2} = 0.095$, from observations in different marine and atmospheric boundary layers. Townsend (1976) measured similar values in laboratory boundary layer flows, with high horizontal pressure gradient ($-\overline{u'w'}/\overline{q^2} \approx 0.08$). Much larger values were measured, however, in laboratory shearing flows

with a small pressure gradient $(-\overline{u'w'}/\overline{q^2} \approx 0.15)$ and in homogenous grid-turbulence $(-\overline{u'w'}/\overline{q^2} \approx 0.16)$ (Townsend, 1976). This ratio is used in the TKE method (Soulsby and Humphery, 1990) to estimate bed shear stress from the turbulence energy $\overline{q^2}$ (Section 1.5.2). It is also used in most turbulence closure schemes (such as the *k-ε* model), for the bottom boundary conditions of the turbulent kinetic energy and the energy dissipation rate parameters (Luyten *et al.*, 1996).

Authors & site description	z [cm]	U [cm/s]	$\sqrt{\overline{u'^2}}/u_*$	$\sqrt{\overline{w'^2}}/u_*$	$\sqrt{\overline{u'^2}}/U$	$\sqrt{\overline{w'^2}}/U$
Soulsby (1983) Standard BBL ratios	-	-	*2.3-2.6*	*1.2-1.5*	-	-
Bowden and Fairbairn (1952) : coarse-grained sand and gravel	0.75	0.28-0.50	-	-	0.102	0.065
Bowden (1962): firm sandy bottom, d=12-22 m	1.50-1.75	< 0.50	-	-	0.123	0.063
	1.00-1.25	< 0.50	-	-	0.119	0.068
	0.50-1.60	< 0.50	-	-	0.123	0.064
Bowden and Howe (1963) : coarse-grained sand and gravel	1.00	-	-	-	-	-
	0.50	-	-	-	-	-
Bowden and Howe (1963) : smooth mud, water depth 4-13 m	7-5	1.20	-	-	0.029	0.016
	1.25	0.61	-	-	0.057	0.029
	0.50		-	-	0.063	0.026
Soulsby (1977) : fine sand, d= 1.75 m	1.40	-	2.45	1.26	-	-
	0.30	-	2.70	1.52	-	-
Heathershaw (1979) : muddy sand to coarse gravel	1.50	1.00	-	-	0.13	0.060
	1.00	1.00	-	-	0.15	0.069
Soulsby (1981) : 1.5 km upstream of a 30 m high marine sandbank d=42m	0.65	-	2.27	1.21	-	-

Table 1-1 : Turbulent velocity intensities measured in various marine BBL flows at different heights z above the bed.

1.3.4 The Reynolds stress correlation coefficient $r_{u'w'}$

The value of $r_{u'w'}$ provides information about the spatial coherence in the velocity signal and, hence, about the strength of the turbulent eddies of the turbulence. Similar $r_{u'w'}$ values

characterise uniform shear flows. Gross and Nowell (1985) found that $r_{u'w'}$ varies between –0.40 and –0.30 in a variety of marine uniform BBLs. In homogenous grid-turbulence (which is characteristic of homogenous shear flows), Townsend (1976) measured $r_{u'w'}$ around -0.44

1.3.5 Typical length-scales of turbulence structures

The size reached by the turbulence eddies reflects the balance between the mean flow forces and the turbulence forces (eddies are generated through instabilities induced by the shearing of the mean flow and are dissipated through viscous forces). The eddy size controls the extent of vertical mixing (through the flow motions associated with the vortices). Measurements of velocity fluctuation spectra in shallow water BBLs have shown that the bulk of energy in vertical and horizontal motion and in the Reynolds stress, are contained within the following non-dimensional wavenumbers, k^* (where $k^* = k/z$) (Soulsby *et al.*, 1984; Heathershaw, 1979; Soulsby, 1977; and Bowden, 1962):

$$10^{-2} \leq k^*_{u'} \leq 10^{-1} \qquad \text{Equation 1-30}$$

$$10^{-1} \leq k^*_{w'} \leq 10^{2} \qquad \text{Equation 1-31}$$

$$10^{-2} \leq k^*_{u'w'} \leq 10^{1} \qquad \text{Equation 1-32}$$

where $k^*_{u'}$, $k^*_{w'}$ and $k^*_{u'w'}$ are the non-dimensional wavenumbers for the streamwise velocity, vertical velocity and Reynolds stress spectra, respectively.

Eulerian integral time-scales ($T_{u'}$ and $T_{w'}$) or length-scales ($L_{u'}$ and $L_{w'}$) of turbulence (Equations 1.6 and 1.9) are associated with typical values within marine BBL flows (Table 1-2).

Authors & site description	z (m)	U (m/s)	$L_{u'}$ (m)	$L_{w'}$ (m)
Bowden (1962): firm sandy bed, d=12-22m	0.50	0.2 –0.4	3.2	0.9
	0.75		3.6	1.3
	1.0		3.3	1.3
Bowden & Howe (1963): smooth mud, d = 8 m	0.50	0.5	3.8	1.1
	1.3	0.6	6.3	1.4
Heathershaw (1979): fine sand, d~50m	1	0.4	4.8	1.5
	1.5	0.5	7.1	2.1
Soulsby (1980): sand ripples	0.3	0.4	2.0	0.5
	1.4	0.5	4.5	0.8

Table 1-2: Eulerian integral length-scales, measured by various authors in marine BBLs, at different heights z above the bed.

1.3.6 Energy dissipation rate ε

The rate ε at which turbulent kinetic energy is dissipated through viscous forces can be derived from high-frequency measurements of velocity time-series, using the 'universal' expression of the velocity energy spectrum within the isotropic inertial sub-range (Equation 1-23). ε values measured near the bed in shallow marine environments are listed in Table 1-3.

Authors	Areas	z (m)	ε ($W.m^{-3}$)
Seitz (1962)	Stratified estuary	1.00	0.18×10^{-2}
Heathershaw (1979)	Irish Sea	1.00	6.3×10^{-2}
		1.50	5.7×10^{-2}
Simpson *et al.* (1996)	Mixed waters	near bed	10×10^{-2}
	Stratified waters	near bed	3×10^{-2}

Table 1-3: Energy dissipation rates measured within the bottom layer of shallow marine environments.

1.4 Flows over large-scale bedforms

Flows over bedforms are subject to forces which create mean flow non-uniformities, as follows: (i) the velocity streamlines are distorted under the influence of the horizontal pressure gradient, generated by the obstruction of the flow by the bedform; (ii) above a critical Reynolds number, the flow detaches from the crest of the bedform and evolves into a free-shear layers consisting of three-dimensional vortices (Figure 1-4); and (iii) the flow is retarded upstream of the bedform and is accelerated over the crest.

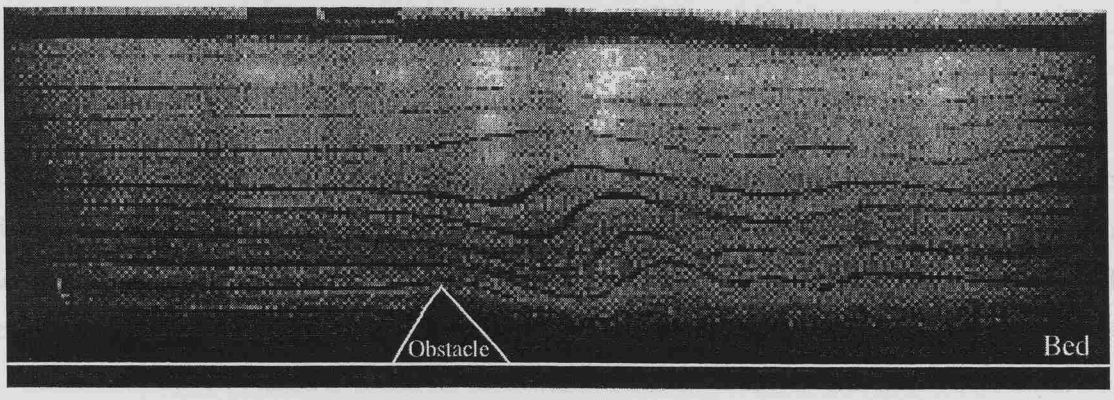

Figure 1-4: Free-shear layer propagating downstream of a bottom obstacle, as a result of flow separation over the crest. The flow streamlines, appearing in black, are visualised using a dye and a density-stratified water column (from Castro, 1987).

The turbulence structures are subject to complex and uneven strain in the 3 directions of space, which contrasts with the uniform horizontal shear experienced in 'classic' boundary layers. This is particularly the case for the large eddies, which are strained almost entirely by the mean flow gradients. These eddies contain most of the energy of the flow and control the development of the Reynolds stress (Townsend, 1980). Modification of their structures and intensities is expected to have important implications for the Reynolds stress modelling and, hence, for the predictions of sediment transport.

Most information about unidirectional flows over large-scale bedforms concerns the mean flow field and the macro-scale flow structures (such as the wake) (Lawrence, 1987; Nelson and Smith, 1989; Baetke *et al.*, 1990; Lamb, 1994; Knaap *et al.*, 1991; Wiberg and Nelson, 1992; Bennett and Best, 1993; Martinuzzi and Tropea, 1993). Much less data exist on the structure of the turbulence over bedforms. Nelson *et al.* (1993) observed that the turbulence in the wake of a bedform resembles the turbulence field in the wake of a sphere. It was found that the internal boundary layer developing downstream of the re-attachment point is strongly affected by the highly turbulent free-shear layer just above; it is characterised by different flow statistics than those found in 'classic' BBL flows. Maximum turbulence and shear stress occur in the overlying free-shear flow (where Kelvin-Helmhotz instabilities develop) (McLean *et al.*, 1994, 1996; Bennett and Best, 1995) and not near the bed, as in classic flows. Modification of the Reynolds stress has been observed over bedforms, with intensification in the outward and inward interaction events, compared to ejections and sweeps (McLean *et al.*, 1994; Nelson *et al.*, 1995). It was suggested that the flow recovers its 'free-stream' structure at distances more than 50 times the height of the obstacle, from the separation point (Bradshaw and Wong, 1972).

1.5 Sediment particle–turbulence interactions: hydrodynamic control of sediment transport

1.5.1 Modes of transport of sediments

(i) Bedload transport.

In this mode, the sediment particle motions are dominated by gravity forces and are in contact with the bed for most of the time. The particles move either by rolling, sliding or saltating along the bed. This mode of transport dominates the transport of sand material, under low to moderate flow regimes, and the transport of heavy particles (coarse sand, shingle...).

(ii) Transport in suspension.

Suspended transport occurs when the upward forces of the turbulent motions exceed the submerged weight of the particles. The suspended load contains mainly fine particles (which consists, typically, of material finer than 0.050 mm *i.e.* clay and silt) or loose organic aggregates. Sand particles can also be transported into suspension, usually intermittently, under active hydrodynamic conditions.

1.5.2 Sediment particle-turbulence interactions over a flat bed.

The fundamental role of turbulence vortical structures in the transport of sediments was speculated at an early stage. Sutherland (1967) first observed, in the laboratory, that the intermittent 'burst-like' motion of bed sediment grains, occurs in association with impinging eddies onto the bed (visualised using dye tracer). The role of near-bed turbulence vortices in entraining bed sediment was later supported by observations that sediments tend to form 'streamwise streaks' over a smooth bed; these 'mimic' the streaky structures of the near-bed layer (Figure 1-5) (Grass, 1971). The 'sediment streaks' are more stable than the flow streaks, and their span-wise spacing vary according to the size of the sediment grain (the finer the grains, the closer the streaks).

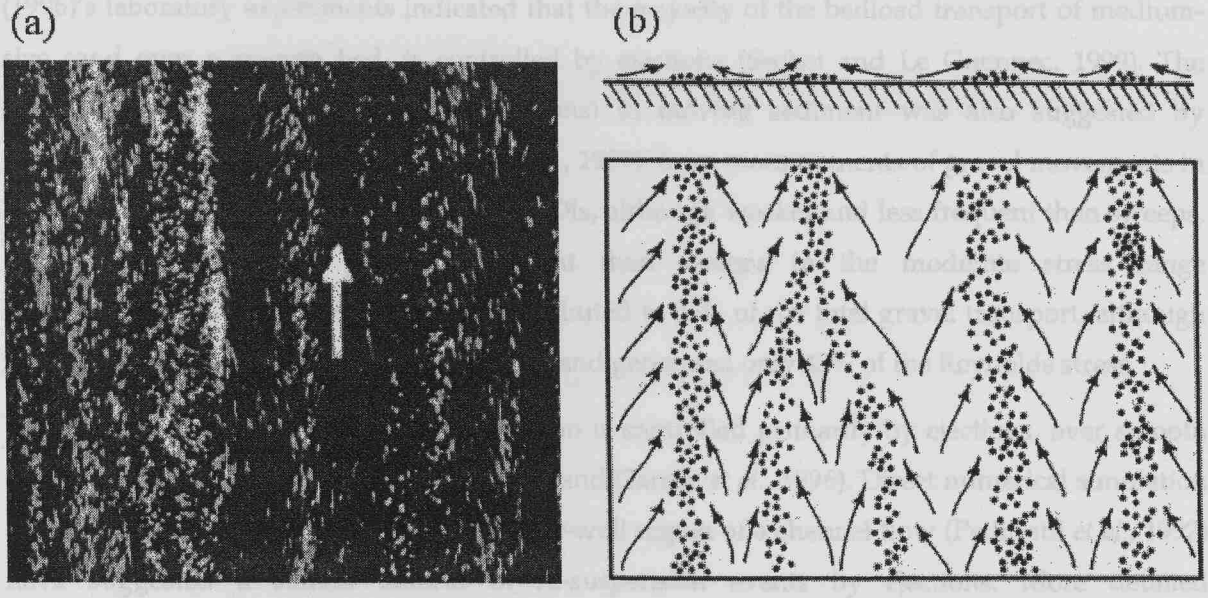

Figure 1-5: (a) Sediment longitudinal streaks formed over a smooth bed; (b) conceptual model of the action of sweeps, pushing the sediment aside, into regions of lower velocity (from Grass, 1971).

At high flow regimes or for large sediment grain sizes, the streamwise sediment streaks disappear and are replaced by span-wise irregularities, such as ripples (Williams and Kemp, 1971; Best, 1992). These new sediment formations reproduce, also, the turbulence structures of the

near-bed layer; this is dominated by wakes shed from the sediment grains (Kirbridge, 1993).

It is agreed generally that sediment transport is induced mainly by the bursting events generated by the near-bed vortices (Section 1.1.2), which induce intense and intermittent flow momentum transfer to the bed sediment. The type of bursting events controlling dominantly each sediment transport mode, are still a matter of debate and only few detailed studies have tried to resolve this problem. This omission is due, partly, to the difficulty of monitoring simultaneously the high frequency turbulence processes of the near-bed layer with the instantaneous bed sediment movements. Most results indicate that sweep events are the dominant mechanisms responsible for the rolling and sliding of grains. This hypothesis was first suggested by Grass (1971), based upon the observation of the movement of fine sand over a smooth boundary; this was fast in areas of high velocity inrush streaks (sweeps), and slow in areas of low-speed (ejection) streaks (Figure 1-5(b)). Yung *et al.* (1989) obtained similar results, using plexiglass particles. From the observation that the bedload movements were weakly related to ejection events, they concluded that the tangential force exerted during sweep events must be the principal factor of entrainment. Yung *et al.* (*op. cit.*) also observed that ejections are inefficient for particles whose diameter are smaller than the thickness of the viscous sub-layer; this point was contested later by García *et al.* (1996). Williams and Kemp (1971) observed that the first movements of sand on a flat bed, leading eventually to the formation of ripples, was induced by sweep impacts. Finally, Thorne *et al.* (1989) and Drake *et al.* (1988) found that bedload movements of gravel in a natural estuary and in a natural shallow stream, respectively, were related principally to sweeps. In contrast, Sechet (1996)'s laboratory experiments indicated that the majority of the bedload transport of medium-size sand over a smooth bed, is controlled by ejections (Sechet and Le Guennec, 1999). The significant role of OIs (outward interactions) in moving sediment was also suggested by (Heathershaw and Thorne, 1985; Thorne *et al.*, 1989), from measurements of gravel movements in a natural BBL. These authors observed that OIs, although weaker and less frequent than sweeps, generated even greater gravel movement than sweeps in the moderate stress range ($0 < |uw| < 0.04\ m^2.s^{-2}$). Sweeps and OIs contributed to 73% of the total gravel transport, although these 2 events occurred only 24% of the time and generated only 43% of the Reynolds stress.

It is thought that bed sediment re-suspension is controlled primarily by ejections, over smooth and rough beds (Sumer and Deigaard, 1989; and García *et al.*, 1996). Direct numerical simulation of particle-turbulence interactions in the near-wall region of a channel flow (Pedinotti *et al.*, 1992) have suggested a similar control of re-suspension events by ejections. More detailed measurements are required to confirm this hypothesis.

1.5.3 Particle-turbulence interactions in flows over bedforms:

Little information exists on sediment particle-turbulence in environments influenced by bedforms. McLean *et al.* (1996) measured, in the laboratory, sediment fluxes across a two-dimensional sandy dune embedded into a field of cement dunes. They found that 54% of sand bedload transport occurs during sweep events. Most results have shown an increased participation of OI events to bedload movements, compared to flat bed conditions. McLean *et al.* (1996) measured that 25% of sediment transport over two-dimensional dunes occur during OI events. Nelson *et al.* (1995) observed that the transport rates generated by sweeps and by OIs are approximately equal and are much higher than the rates generated by ejections or IIs. These investigators suggested that sweeps move more sediment than OIs only because they are more frequent. OIs appeared to be more effective close to the bottom obstacle whereas sweeps appeared to be more effective farther downstream.

The control of particle re-suspension by ejections over large-scale bedforms (as over flat bed) is suggested by some authors, from observations of high suspended sediment concentration associated with 'boils', which are dominated by ejection-flows (Grass, 1971; Jackson, 1976; Kostaschuk and Church, 1993). Bennett and Best (1995) have suggested that the increased participation of OIs within the separation zone and at and downstream of the re-attachment zone, may provide a mechanism by which sediment is eroded from the trough and the lower back face of dunes.

1.6 Parameters and assumptions in sediment transport modelling

1.6.1 Sediment transport equations

The transport of sediment in a marine system results essentially from: (i) advection of suspended sediment (SS), by the mean current; (ii) vertical migration of SS, by settling; (iii) dispersion of SS, by turbulence; and (iv) exchange of sediment at the bed sediment/water interface, by turbulence structures. These processes are expressed numerically in the advection-diffusion Equation (Equation 1-33) and in its boundary conditions (Equations 1-34 and 1-35).

$$\frac{dC}{dt} = U\frac{\partial C}{\partial x} - V\frac{\partial C}{\partial y} - W\frac{\partial C}{\partial z} \quad \text{... advection} \qquad \text{Equation 1-33}$$

$$-\frac{\partial W_s C}{\partial z} \quad \text{... settling}$$

$$+\frac{\partial}{\partial x}\left(\varepsilon_{sx}\,\partial C/\partial x\right) + +\frac{\partial}{\partial y}\left(\varepsilon_{sy}\,\partial C/\partial y\right) + \frac{\partial}{\partial z}\left(\varepsilon_{sz}\,\partial C/\partial z\right) \quad \text{... diffusion}$$

Boundary conditions:

$$\varepsilon_{sz}\frac{\partial c}{\partial z} = w_s c - E_S C_a \quad \text{at the bed} \qquad \text{Equation 1-34}$$

$$\varepsilon_{sz}\frac{\partial c}{\partial z} = w_s c \quad \text{at the surface} \qquad \text{Equation 1-35}$$

Where ε_{sx}, ε_{sy}, and ε_{sz}, = longitudinal, lateral and vertical sediment diffusion coefficients.

w_s is the settling velocity of the suspended sediment, which can be measured in the laboratory or be attributed an empirical expression.

$E_S = f(\tau_0)$ is the entrainment rate of bed sediment; it is a function of the bed shear stress (Lou *et al.*, 1999).

C_a is the near-bed suspended sediment concentration and must be estimated directly.

The resolution of this equation requires the resolution of the different flow parameters involved: U, V, W, ε_x, ε_y and ε_z and τ.

The mean flow field (U, V, W) is fully resolved using the equations of continuity, which express the conservation of mass (Elder and Williams, 1996). Numerical solutions to these equations exist for two-dimensional-shear flows as well as for more complex three-dimensional shear flows (Lawrence, 1987; Baetke *et al.*, 1990; Lamb, 1994). The main problem lies in the estimation of the turbulent eddy viscosity (discussed below).

The sediment diffusion coefficients are expressed usually as functions of the fluid eddy viscosity coefficient (*e.g.* Equation 1-36).

The eddy viscosity ε_f is derived from a turbulent closure scheme, since full resolution of the turbulence processes require too large an amount of computer time for the convenient use of models. Turbulent closure schemes reduce the number of equations describing the turbulent fluxes and simplifying their expression to algebraic forms. These schemes rely on 'universal' relationships between the turbulence parameters and the mean flow variables, or between the different turbulent quantities of 'classic' flows (Section 1.2.4).

$$\varepsilon_s = \beta\phi\varepsilon_f \quad \text{(van Rijn, 1993)} \qquad \text{Equation 1-36}$$

where β and ϕ are factors are to be determined experimentally.

β describes the difference between a 'fluid' particle and a sediment particle, and

ϕ expresses the influence of the sediment particles on the turbulence structure.

Different turbulence closure schemes have been proposed to solve the eddy viscosity coefficient ε_f (see reviews in Rodi (1984) and Luyten *et al.* (1996)). ε_f is expressed as a function of the turbulent kinetic energy and the turbulence length scale (for k-l closure schemes), or as a function of the

turbulent kinetic energy and the energy dissipation rate ε (for k-ε schemes).

The shear stress parameter τ is the parameter used to estimate the threshold conditions and the rates of deposition, bedload transport and re-suspension of sediments. Shields (1936)'s curves, modified Yalin (1972), are used widely to express the initiation of bedload transport, as a function of the critical bed shear τ_{cr}. Bagnold (1966) expressed the critical flow condition for re-suspension as a function of τ_{cr}. Different expressions of the rate of bedload transport and re-suspension, as a function of τ_{cr}, are also presented in van Rijn (1993).

1.6.2 Bed shear stress models

1) The Reynolds Stress method

The Reynolds stress method estimates the bed shear stress (τ_0) from the eddy-correlation technique (Equation 1-37). It uses simultaneous measurements of vertical and horizontal velocity components of the turbulent flow, within the constant stress layer.

$$\tau_0 = -\rho\left(\overline{u'w'}^2 + \overline{v'w'}^2\right)^{1/2} \qquad \text{Equation 1-37}$$

This method is the most direct way of estimating bed shear stress. Its main disadvantage lies in its sensitivity to mis-alignement of the current meter sensor axis with the true vertical axis (τ_0 varies of about 10% per degree of tilt (Soulsby, 1983)).

2) The Law of the Wall

In environments where the bottom layer is logarithmic, the bed friction velocity can be estimated by solving Equation 1-4, using mean horizontal velocities measured at a minimum of two heights z above the bottom. The proximity of the velocity profile to a logarithmic variation is quantified by the regression coefficient r^2 of the linear regression, between the straight line and the semi-logarithmic plot of log(z) against the measured velocity. The confidence in the estimation of u_* and z_0 depends on r^2, on the number of measurement points and on their spacing (Gross and Nowell, 1983; Grant *et al.*, 1984). The Law of the Wall relies on accurate determinations of the heights of the velocity measurements and of the magnitude of the mean horizontal velocities. The precise heights of the measurements may be difficult to estimate in eroding or depositing environments, or over small-scale bedforms. Applying the Law of the Wall over a rough bed, using velocity measurements in the upper region of the logarithmic layer (z > 1 m), can lead to large over-estimations of u_* (Chriss and Cadwell, 1984; Dewey *et al.*, 1988).

3) The Inertial Dissipation method

This method calculates τ_0 by expressing the balance between the rate of energy dissipation (ε) and the rate of energy production, in the equilibrium range (Equation 1-38).

$$-\rho\overline{u'w'}\frac{\partial u}{\partial z}=\varepsilon \qquad \text{Equation 1-38}$$

Since, in the constant stress layer, the Reynolds stress is equal to the bed stress τ_0, and $\partial u/\partial z = \tau_0^{1/2}/\kappa z$, Equation 38 reduces to:

$$\frac{\tau_0^{3/2}}{\kappa z}=\varepsilon \qquad \text{Equation 1-39}$$

In this Equation, ε is derived from the expression of the horizontal, or vertical, velocity spectrum in the inertial sub-range (Equation 1-23). The inertial dissipation method is convenient, since it requires only one point of measurement (for the estimation of ε) and is relatively insensitive to errors in sensor orientation and in mean flow measurement heights (Huntley, 1988). It relies, however, on: (a) the assumption that the energy production and dissipation at the measurement point balance each other; and (b) the existence of a true inertial sub-range, where the scales of energy dissipation are sufficiently separated from the scales of energy production. Therefore, the turbulence measurements must be made near enough to the bed to be within the constant stress layer, but far enough to produce an inertial sub-range. Sufficient scale separation occurs for Reynolds numbers above a critical value. Lumley (1972) observed that the critical Reynolds number lies in the range 2500-3500; Huntley (1988) found that full separation occurs only if $u_* > 0.8 \pm 0.2$ cm/s; and Gross and Nowell (1983) found a limiting u_* value of 2.0 cm/s. A modified version of the Inertial Dissipation method was proposed by Huntley (1988), to correct errors in τ_0 estimations resulting from measurements outside the inertial subrange.

4) Turbulent Kinetic Energy method

The TKE method (Soulsby and Humphery, 1990) is based on the similarity argument, which states that τ_0 is proportional to the turbulent kinetic energy TKE (Equation 1-40)

$$\tau_0 = 0.19\rho TKE \qquad \text{Equation 1-40}$$

1.6.3 Applications of models to flows over large-scale bedforms

'Universal' relationships between the flow parameters of classic flows, hold for a wide variety of flows, even those which are not strictly uniform or two-dimensional (*e.g.* tidal flows, flows over rough beds, combined current-wave flows). In cases of appreciable curvature of the mean

velocity streamline, however, the turbulence statistics differ significantly from that of 'classic' BBL flows. As such, the 'universal' expressions for turbulence may not be valid anymore.

Most available relationships between sediment transport rate and bed shear stress, in uniform flows, involve spatially-averaged parameters. These procedures are accurate over a flat bed, but lead to errors over bedforms, where the spatial and temporal variations in the flow characteristics become important. In such cases, it might be more appropriate to consider local and instantaneous bed shear stress in the prediction of transport rates. For these reasons, Williams *et al.* (1989) proposed an instantaneous bedload transport prediction method. However, Nelson *et al.* (1995) observed that such methods provide erroneous predictions too, because the model does not account for the non-linearity in the bed sediment response to the larger turbulence structures present downstream of bedforms: it was suggested that a 0.3 s long sweep event moves more sediment than 3 events, lasting 0.1 s.

Chapter 2

Field investigation: flow dynamics and sediment transport downstream of large-scale bedforms

2.1 General setting

2.1.1 Objectives

Measurements were collected in a shallow BBL (Figure 2-1), in the vicinity of large-scale bedforms, to investigate their effects on the flow dynamics and sediment transport. The objectives of this part of the research programme were:

(i) To characterise the flow structures and their influence on the suspended sediment, in natural BBLs influenced by large-scale bedforms.

(ii) To obtain *in situ* measurements of the turbulent parameters of the flow, used in numerical hydrodynamic and sediment transport models (*e.g.* turbulent closure schemes or bed shear stress estimation models).

(iii) To investigate whether the uniform BBL flow theory (Section 1.1) is valid in such environments, for predicting sediment transport.

The data presented in this chapter have been published in Lecouturier et al. (2000) (Annexe 1).

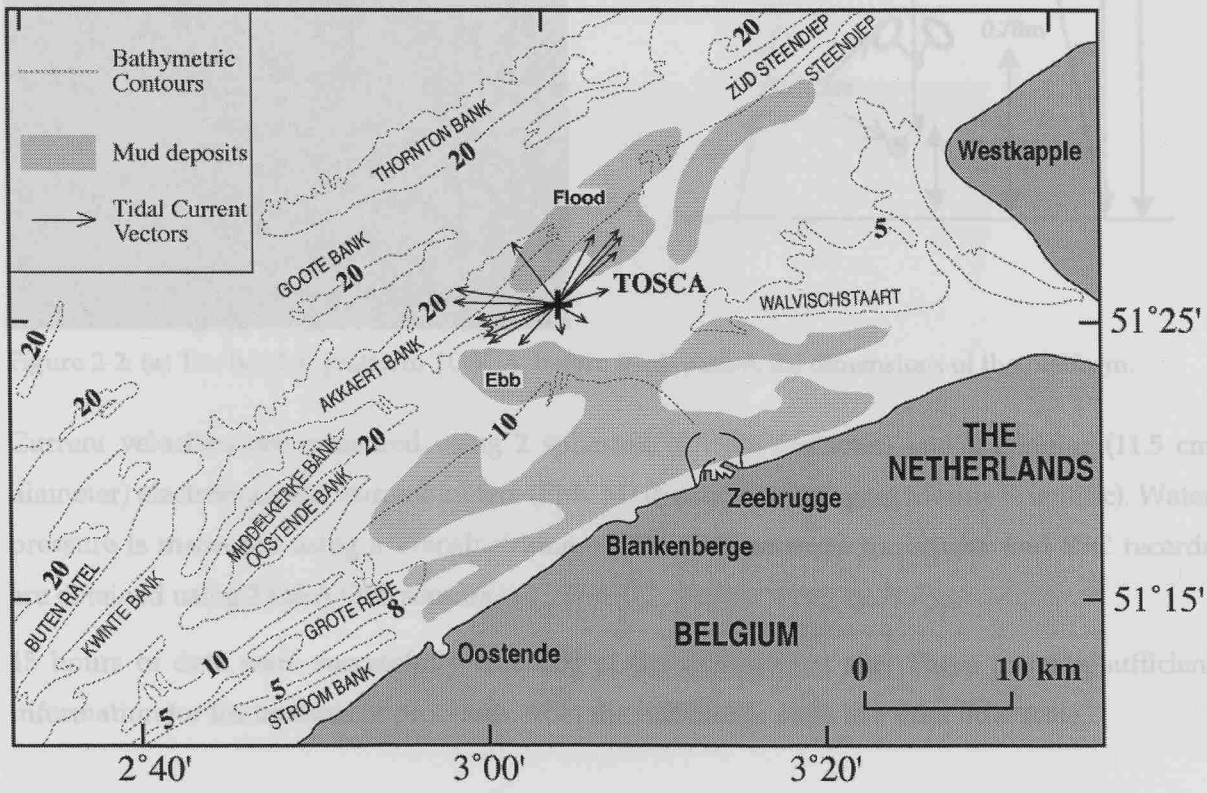

Figure 2-1: The study site offshore of the Belgium coast, near the Flemish bank system. The deployment site of TOSCA and the mean tidal currents measured over a full spring tidal cycle (on 7th Sept 94), are indicated.

2.1.2 Instrumentation and method

A benthic instrumented platform, TOSCA (Transport Of Sediment under the Combined Action of waves and currents) (Figure 2-2), was used to measure the mean and turbulent characteristics of the BBL flow. TOSCA records simultaneously and at 5-Hz, time-series of horizontal current velocity and direction at z = 0.35 m, 0.78 m and 1.20 m above the bed, of vertical current speed at z = 0.78 m, and of suspended sediment concentration (SSC) at all three heights. Simultaneous high-frequency measurements of water pressure are also obtained at z = 1.8 m above the bed. Sea surface elevation time-series (*i.e.* surface waves) are derived by correcting the water pressure records for depth attenuation, using the frequency-dependent correction of Earle and Bishop (1984). These measurements were collected by bursts of 30 min, at 30 min intervals for 15 hours.

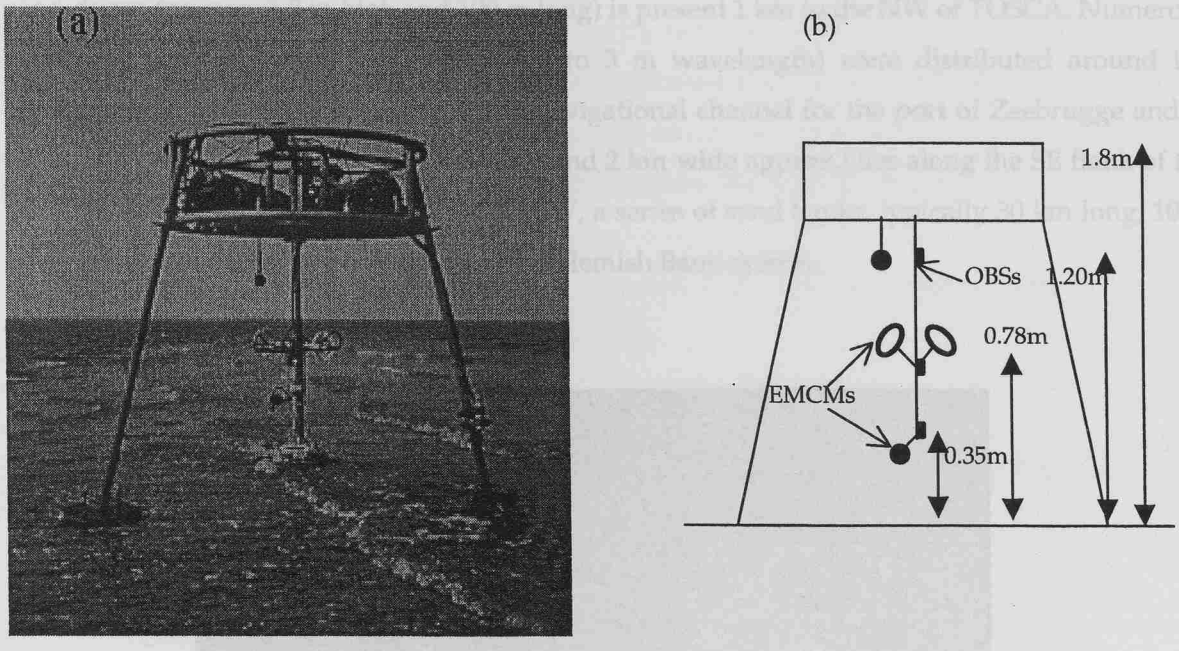

Figure 2-2: (a) The benthic platform TOSCA, before deployment; (b) dimensions of the platform.

Current velocities are measured using 2 spherical (5.5 cm diameter) and 2 annular (11.5 cm diameter) electromagnetic current meters (EMCM) (Series 800, Valeport Marine Scientific). Water pressure is measured using a TransInstrument BHL-4250 pressure transducer and SSC records are obtained using 3 D&A OBS sensors.

15 hours of data were successfully recorded at the deployment site. These provide sufficient information for the analysis of processes, from the turbulence scale to a tidal flow scale.

2.1.3 Study site

The area of investigation is located approximately 10 km offshore of the Belgian coastline, in the Flemish Bank area (Southern North Sea) (51° 25.81 N, 3° 5.02 E), in a mean water depth of 11 m (Figure 2-1). Grain size analysis of the upper 3 cm of Reineck box-cores collected at the TOSCA deployment site and at 1 km to the north, east, west and south of the site, reveal that the seabed consists of well sorted fine- to medium-size sand (median grain diameter of 0.220 mm). A detailed echo-sounder bathymetric survey, undertaken over an area of 3×9 km around the TOSCA site, and a side-scan survey, along three 1-km long N-S transects and separated by 150 m (side-scan sonar range), were carried out prior to the deployment of TOSCA. These surveys indicated that the seabed was locally flat, for an area of at least 250 m radius around the TOSCA site (Figure 2-3). Farther away, the seabed was covered by bedforms of various scales. A field of sand dunes (approx. 1.5 m high and 100 m long) is present 1 km to the NW of TOSCA. Numerous small bedforms (0.3 to 1 m high and 0.5 to 3 m wavelength) were distributed around the investigated site. 3 km to the south is the navigational channel for the port of Zeebrugge and 4 km to the W-NW, a large swale (13 m deep and 2 km wide approx.) lies along the SE flank of the Akkaert Bank (Figure 2-1). To the NW and W, a series of sand banks, typically 30 km long, 10 to 20 m in height and 1 to 2 km wide, form the Flemish Bank system.

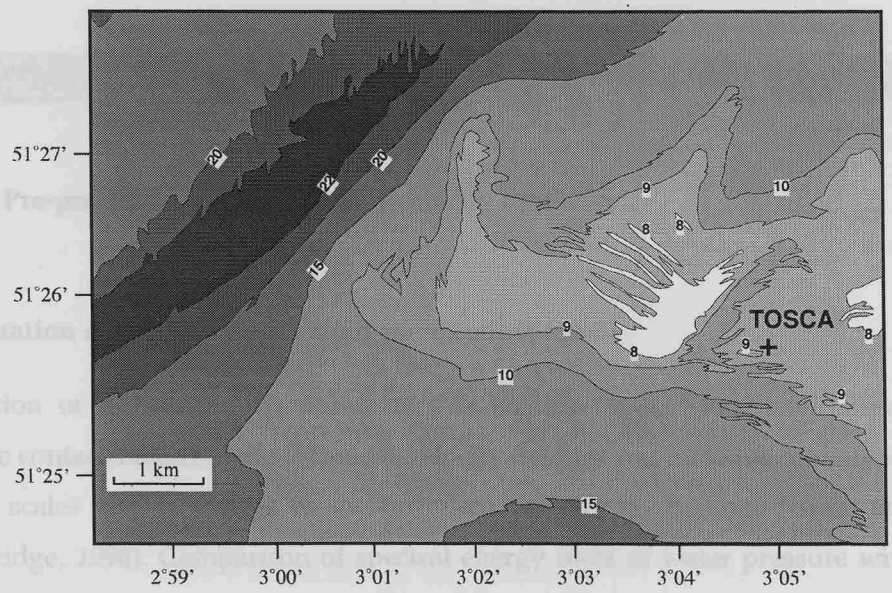

Figure 2-3: Detailed bathymetry (in meters) of the area surrounding TOSCA deployment site, based on an echo-sounder survey undertaken on 7th September 1994 (after Ministerie van de Vlaamse Gemeeschap, 1994).

Hydrodynamic models (O'Connor, 1996) and Synthetic Aperture Radar (SAR) images (Section 2.2.2) provide evidence that separation of the currents occurs over the bedforms of the area, during spring tides. These flow structures are thought to result in bedload and suspended

sediment transport patterns which are critical for the maintenance of the sandbanks (O'Connor, 1996).

2.1.4 Tidal and climate conditions

The deployment period of TOSCA occurred during a spring tide, with 5 m tidal range and currents reaching speeds of 0.70 ms^{-1} at 1.2 m above the bed. The wind was weak (~ 4.5 to 5 ms^{-1}) and blew seaward (180°N); thus the waves were generally small (significant wave height H_s < 0.40 m). The variation in mean water depth and in the mean current speed and SSC at all 3 heights, during the deployment period, are shown in Annexe 2. Detailed visual analysis of the SSC and velocity time-series showed that no significant resuspension of the underlying sandy sediment (*i.e.* above the height of the lowest suspended sediment concentration (SSC) measurements, at 0.35 m above the seabed) occurred during the deployment period. These measurements agree with the observations of Lanckneus and De Moor (1995), who found that, even during peak tidal flows, sand resuspension events are rare; when they occur, they are generally limited to heights of less than 0.15 m above the seabed. The tidal variation in SSC recorded by the OBS sensors (Annexe 2, Figure c) is believed to originate from the resuspension of adjacent muddy deposits, which are then advected across the measurement site, by the tidal currents (Grochowski, 1995; Lecouturier et al., 1998).

2.2 Results

2.2.1 Pre-processing of the SSC and velocity time-series

1) Filtration of the time-series from wave contributions

Estimation of turbulent flow parameters in shallow water shelf environments is subject to possible contamination of the turbulent velocity field by waves: wave orbital velocities may have similar scales and intensities as the turbulent velocity fluctuations (Grant and Madsen, 1986; Trowbridge, 1998). Comparison of spectral energy plots of water pressure with spectra of total velocity fluctuations (Figure 2-4) and of Reynolds stress for the Flemish Banks deployment (Figure 2-5), shows that energy in the turbulence velocity and Reynolds stress fields at the wave frequencies is small. The plots reveal a negligible contamination of the near-bed flow by waves.

A linear filtration technique (Thornton, 1979) was applied, nevertheless, to remove any wave contributions, before computing the turbulent parameters. This technique separates the total-velocity spectrum $E_U(f)$ into a turbulent $E_{u'}(f)$ and a wave-driven $E_{wave}(f)$ component, by using

co-located measurements of sea surface elevation (ξ) (or water pressure) and current velocity. The wave-component spectrum is defined as the part of the spectrum in coherence with the sea surface elevation fluctuations (Equation 2-1). The turbulent component is defined as the incoherent part; it is retrieved using Equation 2-2. These equations assume that waves approach the mean flow at right angles; this is the case during the flood phase of the tide. However, during the ebb phase, wave approach is around 45° to the current direction, for which the effectiveness of the filtration technique is probably limited.

$$E_{wave}(f) = \gamma^2_{U,\xi}(f) E_U(f) \qquad \text{Equation 2-1}$$

$$E_{u'}(f) = E_U(f) - E_{wave}(f) \qquad \text{Equation 2-2}$$

where $\gamma_{U,\xi}$ is the coherence function between ξ and U.

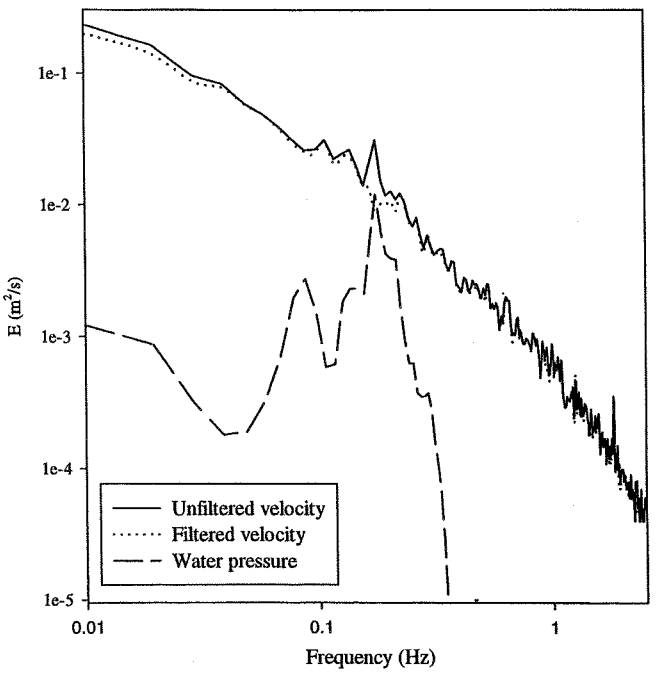

Figure 2-4: Energy spectra of total (unfiltered) and turbulent (wave-filtered) horizontal velocity fluctuations and of water pressure.

The dashed-line in Figure 2-3 illustrates the removal of the narrow wave-related energy peak in the velocity spectra, using this technique. The filtration of wave contributions removes about 9 % of the total turbulent kinetic energy (TKE) (which was about 32 $m.s^{-1}$ before filtration).

2) Stationarity of the time-series

The *run test* (Bendat and Piersol, 1971), described in Section 1.2.3, was used to determine the longest length of the stationary signals. The 30 min velocity records were divided into 30 s

intervals, over which the rms velocities are averaged. New time-series of 60 estimates, spanning a period of 30 min, were formed. The *run test* was applied then to sub-series of 5 to 30 min duration, using a 1 min step (adding 2 estimates at a time). The results of the test (Table 2-1) show that the shortest record length (Δt) to be non-stationary varied from 5 min to periods exceeding 30 min, but that most of the stationary record lengths exceed 10 min (in 35 cases out of 45). Based upon this analysis, the 30 min time-series were divided into 3 sub-series of 10 min, for the computation of the mean and turbulent parameters.

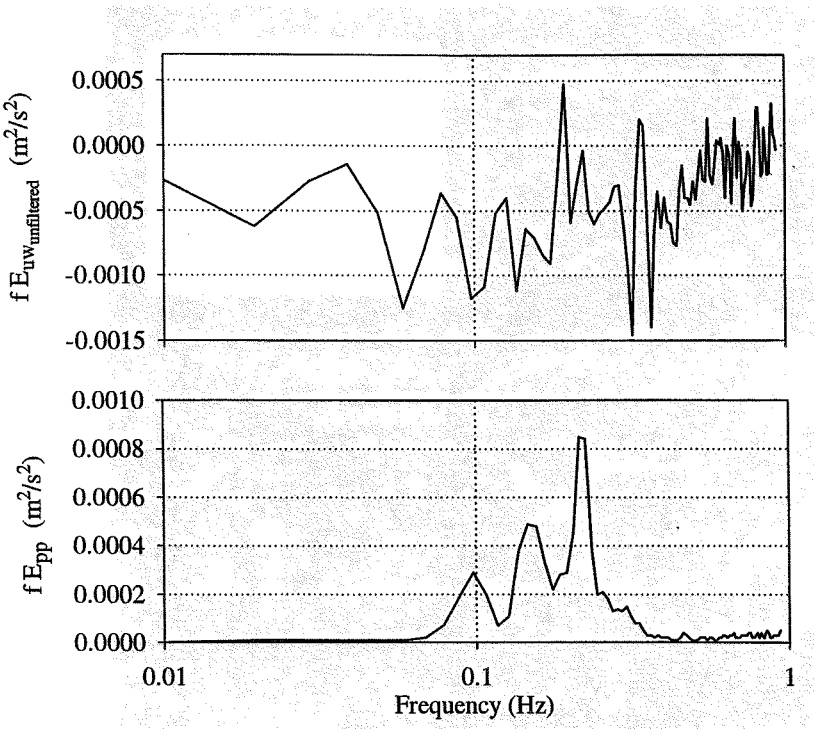

Figure 2-5: Energy spectra for (a) Reynolds stress; and (b) water pressure.

Burst no:		**1**	**2**	**3**	**4**	**5**	**6**	**7**	**8**	**9**	**10**	**11**	**12**	**13**	**14**	**15**
Z	**0.35**	>30	21	20	12	23	9	5	18	24	>30	9	14	20	13	>30
[m]	**0.78**	28	25	20	11	15	5	7	5	6	8	21	16	>30	13	15
	1.20	28	>30	14	11	15	13	5	19	6	>30	10	17	>30	24	>30

Table 2-1: Shortest non-stationary velocity record lengths, computed using the run test at 5% confidence level, for each burst and measuring heights.

2.2.2 Evidence of flow separation processes over bedforms

1) Sea surface signatures of flow interactions with topographic features

SAR images of the area around the deployment site (Figure 2-6) reveal the presence of sea surface signatures, as elongated white patches on the images, above and downstream of the sandbanks. These patches correspond to areas of enhanced back-scatter, which result from enhanced sea surface roughness. These features reveal that strong interaction processes are taking place between the tidal flow and the sandbanks. Such signatures are particularly evident during spring tides, as occurred during the experiment.

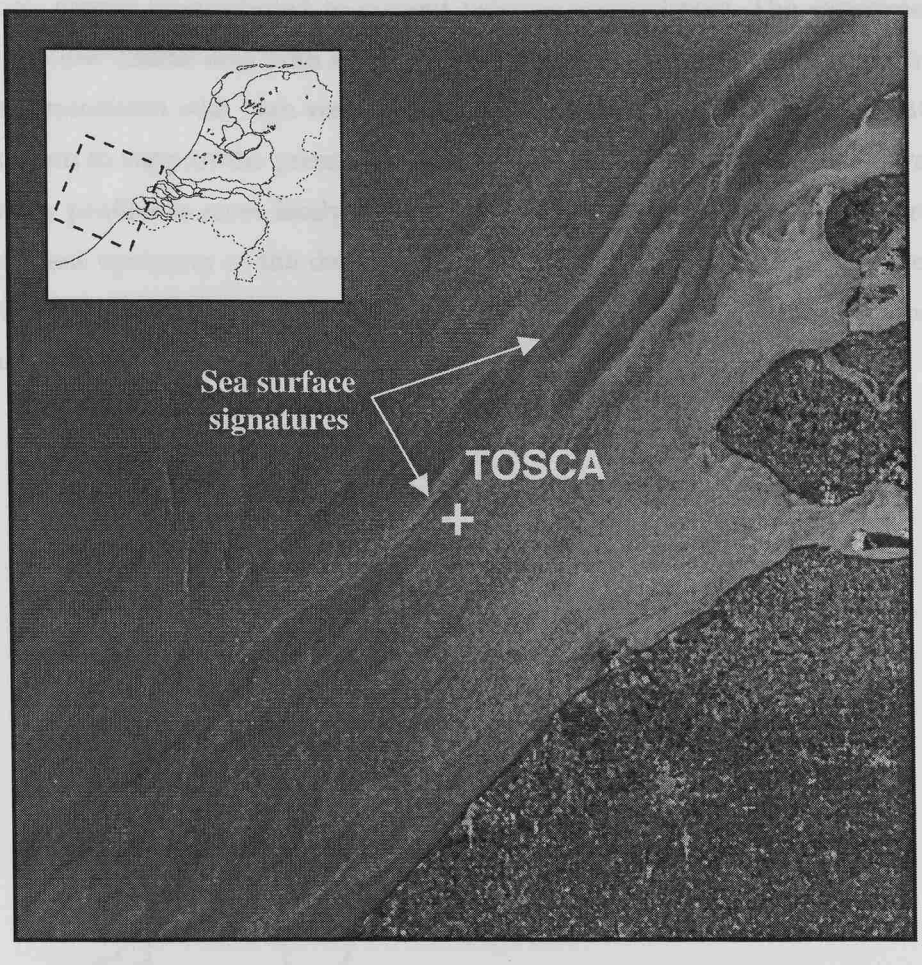

Figure 2-6: Synthetic Aperture Radar (SAR) image of the area around the experimental site (Orbit 1604, Frame 2565, Date 9/8/94), showing large-scale elongated sea surface signatures. The size of the image is 100 km by 100 km.

2) Vertical velocity structure

The vertical velocity profiles measured at the study site depart significantly from the logarithmic profile, during most of the tidal cycle. The variation in the mean vertical velocity profile throughout the tidal cycle is shown in Annexe 3. When the current flowed towards the NW-SW sector (over approximately 50 % of the time, Figure 2-1), the velocity profiles displayed a

downward curvature, when plotted on a semi-logarithmic graph of log z versus U(z) (Figure 2-7). On a few occasions (about 20 % of the time), when the current flowed towards the opposite direction (E-NE), the velocity profile displayed an upward curvature. Non-logarithmic velocity profiles occur for a variety of reasons : (i) unsteadiness in the flow velocity (Soulsby and Dyer, 1981); (ii) the presence of internal waves (Adams *et al.*, 1990); (iii) flow stratification (Green *et al.*, 1990); (iv) heterogeneous distribution of bottom roughness (Paola, 1985; Heathershaw and Langhorne, 1988); or (v) the presence of large bedforms, associated with flow separation and eddy shedding (Hoerner, 1965; Adams *et al.*, 1981). Downward curvature in the vertical velocity profiles was observed here during both the accelerating and decelerating phases of the tidal flow and, therefore, cannot be attributed to current velocity unsteadiness. The experimental site is located in a shallow coastal area with strong tidal currents and no major freshwater inputs. Such conditions are associated with high vertical mixing which do not allow sufficient stratification of the water column to support the presence of internal waves. Consequently, the curvature in the vertical velocity profiles is more likely to have resulted from flow separation effects over large bedforms, present upstream of the deployment site. As the flow separates from the bedforms, large-scale vortices are shed and disrupt the structure of the BBL. Such vortices can propagate to large distances downstream of bedforms (Section 1.3).

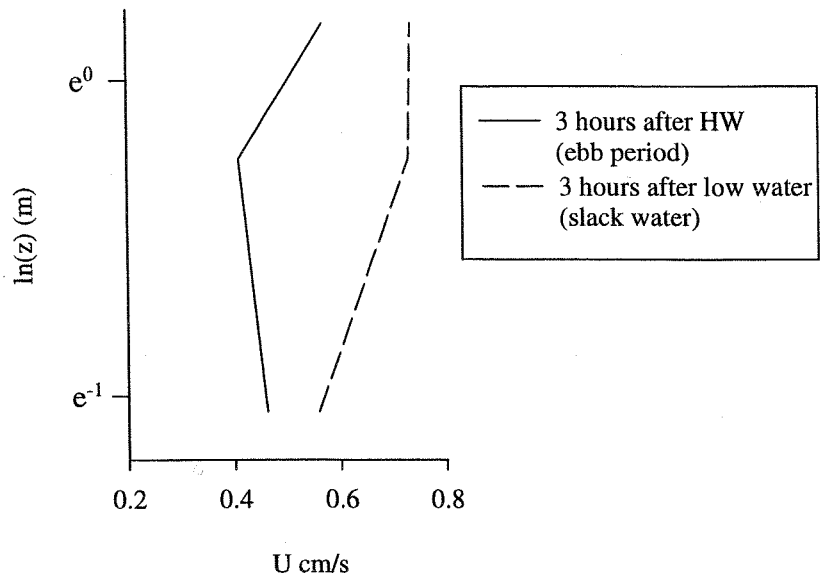

Figure 2-7: Vertical profile of mean horizontal velocity, typical for the ebb phase of the tide and for the flood phase (See Annexe 2 for the mean current variability throughout the tidal cycle).

2.2.3 Macro-scale coherent structures in the BBL flow and their impact on sediment transport

The SSC and velocity time-series are characterised by distinct small-scale (turbulent) and large-scale (macro-turbulent) modules of: (i) small velocity and high SSC; and (ii) high velocity and low SSC. Such features were clearest during periods of strong tidal currents (ebb and flood). Figures 2.8 and 2.9 illustrate the occurrence of such structures during peak ebb tidal flow; records collected during peak flood tidal flows are shown in Annexe 4. These macro-scale oscillations were recorded at all 3 heights; 2 heights only are shown in the Figures for clarity reason. In those plots, no units are attributed to the SSC time-series, due to uncertainty in the nature of the suspensions, and hence in the calibration of the OBS sensors.

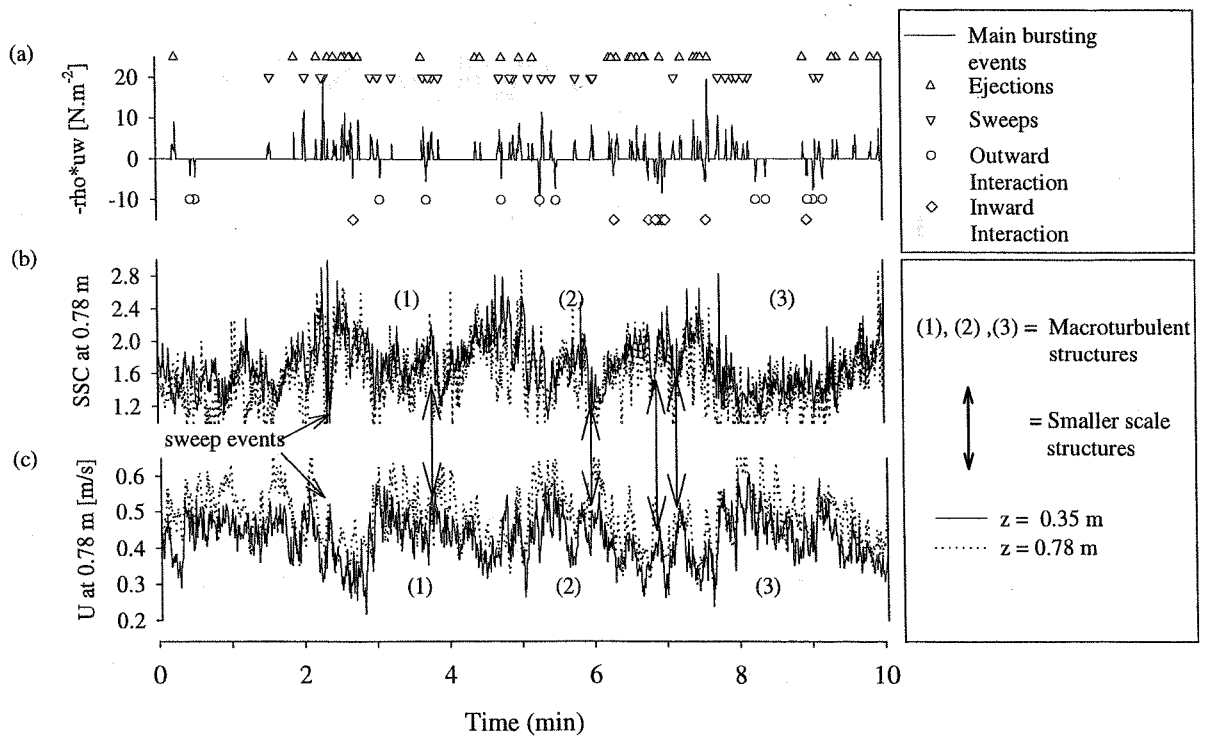

Figure 2-8: Time-series of Reynolds stress (a), SSC (b) and horizontal velocity (c) collected 3 hours after high water (ebb phase, burst n°3 (see Annexe 2)). The large-scale (macro-turbulence) oscillations in the SSC and velocity time-series are typical of the ebb and flood phases of the tide. The symbols indicate the occurrence of the major bursting events.

For analysis of the turbulent and macro-turbulent features contained within the records, the total velocity and SSC time-series were de-trended and separated, by filtering, into turbulent and macro-turbulent time-series. The turbulent time-series of horizontal and vertical velocity (u´ and w´ respectively) and of suspended sediment concentration (ssc´), were obtained by filtering the total velocity and SSC time-series (u, w and ssc), using a high-pass elliptic filter (i.e. the MATLAB function ellip.m, with R_p=0.5 and R_s=34). Similarly, the macro-turbulent time-series (u_{macro}, w_{macro}

and ssc_{macro}) (containing the macro-turbulent flow structure information) were obtained by filtering the wave-filtered time-series, using a low-pass elliptic filter. A cut-off frequency (f_{cut}) of 0.03Hz of both filters was selected from the auto-correlation functions ($r_{uu}(t)$) of the total detrended horizontal velocities. It was chosen as the inverse of the time-lag value T_0, at the first zero-crossing of the auto-correlation function. T_0 defines the approximate extent of the principal large-scale eddies (Figure 2-10).

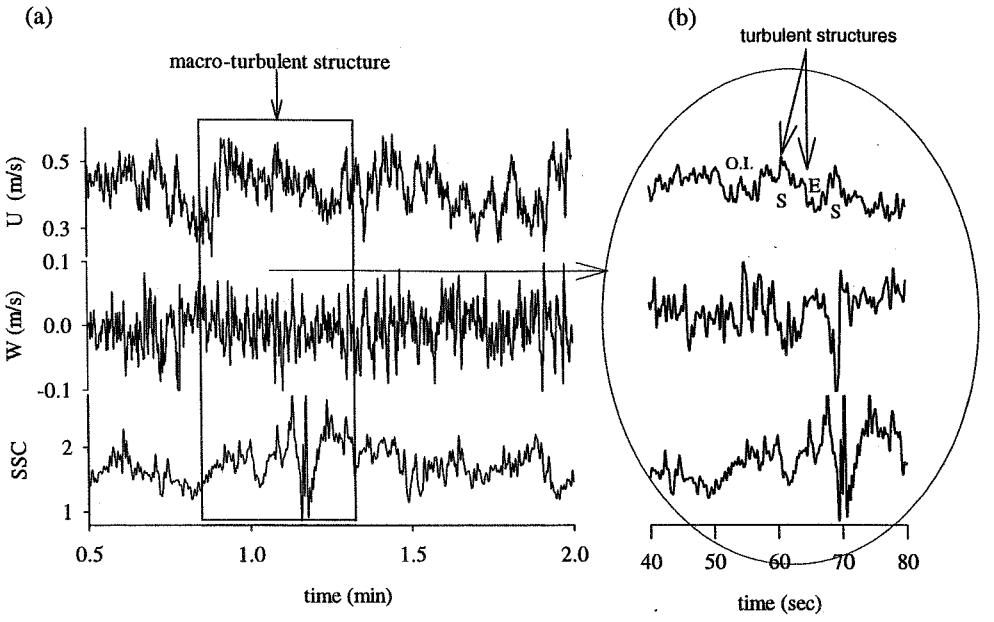

Figure 2-9: Time-series of total horizontal and vertical velocities (U and W) and suspended sediment concentrations (SSC), collected 3 hours after high water (burst n°3). The series illustrate the superposition of turbulent structures (bursting events) (b), within the macro-turbulent structure (a). Legend: E = ejection; S = sweep; OI = outward interaction. The same vertical axis scales are used for the right-hand and left-hand graphs.

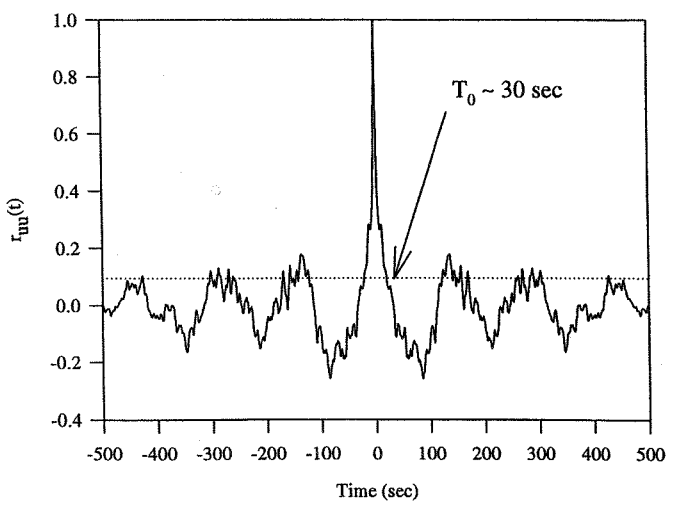

Figure 2-10: Auto-correlation function of detrended horizontal velocity, showing the first zero-crossing (T_0) used as a limit between the high-frequency and the macro-turbulent flow oscillations (burst n°3).

The temporal scale of the turbulent and macro-turbulent flow structures, together with the relationships between the velocity magnitude and the SSC within these modules, were determined using the cross-correlation functions of the turbulent and macro-turbulent SSC and velocity time-series. Typical plots of the cross-correlation functions of the macro-turbulent variables (u_{macro}, w_{macro} and ssc_{macro}) and of the turbulent variables (u′, w′ and ssc′) are shown in Figure 2.11.

Similar velocity and suspended sediment concentration signatures are revealed within the turbulent and the macro-turbulent time-series. Both the turbulent and macro-turbulent cross-correlation curves are characterised by oscillating tails, which reflect the quasi-periodical occurrence of the turbulent and macro-turbulent flow structures within the flow. The cross-correlation functions of u_{macro} and ssc_{macro}, and u′ and ssc′ are both negative, at zero time-lag (Figure 2-11(a) and (d)). This shows that high turbidity is related to low horizontal velocity and low turbidity to high velocity, in both the large-scale and small-scale flow structures. Similarly, the negative correlation between vertical and horizontal velocities ((e) and (f)) reveal that low speed modules are associated mostly with positive vertical velocities, whereas high-speed flows tend to be associated with negative vertical velocities. Positive (upward) vertical velocity is associated also dominantly with increasing SSC and *vice versa* ((c) and (d)). The positive correlation between ssc′ and w′, together with the negative correlation between ssc′ and u′, suggest that 'ejection-like' events ($u'<0$ and $w'>0$) are associated with increases in SSC, while 'sweep-like' events ($u'>0$ and $w'<0$) are associated with SSC decreases.

Multiplication of the time-scale over which the macro-scale structures extend within the time series, by the mean flow speed, indicates that the streamwise extent of the low-speed modules is around 10 to 20 m; similarly, that of the high-speed modules is around 10 to 30 m. The macro-turbulent structure signature appears at all the recording heights (z = 0.35, 0.78 and 1.2 m above the bed), with a high vertical coherence (around 0.80). This pattern shows that the macro-turbulent structures extend at least 1 m vertically. The time-lags for maximum coherence between the SSC, recorded at different heights, show that the structures have an inclination of approximately 60 degrees from the vertical. This angle is slightly higher than the inclinations of the turbid flow structures measured over natural large dunes in the Fraser delta (64-88 degree from the horizontal) (Kostaschuk and Villard, 1999; Kostaschuk, 2000) (forming an angle of about 75^0 from the vertical).

These events are particularly distinct during the peak ebb and flood phases of the tidal cycle, but become more intermittent and weaker during slack water. The percentage of energy contained within the (low) frequency band of the macro-turbulent structures ($f<0.03$ Hz), is related strongly to the mean tidal current speed (Figure 2-12). These observations support the hypothesis that flow-bedform interaction effects generate the macro-scale flow features.

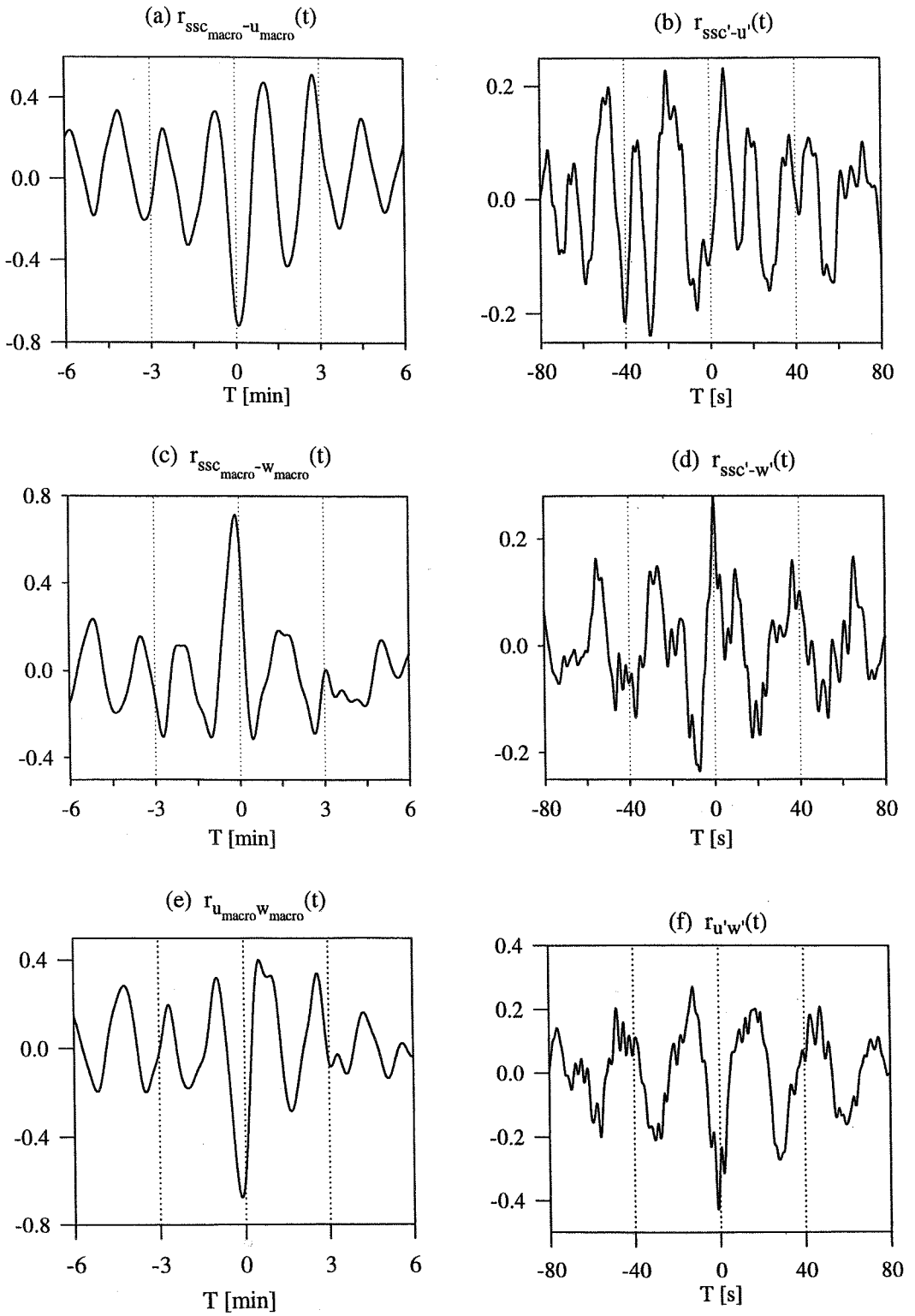

Figure 2-11: Cross-correlation functions of turbulent and macro-turbulent time-series of horizontal velocity and vertical velocity ($r_{u'-w'}$ and $r_{usec-wsec}$ respectively), vertical velocity and SSC ($r_{ssc'-w'}$ and $r_{sscmacro-wmacro}$), and horizontal velocity and SSC ($r_{ssc'-u'}$ and $r_{sscmacro-umacro}$). The time-series were recorded at z = 0.78 m above the seabed, 3 hours after low water (burst n°9)

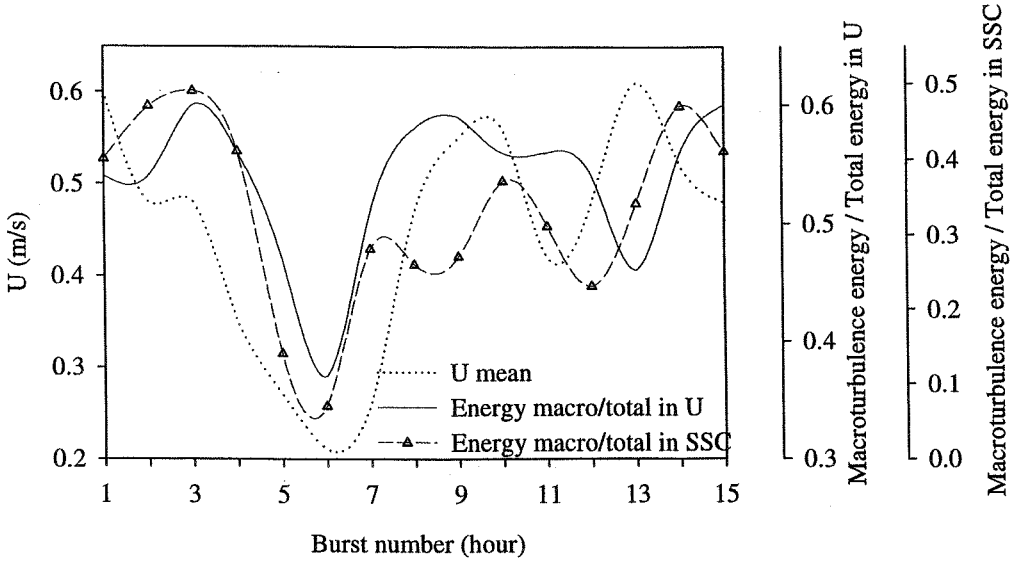

Figure 2-12: Variation in the percentage of energy contained within the low frequency band (macro-turbulence) over the total energy, in the SSC and horizontal velocity time-series, during a tidal cycle. The macroturbulence energy in U or SSC were calculated by integrating the spectra of the U or SSC time-series from 0Hz to 0.03Hz; the total energy in U or SSC is obtained by integrating the spectra from 0Hz to F_N= 2.5Hz.

2.2.4 Modulation of the bursting process by the macro-scale structures

The four types of bursting events (ejection, sweep, outward and inward interactions) are detected in each of the velocity time-series recorded at 0.78 m above the seabed (where three-dimensional speed measurements are obtained). This observation is achieved using the method of Soulsby (1983), as described in Section 1.2.3(iii). The bursting events are plotted with the macro-turbulent velocity time-series in Figure 2-8. The plots reveal that the bursting events are not distributed randomly in time, but occur in relation to the macro-turbulent velocity features. Ejections and inward interactions occur mainly within macro-scale modules of low speed and high SSC, whereas sweep and outward interaction events appear dominantly during macro-scale features of high speed and low SSC. The percentages of each bursting event occurring during periods of high speed macro-scale modules ($U_{macro} > 0$), averaged over the tidal cycle, are presented in Table 2-2. The percentages occurring during $U_{macro} < 0$ are the complements to 100%, of those shown in the Table. The results confirm the previous observation.

The mean duration of both ejections and sweeps is around 10 s, during the flood and ebb currents; this decreases down to 4-5 s during the slack water period. The mean duration of inward and outward interactions varies between 2 and 4 s and is independent of the tidal phase.

Larger (negative) contributions of outward and inward interactions to the Reynolds stress τ are

measured, compared to those reported by other researchers, over smaller roughness elements (Heathershaw and Thorne (1985) and Soulsby *et al.* (1994)) (Table 2-3). It is interesting to note that the larger bedforms present at the measurement site of Soulsby *et al.* (1994) (small sand dunes), compared to those found in the study area of Heathershaw and Thorne (1985) (gravel bed), lead to higher values in the inward and outward interaction contributions to the total Reynolds stress.

Bursting events	Ejections $u'<0, w'>0$	Sweeps $u'>0, w'<0$	Outward Interactions $u'>0, w'>0$	Inward Interactions $u'<0, w'<0$
% occurrence during $U_{macro}>0$	33% (±7)	65% (±11)	65% (±10)	30% (±8)

Table 2-2 : Percentages of occurrence of the four bursting events during macro-scale modules of high horizontal speed. The values are averaged burst-percentages over the deployment period.

The increased participation of outward and inward interactions (which contribute negatively to τ ($-\rho uw_{OI} < 0$ and $-\rho uw_{II} < 0$)), in relation to that of sweeps and ejections (which contribute positively to τ), reduces the value of the Reynolds stress. The Reynolds stress is about 40% lower than the shear stress values estimated using methods based upon the turbulent energy, or on the mean flow velocity (*i.e.* inertial dissipation, turbulent kinetic energy (Huntley, 1988) and Larsen *et al.* (1981) methods) (Figure 2-13). Unexpected low Reynolds stress values were also measured by McLean *et al.* (1996), in separated flows. These authors explained this particular characteristic in terms of a decrease in the correlation, between the vertical and horizontal velocities.

Bursting event	**% of Reynolds stress contribution of each bursting event**		
	TOSCA data (present study)	Soulsby *et al.* (1994)	Heathershaw and Thorne (1985)
Ejections	73.80 %	60 %	50.00 %
Sweeps	69.90 %	56 %	50.90 %
Outward Interactions	-29.90 %	-15 %	-5.28 %
Inward Interactions	-26.80 %	-11 %	-5.57 %

Table 2-3: Average stress contribution to τ of the four bursting events, calculated from all the time-series collected at z = 0.78 m above the seabed. The results are compared with the data obtained by Heathershaw and Thorne (1985) over a gravel bed and by Soulsby *et al.* (1994) over a sandy seabed, covered by small sand dunes (H < 1 m).

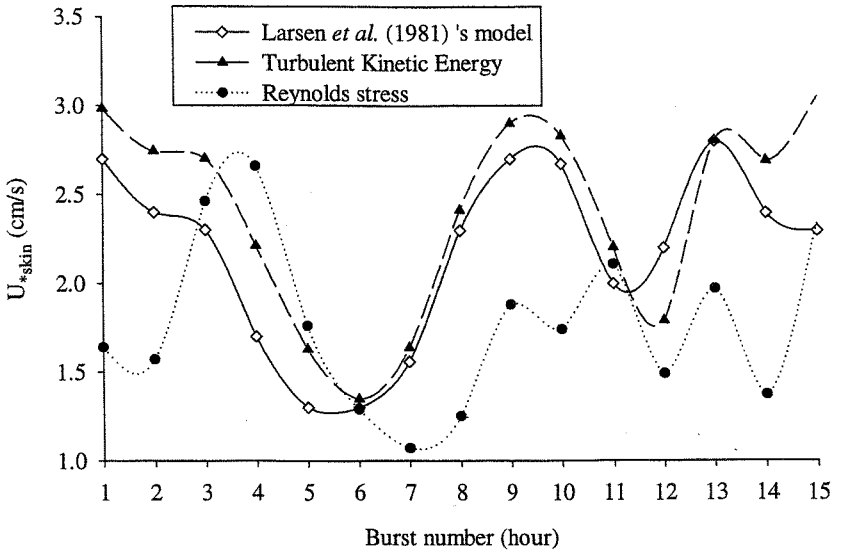

Figure 2-13: Variation in skin friction velocities calculated from the TOSCA measurements (Zeebrugge, September 1994), using the Reynolds stress method, Larsen et al (1981)'s model and the Turbulent Kinetic Energy method.

2.2.5 Turbulence parameters of the BBL flow

Various turbulence parameters of the BBL flow were estimated, to investigate the influence of the large-scale flow structures on the turbulence. The horizontal and vertical rms velocities are shown in Table 2-4. As usually observed in uniform BBL flows, the rms velocities are homogenous with depth.

z [m]	$\left(\overline{u'^2}\right)^{1/2}$ [m/s]	$\left(\overline{v'^2}\right)^{1/2}$ [m/s]	$\left(\overline{w'^2}\right)^{1/2}$ [m/s]	$S_{u'}$	$K_{u'}$	$S_{w'}$	$K_{w'}$
0.35	0.062	0.041	-	0.14 ± 0.12	2.83 ± 0.75	-	-
0.78	0.061	0.041	0.029	0.02 ± 0.17	3.26 ± 1.02	0.01 ± 0.12	3.51 ± 0.29
1.20	0.065	0.045	-	0.02 ± 0.17	2.84 ± 0.22	-	-

Table 2-4 : Tidally-averaged rms velocities, skewness and kurtosis parameters, of the horizontal and vertical turbulent velocities.

The skewness and kurtosis factors are within the 'classic' flow range. The sharp increase of $S_{u'}$, towards the bed, indicates that much larger turbulent velocities occur closer to the bed than above.

The turbulent velocity intensities (Table 2-5) remain approximately constant throughout the tidal cycle. The derived values are close to those reported commonly for uniform BBLs (Table 1-1), although $\left(\overline{u'^2}\right)^{1/2}/u_*$ and $\left(\overline{w'^2}\right)^{1/2}/u_*$ are slightly higher. $\left(\overline{u'^2}\right)^{1/2}/U$ increases towards the bed, as in 'classic' flows.

z [m]	$\left(\overline{u'^2}\right)^{1/2}/u_* \pm$ std	$\left(\overline{w'^2}\right)^{1/2}/u_* \pm$ std	$\left(\overline{u'^2}\right)^{1/2}/U \pm$ std	$\left(\overline{w'^2}\right)^{1/2}/U \pm$ std
0.35	-	-	0.14 ± 0.02	
0.78	3.29 ± 0.81	2.03 ± 0.78	0.13 ± 0.02	0.062 ± 0.014
1.20	-	-	0.11 ± 0.01	

Table 2-5 : Tidally averaged turbulence intensities measured at TOSCA site.

The total turbulence kinetic energy (TKE) was calculated using the three-dimensional velocity measurements obtained at 0.78 m above the seabed (Equation 1-14). TKE values vary between 12 $cm^2.s^{-2}$ (when the current velocity U is the lowest: U=0.30 m/s) and 43 $cm^2.s^{-2}$ (when the current velocity was at a maximum: U=0.65 m/s), with a mean value of 29 $cm^2.s^{-2}$. These measurements are comparable with those described by Soulsby and Humphery (1990), made under conditions of similar mean current speeds.

The mean ratio of the total turbulent kinetic energy $-\overline{uw}/\overline{q^2}$ over the tidal cycle is around 0.05 (Table 2-6). This value is significantly lower than those measured usually in 'classic' flows ($0.15 < -\overline{uw}/\overline{q^2} < 0.20$); it indicates that non three-dimensional coherent turbulence is more important compared to three-dimensional coherent turbulence, than in classic flows. This interpretation is confirmed by the significantly smaller Reynolds stress correlation coefficient ($r_{u'w'}$) than the 'universal' values (Table 2-6).

The skewness and kurtosis parameters of the Reynolds stress are within the range expected in 'classic' BBL flows (Table 2-6).

Z [m]	$u'w'/\overline{q^2}$	$S_{u'w'}$	$K_{u'w'}$	$r_{u'w'}$
0.78	0.05 ± 0.02	-1.37 ± 0.59	11.13 ± 2.69	-0.22 ± 0.09

Table 2-6: Characteristics of the Reynolds stress, measured at z = 0.78 m and averaged over a spring tidal cycle.

The length-scale of the eddies containing most of the flow energy are determined from the wavenumber spectra of the total streamwise velocity fluctuation (u') (*i.e.* using detrended velocity time-series, which were not filtered with high-pass or low-pass filters). Two examples of

typical spectra for the flood-ebb period and 'slack-water' period are plotted in Figure 2-14. The spectral energy peaks demonstrate that, during ebb and flood periods, most of the turbulence energy is contained in features which are 8 m to 10 m in length. Interestingly, these values are of the same order of magnitude as those estimated by multiplying the time-scale of the macro-scale modules (derived visually from the velocity and SSC time-series), by the concomitant mean current speed (Section 2.2.3). During 'slack-water' periods, these large eddies have lost most of their energy (small spectral energy at large wavenumbers) and smaller length-scale features prevail (with spectral energy maxima range between wavelengths of 1 to 4 m). These scales are typical of uniform flows over a flat bed (Table 1-2).

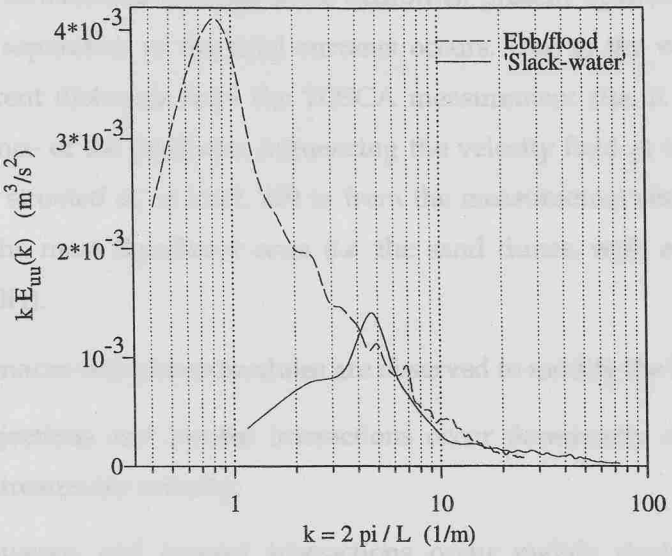

Figure 2-14: Wavenumber spectra of horizontal velocity time-series recorded during peak ebb tidal flow and during low slack water.

The turbulence energy dissipation rates ε were estimated for each measuring height, throughout the tidal cycle, from the spectra of streamwise velocity within the inertial sub-range (Equation 1-23). The limits of the inertial sub-range were determined by: (a) selecting the range of wavenumbers over which the spectral energy of u' decreases as $k^{-5/3}$ (determined visually from the wavenumber spectra); and (b) plotting the selected ε values against k and selecting the range of k values where ε remains constant. The wavenumbers (k) used for the estimation of ε were also limited by the resolution range of the current-meters [k_{low} , k_{sup}]: k_{low} (the largest size of eddies observable) is controlled by the height of the sensor z and the length of the record T; and k_{sup} (the smallest size of eddies observable) is controlled by the size of the sensor head D and the sampling frequency F_s (Soulsby, 1983). The tidally averaged value of turbulence energy dissipation ε

decreased from 0.054 to 0.040 Wm^{-3} between z = 0.35 m and 1.20 m above the bed. These values are typical of near-bed flows in shallow uniform BBL (Heathershaw, 1979; Simpson *et al.*, 1996) (Table 1-3).

The length scale of the eddies l, at which turbulence energy is dissipated through molecular viscosity forces, was estimated from ε: $l = \nu^{3/4} \varepsilon^{-1/4}$ (where ν is the kinematic viscosity = 1.3×10^{-6} m^2/s). A tidal average of $l \cong 0.46 \times 10^{-3}$ m was obtained at all three heights above the bed.

2.3 Discussion of the field results

- The macro-turbulent structures observed at the study site are believed to result from eddies shed downstream of large-scale bedforms, present upstream of the deployment site, where flow separation of the tidal currents occurs. Due to the variety of bedforms distributed at different distances from the TOSCA measurement site, it is difficult to establish the exact distance of the bedforms influencing the velocity field at the site. Any significant bedforms were situated at, at least, 250 m from the measurement site (~ 100 times the bedform height H); the most significant ones (*i.e.* the sand dunes, with a H/d ratio of 0.2) were at 1 km (~600H).
- The macro-turbulence modules are observed to modify the bursting process:
  - ejections and inward interactions occur dominantly during macro-scale events of low streamwise velocity;
  - sweeps and inward interactions occur mainly during macro-scale features of high streamwise flow speed.
- Cross-correlation analysis, as well as visual observation of the velocity and SSC time-series, indicates that ejections induce increases in the SSC, and that sweeps are associated with SSC decreases.
  - The intensification of ejections, during macro-scale modules of low streamwise speed, explains the high turbidity associated with these structures. Ejections are able to lift sediment up from more turbid waters at the bottom of the water column, hence favouring their maintenance into suspension.
  - Conversely, the downward velocities of the sweeps dominating Umacro < 0, favour their low turbidity.
- Ejection and sweep events are observed to dominate almost equally the Reynolds stress production. This contrasts with previous observations over rough beds, where the dominance of sweep events was identified (Section 1.2.2(2)).

- The relative (negative) contributions of inward and outward interactions to the Reynolds stress (compared to that of ejections and sweeps), are larger at the measurement site (i.e. downstream of bedforms) than in 'classic' flows over a flat bed. This characteristic is observed during peak ebb flow and during most of the flood phases of the tide. This characteristics implies that::
  - the values of the Reynolds stress are lower than that expected from the mean flow and total turbulence energy; hence, the Reynolds stress values are lower than the shear stress values estimated using 'mean' flow methods (*e.g.* Larsen *et al.* (1981)), or values derived from turbulence closure scheme models (*e.g.* TKE method) (Figure 2-13);
  - the frequency of outward interaction events in the BBL is related inversely to the magnitude of the Reynolds stress, although outward interaction events may be related to sediment transport processes (see Section 1.4);
  - for the same contributions of sweeps and ejections over a flat bed and downstream of the bedforms, the value of the Reynolds stress is lower downstream of bedforms (due to the increased participation of the negative-stress events OI and II). Since most sediment transport models base their predictions on the shear stress values, it is likely that the Reynolds stress approach will underestimate the transport of sediment in BBLs influenced by large-scale bedforms.
- Other aspects of the flow turbulence at the study site appear to be unaffected by the presence of bedforms.
  - The turbulence intensities, the rate of energy dissipation, and the viscous scales at which turbulent energy is dissipated, are similar to the values observed typically in steady uniform flows.
  - These results are consistent with vortex stretching in 3D turbulent flow fields in which energy is transferred progressively to smaller scales; these retain less detail of the mean and larger scale motions.
- These observations underline the importance of obtaining a detailed knowledge of the turbulence structures of the flow, before deriving mean-value parameters of the turbulent velocity fluctuations for the prediction of sediment transport processes. The turbulent and mean structure of a current flowing over a flat bed can be affected significantly by the presence of upstream large-scale bedforms. The relationships between mean-value parameters of the turbulent velocities, such as the Reynolds stress, and sediment transport quantities, may not apply in the same manner as in 'classic' uniform flows.

Chapter 3

Laboratory investigation: flow turbulence and bedload transport downstream of a large-scale bedform

3.1 General setting

3.1.1 Objectives

The turbulence processes generating bedload transport downstream of a large-scale bedform, were investigated further in a flume laboratory. The properties of the mean flow and of the turbulence were determined, in order to test the findings of the field investigation (previous Chapter) and to investigate further the following aspects: (i) the mean flow structures; (ii) the turbulence and macro-turbulence characteristics; (iii) the turbulence mechanisms initiating bed sediment movement, downstream of bedforms; (iv) the implications for modelling the flow and sediment transport processes, downstream of large-scale bedforms.

3.1.2 Instrumentation and methods

1) The flume

The experiments were performed in a straight re-circulating rectangular flume (Figure 3-1) of the School of Ocean and Earth Science (SOES) (University of Southampton).

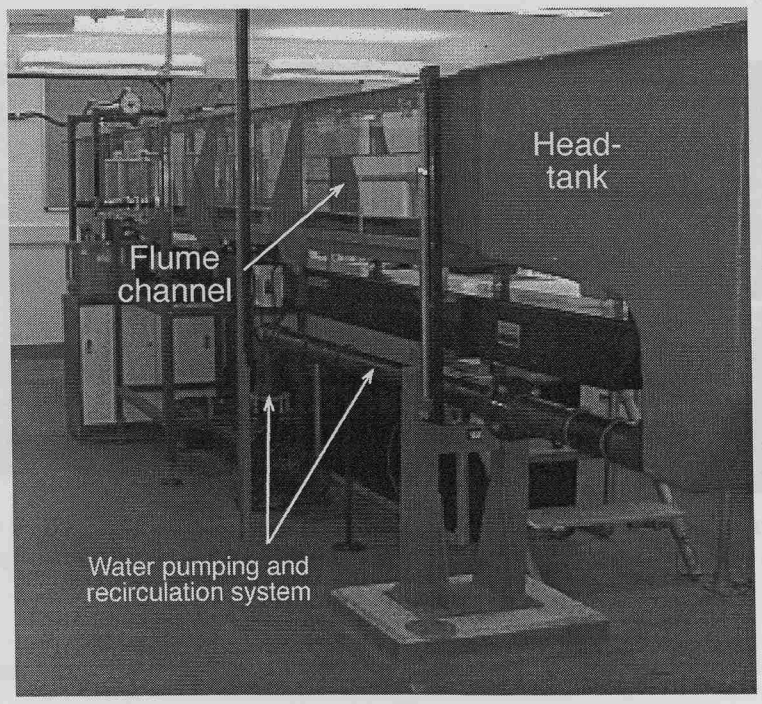

Figure 3-1: The SOES straight flume : rectangular, recirculating and unidirectional.

The flume is 5.0 m long, 0.30 m wide and 0.45 m deep. The flow characteristics inside the flume have been examined previously, in detail, by Tomlinson (1993). The flow is unidirectional along the channel by an electric pump. Water enters the channel through a head-tank, then through a

'honey comb' structure, which dampens the turbulence generated by the pump. The water depth in the flume is controlled manually, by adjusting a tilting valve at the upstream end of the flume; it was set at either 0.20 m or 0.30 m, during the experiments. Fine sand was glued onto the bed, to roughen it.

2) The bedform

An asymmetrical bedform, made of plywood fabricated, was fixed onto the bed of the flume (Figure 3-2(a)); it was 0.06 m high, 0.22 m long (wavelength), with an Asymmetry Index (length of the stoss side horizontal projection to the bedform height (H) ratio) of 2.1 and a 'Ripple' Index (base length to height ratio) of 3.8. The aspect ratio of the bedform (W/H, where W is the width of the bedform) is about 5; however, the bedform width extends across the flume cross-section which represents the case of two-dimensional bedforms, characterised by the absence of transversal-flows. A steep-shape bedform was chosen, in order to enhance the form drag and, hence, to distinguish better its influence on the bed sediment from that of the bed friction. A single bedform was used, instead of a field of bedforms, in order: (i) to avoid the overlap of the different hydrodynamic regions developing upstream and downstream of the bedform; and (ii) to complement past studies, which have concentrated on fields of bedforms (ripples or sand-dunes) (Nelson *et al.*, 1993, 1995; McLean *et al.*, 1994; Bennett and Best, 1995).

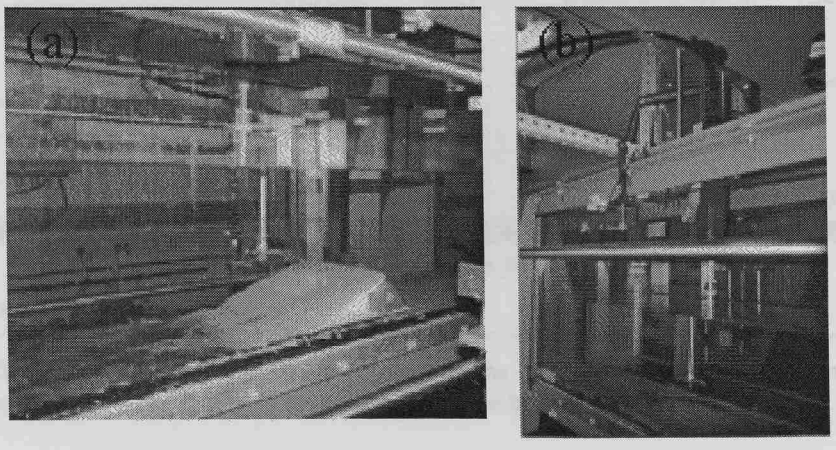

Figure 3-2: (a) The large-scale bedform in the flume, with the ADV sampling upstream. (b) The ADV, mounted on a structure allowing up and down vertical movements, sampling over a flat bed.

3) Flow measurement

A three-dimensional downward-looking Acoustic Doppler Velocimeter (ADV, 10 MHz, Norteck As) measured the flow velocity field in the channel (Figure 3-2(b)). The ADV was mounted on a metallic frame fixed on top of the flume, equipped with a vertically-moving section to allow vertical profile sampling. The vertical movements were controlled manually, using a rotor device,

allowing up and down vertical movements, with a precision of about 1 mm. The 3 components of the flow velocity field were recorded at 25 Hz, by bursts of 10 min.

Vertical velocity profiles were measured between 0.5 cm and 12 cm above the bed (the maximum height technically allowed). The spacing between the measurement points within the flow depth was 0.5 cm over the lower 3 cm bottom layer, and 1 cm or more, above. To study the streamwise variation of the flow characteristics, the bedform was moved along the flume and fixed at different distances upstream and downstream of the ADV sampling profile (and sediment-testing area). This avoided any changes in the vertical and streamwise alignment of the ADV with the mean flow between each sampled vertical profiles. The positions sampled (Figure 3-3) were included within: (i) the flat bed region, to determine the 'background' flow structure inside the flume (as explained below); (ii) the upstream region; (iii) the lee region, to study the flow structures and sediment movements in a region where the mean flow is least uniform; (iv) the intermediate region; and (v) the far wake region, to allow comparison with the field measurements (Chapter 2). The extent of the recirculation region was determined prior to these measurements, using flow-visualisation images (the technique is described below).

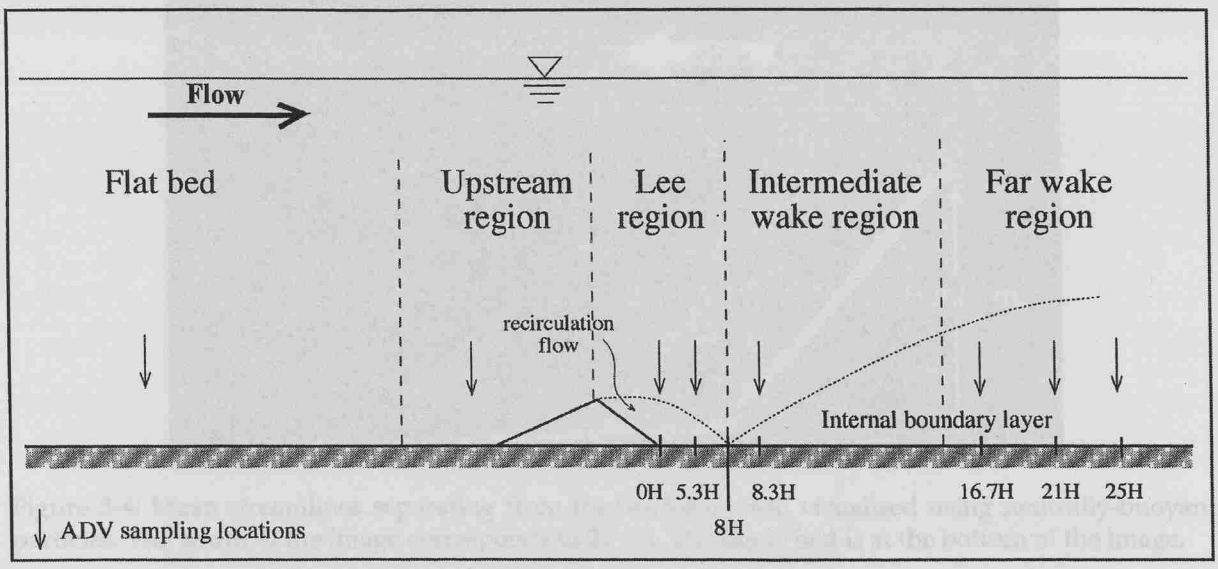

Figure 3-3: Hydrodynamic regions in the flow around the bedform and location of the ADV velocity profiles measurements (not to scale). H is the heigth of the bedform.

The measurements were performed for different flow discharge rates. At each flow discharge rate, the turbulence and mean flow structure were also measured over flat bed, to determine the 'background turbulence' in the flume. Comparison between the profiles measured and the 'background' profiles determined the 'net' effect of the bedform on the flow dynamics.

A slightly different procedure was applied for the 2 farthest positions downstream (x = 21H and 25H) to that outlined above. For these positions, the ADV was moved downstream, to maintain the bedform within the middle section of the flume, to minimise any potential influence from the flume-end inflow. Analysis of the velocity profiles collected at these latter positions, over a flat

bed, showed that the 'background' flow characteristics are similar to those at the previous ADV position. Further, due to time constraint, only a single profile was collected at these positions, for a moderate flow regime. These profiles were collected after all the other measurements were obtained.

Measurements were collected only over the flat bed area, upstream and downstream of the bedform, for comparison with the field measurements (Chapter 2). This approach was motivated also by the fact that the quality of the ADV records deteriorated on the sloping flanks of the bedform. The cause of this deterioration is not clear.

The flow structures generated downstream of the bedform were visualised using video 'particle tracking'. White neutrally-buoyant particles (Pliolite, Good Year™) were injected into the water in the head-tank and were tracked in the flow of the flume using a video camera (50 frames/s). An example of the mean flow streamlines separating from the bedform crest is shown in Figure 3-4. Figure 3-5 shows examples of turbulence structures visualised near the re-attachment zone.

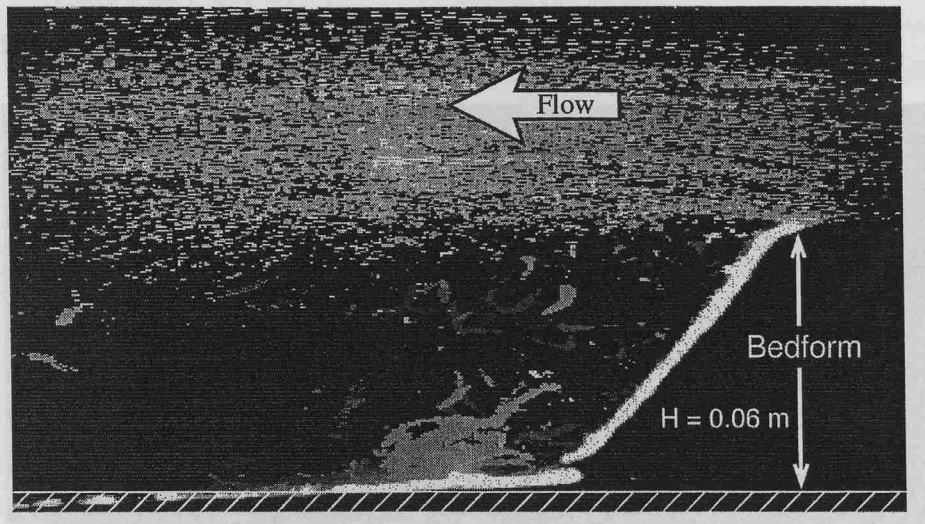

Figure 3-4: Mean streamlines separating from the bedform crest, visualised using neutrally-buoyant particles. The width of the image corresponds to 32 cm. The flume bed is at the bottom of the image.

4) Sediment transport observations

Sand (0.125-0.150 mm in diameters) or gravel (~ 4 mm diameter) were introduced onto the flume bed, up to the level of a cylindrical hole (9 cm diameter and 2 cm deep), located at the centre of the flume bed. Bedload movements and resuspension events of the sediment were observed visually, over a flat bed and at three positions downstream of the bedform: x = 3.3H, 8.3H and 16.7H. The suspended sediment transport was not studied, due to technical limitations *i.e.* the water is re-circulated in the flume, via large water storage tanks, where the material placed into suspension in the channel is lost by sedimentation.

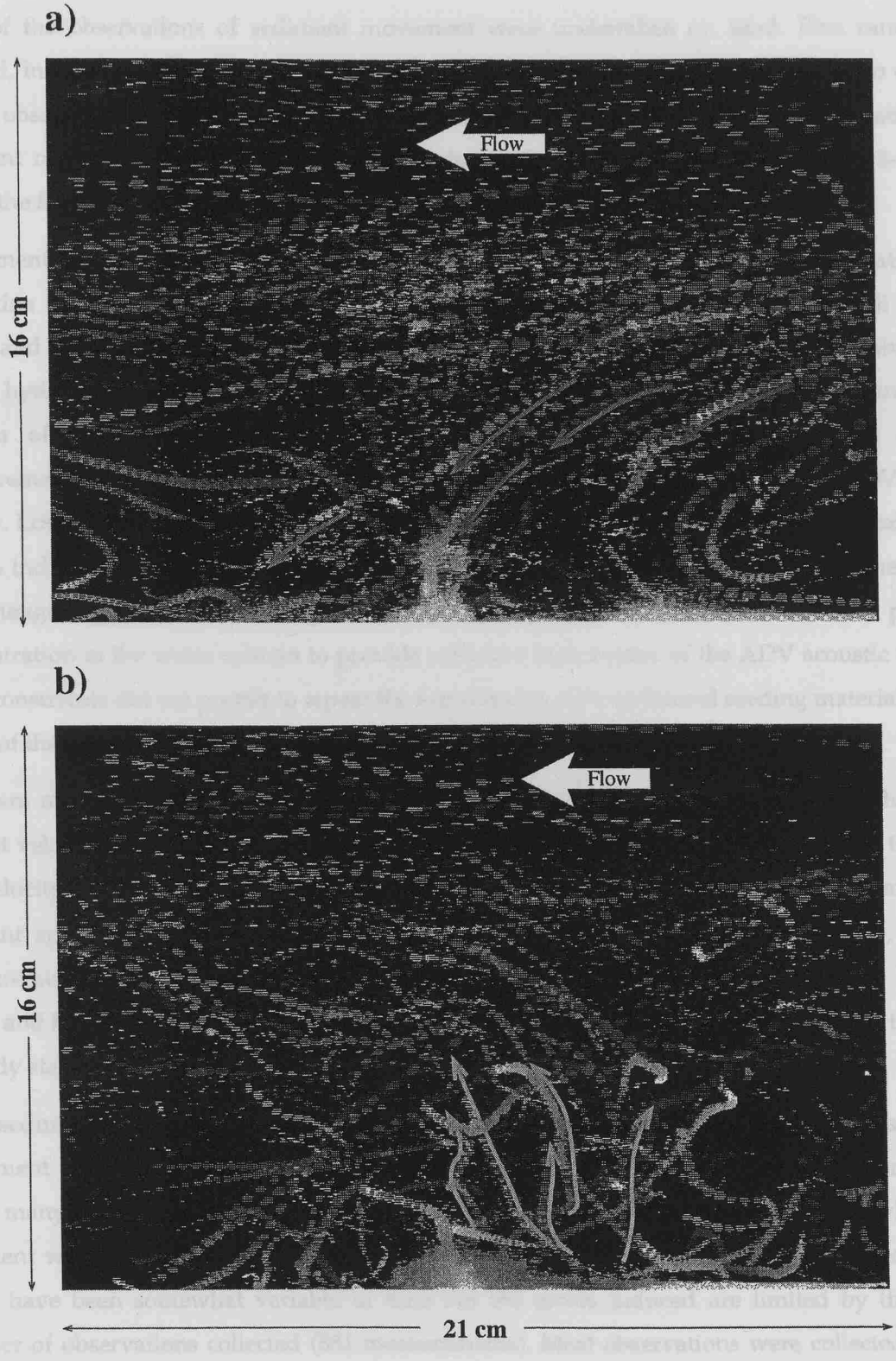

Figure 3-5: Turbulent flow structures visualised with neutrally-buoyant particles. (a) intermittent downward streaks (sweeps or II); followed ~20 s later by (b) intermittent upward flows (ejections or OIs). The image extend over the region $6H \leq x \leq 9.5H$ downstream of the bedform.

Most of the observations of sediment movement were undertaken on sand. Fine sand was selected, instead of (for example) cohesive sediment or coarser-grained sand, in order to enable visual observation of individual particle movements. It permitted also the observation of sediment movement and re-suspension, at moderate flow discharge rates (see Table 3-3), for which the flow in the flume is most uniform.

Experiments over a gravel bed were carried out during the latter phase of the investigation, to determine the eventual differences in the turbulence signal associated with light small grains (sand) and heavy protuberant grains (gravel) transport. Since no clear differences were observed in the hydrodynamic control of the bedload transport of these two types of sediments, the number of experiments undertaken with gravel was limited. Furthermore, some of the measurements collected over the gravel bed had to be eliminated, due to insufficient ADV signal quality. Low signal correlation coefficient values (below 80 %, but above the lower critical value of 70% indicated by the manufacturer (Nortek AS, 1998)) were obtained after the flume water was changed (prior to undertaking the gravel experiments); this resulted in too low particle concentration in the water column to provide sufficient back-scatter of the ADV acoustic waves. Time constraints did not permit to repeat the experiments with additional seeding material in the water of the flume.

Sediment movement observations were collected over 2 minutes, simultaneously with the ADV current velocity measurements. Most of the observations were collected in simultaneity to near-bed velocity measurements ($z < 3$ cm). The flow was run for 30 min over the bed sediments, at a constant speed (7×10^{-2} m/s) below the threshold of movement of the sand particle, before measurements were undertaken. This procedure created similar bed sediment stress history (Little and Mayer, 1976), for all the sediment transport experiments and allowed the flow to reach a steady state.

Each sediment movement was defined by its time of initiation, its type and its scale. The movement was described as 'small' when only a few grains (up to 3) moved slowly or 'large' when many grains were rolling rapidly, 'small resuspension' or 'large resuspension' when the sediment was put into suspension as small or large clouds respectively. This visual technique could have been somewhat variable in time but the errors induced are limited by the large number of observations collected (851 measurements). Most observations were collected under strong enough flow regimes (significantly above the threshold conditions for bedload movement), to obtain as many sediment movement events as possible. The flow speed was low enough, however, to limit the sediment transport rate, so that each sediment movement event could be identified clearly and noted. Only the sediment movements occurring just beneath the ADV sampling volume were noted, so that the bursting events causing them could be recorded by the ADV. Attempts were made to record sediment movements using a video camera (50

frames/s) equipped with a macro-lens. However, this method was abandoned, since the resolution of the image was not sufficient to observe the small bedload movements and to distinguish large bedload movements from re-suspension events.

The ADV velocity signal, at the time of each sediment movement, was analysed to determine, subsequently during the analysis procedure: (i) the sign of the 3 velocity components of the turbulent flow structure e.g. bursting events (see Section 1.2.2); (ii) the length-scale of the turbulent flow structures; and (iii) the magnitude of the instantaneous Reynolds stress and TKE.

3.2 Results

3.2.1 Data collected

1) Velocity measurements

The flow measurements analysed in this work consist of:

- 4 streamwise profiles across the bedform, collected at the mid-cross-section of the flume bed, at 2 velocity regimes and 2 water depths (d=20 and d=30 cm) (Table 3-1).
- An extensive set of vertical profiles, measured at different mean flow velocities, at different streamwise positions (x) in relation to the bedform (Figure 3.3): 1 cm upstream of the bedform (i.e. x = -4H, where x = 0 corresponds to the lee base of the bedform, with the positive x axis pointing downstream), and x = 0H, 2.5H, 3.3H, 5.3H, 8.3H, 16.7H, 21H and 25H, downstream of the bedform (see Section 3.1.2(3)) (Table 3-2).

The parameters used in the Tables are:

- U_{1cm} mean current speed at 1 cm above the bed (within the logarithmic layer)
- U_{∞} mean current velocity of the free stream flow (top of the BBL)
- δ_{BBL} thickness of the BBL
- δ_{log} thickness of the logarithmic layer
- $\mathrm{Re} = U_{\infty}\delta_{BBL}/\nu$, the Reynolds number

The flow is always fully turbulent (Re $\cong 10^4$ or more). The turbulence structure and the length of the flow separation zone downstream of the bedform may be expected, therefore, to be weakly dependant upon the Reynolds number, or on the thickness of the BBL (Martunizzi and Tropea, 1993). The Reynolds number increases by a factor of at least 2 from flat bed conditions to positions downstream of the bedform (from the lee up to x ≥ 17H, where H is the bedform height) for a fixed flow regime.

d [cm]	Profile reference	Location	U_{1cm} [cm/s]	U_∞ [cm/s]	δ_{BBL} [cm]	δ_{log} [cm]	Re
20	S1 (constant water discharge Q1)	Flat bed	15	~18*	5<δ<7	~5	[7,000 - 9,200]
		-4H	12.8	17	9	7	11,500
		0H	-4.3	~25	δ > 12 *[1]	<0.3	[23,000 - 38,500]
		3.3H	-5.3	~24	δ > 12 *[1]	<0.3	[22,200 - 37,000]
		8.3H	7.3	~20	δ > 12 *[1]	2	[18,400 - 30,700]
		16.7H		~18	δ > 12 *[1]	7	[16,600 - 28,000]
20	S2 (Q2)	Flat bed	19.1	22.7	7	7	12,200
		16.7H	17.8	~22	δ > 12 *[1]	7	[20,300 - 33,900]
30	J1 (Q3)	Flat bed	10.2	12.4	7	5	6,700
		-4H	8.2	12.0	7	7	6,500
		0H	-2.2	15.9	δ > 12 *[1]	<0.6	14,700
		3.3H	-3.0	~16	δ > 12 *[1]	1.5	[14,800 - 37,000]
		8.3H	3.9	~14	δ > 12 *[1]	3	[27,800 - 32,300]
		16.7H	7.9	~13	δ > 12 *[1]	5	[12,000 - 30,000]
30	J2 (Q4)	Flat bed	18.9	23.0	?	5	[21,200 - 53,000]
		8.3H	7.5	~22	δ > 12 *[1]	1.5	[20,300 - 51,000]
		16.7H	16.3	~24	δ > 12 *[1]	5	[22,100 - 55,400]

Table 3-1 : Flow regime of the streamwise profiles (S1, S2, J1 and J2) collected in the flume, at 4 locations x in relation to the bedform (-4H ≤ x ≤ 16.7H). For each streamwise profile, the water discharge rate in the flume channel is kept constant for all measurements at each location. The discharge rate is different, however, for each streamwise profile. Note: *[1]: δ exceeds the maximum measuring height.

Location	d [cm]	Number of profiles	U_{1cm} [cm/s]	U_∞ [cm/s]	δ_{BBL} [cm]	δ_{log} [cm]	Re
Flat bed	20	7	[14 - 26]	[18 - 31]	7	5	[8,600 - 19,000]
	30	2	[10 - 19]	[12 - 23]	7	5	[7,000 - 14,200]
3.3H	20	7	[-4.5 - -6.2]	[25 - 30]	δ > 12 *[1]	< 0.3	[23,100 - 46,200]
	30	2	-2.9	~17	δ > 12 *[1]	< 0.3	[14,800 - 26,200]
8.3H	20	3	[4.9 - 6.9]	[23 - 30]	δ > 12 *[1]	< 0.3	[21,200 - 46,200]
	30	2	[3.9 - 7.5]	[~15 - ~27]	δ > 12 *[1]	< 0.5	[13,900 - 41,500]
16.7H	20	5	[~13 - 7.8]	[~18 - ~23]	δ > 12 *[1]	7	[16,600 - 35,400]
	30	2	[7.9 - 16.3]	[~14 - ~25]	δ > 12 *[1]	[5 - 7]	[12,900 - 38,500]
21H	20	1	~20	~24	δ > 12 *[1]	> 12	[22,153 - 36,923]
25H	20	1	~20	~24	δ > 9 *[1]	> 9	[16,615 - 36,923]

Table 3-2 : Ranges of the flow parameters characterising all the vertical velocity profiles collected at each of the 6 locations in relation to the bedform. Different flow discharge rates characterise each vertical velocity profiles at each particular location. Note: *[1]: δ exceeds the maximum ADV measuring height.

2) Bedload transport observations

The flow conditions and the number of sediment movements measured successfully (including only those associated with a clear velocity signal), are listed in Table 3-3.

No observation of gravel movements were obtained over a flat bed, since the maximum water discharge in the flume was insufficient to reach threshold conditions.

Location	Number of velocity time-series	Number of sediment movement events observed		U_{1cm} range [cm.s^{-1}]	τ_0 range [N.m^{-2}]
		Sand	Gravel		
Flat bed	11	73	0	[26 to 50]	[0.1 to 0.3]
3.3H	19	212	129	[-6 to -14]	[0.5 to 5.7]
8.3H	21	208	122	[7 to 15]	[0.4 to 3.5]
16.7H	11	96	11	[15 to 35]	[0.2 to 1.9]

Table 3-3 : Data collected during the sediment transport experiments, over flat bed and at different distances from the bedform.

3.2.2 Hydrodynamic regions around the bedform

The mean structure of the flow changes distinctly as it passes across the bedform. A typical variation in the vertical profile of the mean horizontal velocity (streamwise profile J1, Table 3-1) is shown in Figure 3-6. Four hydrodynamic regions can be distinguished around the bedform, on the basis of the mean flow structure: the flat bed region, the upstream region, the re-circulation region, the intermediate region and the far wake region (see also Figure 3-3). The general mean flow characteristics of the regions are described below.

1) Flat bed region

The 'flat bed' region corresponds to the part of the flow far enough from the bedform not to be influenced by it. The flow in the flume over the flat bed has a well-developed BBL and logarithmic layer (the thickness of the BBL (δ_{BBL}) ~ 7 cm (i.e. 23-35% of the water depth d) and δ_{log} ~ 4-5 cm (i.e. 70% of δ_{BBL}) at all flow regimes). These characteristics are representative of a 'classic' uniform flow.

2) Upstream region

In the upstream region, the flow is influenced by the obstruction caused by the bedform. This region was investigated at 1 cm upstream of the stoss face base of the bedform (x = -4H, see

Figure 3-3). Here, the near-bed flow is slightly decelerated (e.g. a reduction of about 10%), whereas the upper flow is accelerated to compensate for the reduced near-bed flow discharge. The thickness of the BBL and of the logarithmic layer increases, respectively, by 30 and 40%, compared to those observed over a flat bed (Figure 3-6). The vertical profiles of mean horizontal velocity, within the bottom layer of this region, follows more closely a logarithmic variation compared to the profiles over a flat bed (higher regression coefficient of the logarithmic fit; see Section 1.6.2(2)).

3) Re-circulation region

The (flow) re-circulation region corresponds to the zone where the flow separates over and downstream of the bedform crest (Figure 3.7). Two locations were sampled within this region: x=0H and x=3.3H (Figure 3-3). The separated wake flow is characterised by a near-bed current flowing upstream, and an upper layer flowing downstream. The 'upstream-flowing' bottom layer becomes thinner downstream (it is about 0.8H in thickness at x = 0H; while about 0.5H thick at x=3.3H). The current speed within this layer is almost constant, with height above the bed. No (measurable) bottom logarithmic velocity layer is present. In the upper layer, the mean horizontal current speed increases logarithmically with height above the bottom layer, as it would over a 'solid' boundary in classic flows (Figure 3-6).

Video images collected during the 'particle tracking' experiments (Section 3.1.2(3)) show that the length of the re-circulation region extends up to a distance of about 8H downstream of the bedform. The re-attachment length does not vary with the flow speed or water depth, which is typical of fully turbulent flows (Martunizzi and Tropea, 1993). The re-attachment length is within the range predicted by Martinuzzi and Tropea (*op. cit.*) for fully turbulent flows, over obstacles with very large aspect ratios (W/H>10, where W is the width of the obstacle) and, hence, over two-dimensional bedforms, as used in this work (see 3.1.2(2)).

4) The intermediate and far wake regions

This intermediate region includes the zone just downstream of the re-attachment zone, where the internal BBL re-develops; it was sampled at x = 8.3H. The far-wake region, sampled at x = 16.7H, is characterised by a well-developed BBL. In both regions, the logarithmic layer is thinner than over a corresponding flat bed (~7-10% of d at x=8.3H and ~10-15% of d at x=16.7H), but the BBL is much thicker; it exceeds the measuring water depth (> 0.5d). Within the 'intermediate wake' region, the influence of the separated 'free-shear' layer throughout the BBL is large compared to that of the wall-friction. In comparison, within the 'far wake' region, the influence of the wake is less than that of the wall-shear flow.

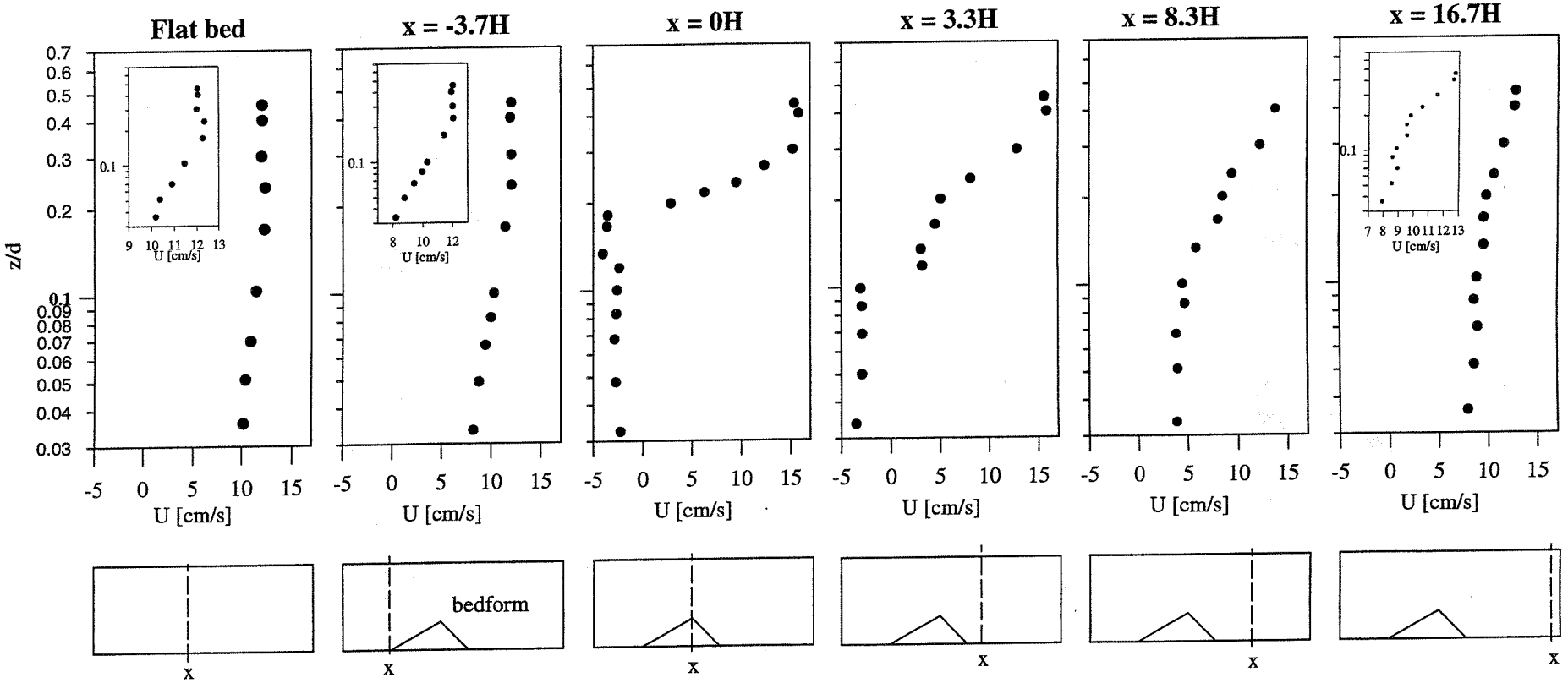

Figure 3-6: Logarithmic velocity profiles measured within the 4 hydrodynamic regions around the bedform (streamwise profile J1, Table 3.1). The smaller graphs correspond to the larger graphs in which they are inserted, over a more restricted velocity range.

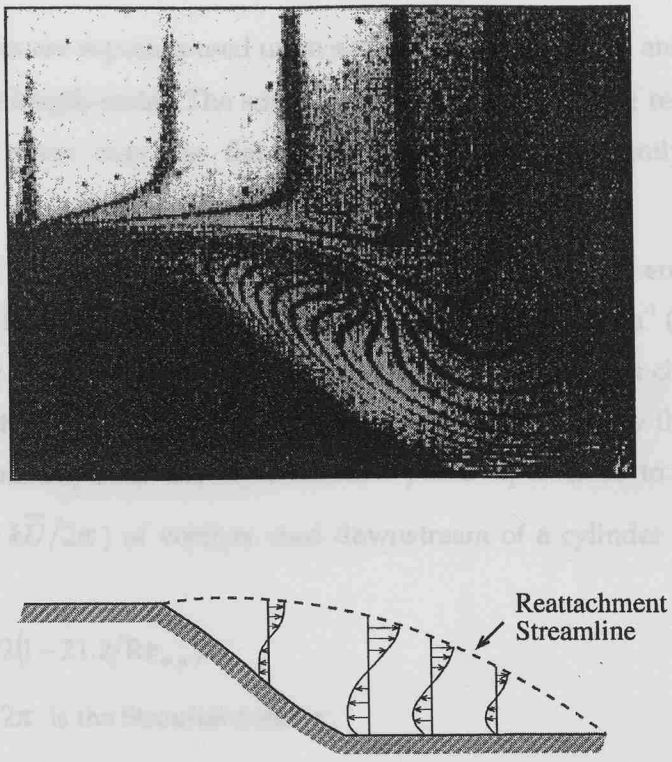

Figure 3-7: Wake region in the lee of a large-scale bedform (from Muller and Gyr, 1996).

3.2.3 Macro-turbulence structures

Long-scale mean current oscillations can be detected in the velocity time-series (Figure 3-8).

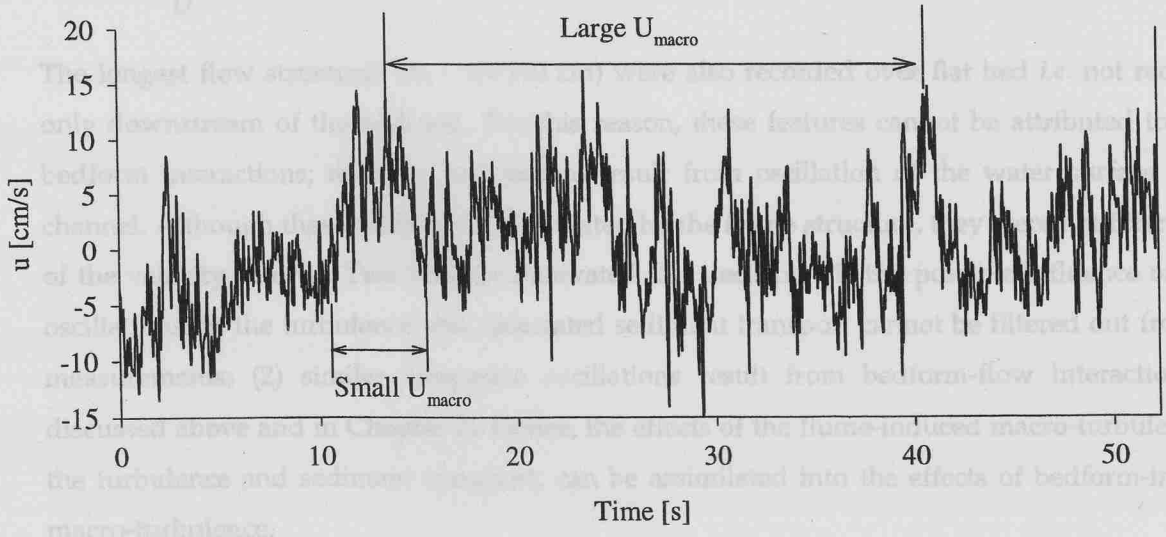

Figure 3-8: Superposition of 2 macro-scale flow speed oscillations, in the velocity signals recorded downstream of the bedform (at x=3.3H). 'Large U_{macro}' indicates the largest-scale flow structures (length-scale λ=60 to 110 cm), and 'Small U_{macro}' indicates the smallest flow structures (λ ~ 25-30 cm).

Two oscillation scales are superimposed upon each other: λ_1 ~ 25-30 cm and λ = 60-110 cm (where λ is the streamwise length-scale). The smaller velocity oscillations are recorded downstream of the bedform, but never over the flat bed; they result, consequently, from bedform-flow interaction effects.

The occurrence of the oscillations is revealed within the velocity energy spectra recorded downstream of the bedform, at wavenumbers around k_1 ~ 0.20-0.22 cm^{-1} (Figure 3.9). The energy peak is particularly distinct at the low flow discharge rates and is least clear (or absent) near the re-attachment point. The energy peak is particularly distinct at the low flow discharge rates and is least clear (or absent) near the re-attachment point. k_1 is close to the primary shedding frequency f ($f = k\overline{U}/2\pi$) of vortices shed downstream of a cylinder (Abarbanel *et al.*, 1991) (Equation 3-1).

$$St = 0.212\left(1 - 21.2/\mathrm{Re}_{\infty,\phi}\right) \qquad \text{Equation 3-1}$$

where $St = k\phi/2\pi$ is the Strouhal number,

$\mathrm{Re}_{\infty,\phi} = U_\infty \phi/\nu$ and

ϕ is the sphere diameter.

Replacing the sphere diameter by the bedform height, H = 6 cm, gives St ~ 0.212 and a shedding wavenumber k = 0.22 cm^{-1}.

Interestingly, the frequency f of the oscillation ($f = k\overline{U}/2\pi$) is also close to the frequency of surface boils observed in rivers (Jackson, 1976) (Equation 3-2).

$$\frac{fd}{U} = 0.16 \qquad \text{Equation 3-2}$$

The longest flow structures (λ_2 = 60-110 cm) were also recorded over flat bed *i.e.* not recorded only downstream of the bedform. For this reason, these features cannot be attributed to flow-bedform interactions; they are believed to result from oscillation of the water surface in the channel. Although these oscillations are created by the flume structure, they were not filtered out of the velocity records. Two reasons motivated this decision: (1) the possible influence of these oscillations on the turbulence and associated sediment transport cannot be filtered out from the measurements; (2) similar long-scale oscillations result from bedform-flow interactions (as discussed above and in Chapter 2). Hence, the effects of the flume-induced macro-turbulence on the turbulence and sediment transport, can be assimilated into the effects of bedform-induced macro-turbulence.

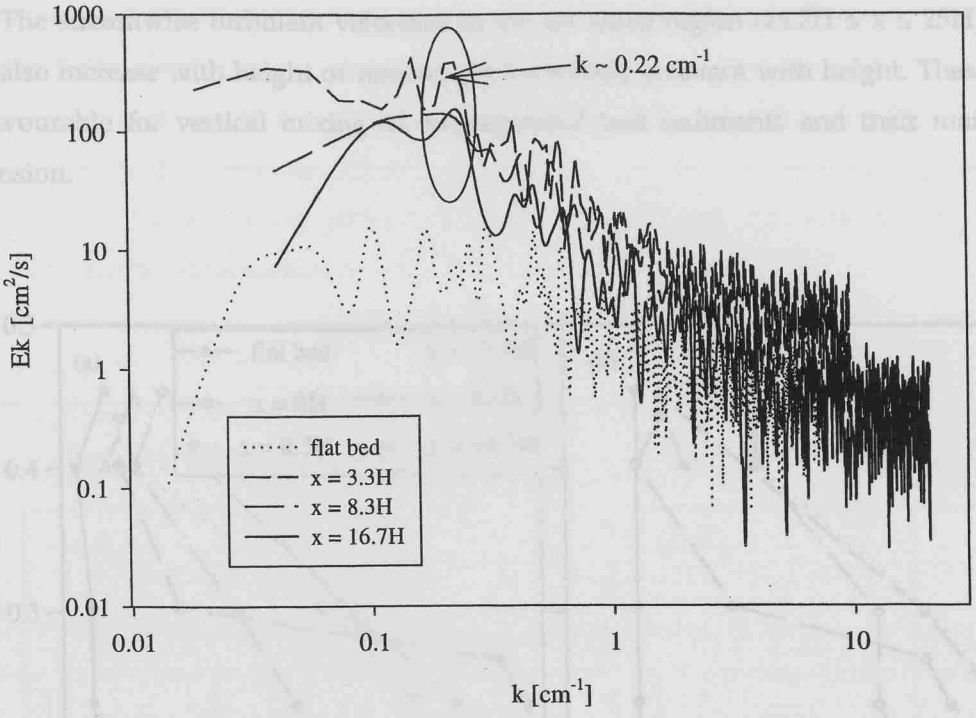

Figure 3-9: Energy spectra of horizontal velocity fluctuations recorded over flat bed and downstream of the bedform. The presence of an energy peak around k=0.22 cm-1 can be seen in the spectra recorded downstream of the bedform but not over flat bed.

3.2.4 The turbulence field

1) Turbulent velocity field

(i) Spatial variability

The turbulent horizontal and vertical velocities are much larger downstream of the bedform than over the flat bed, over a large part of the BBL (up to z ≅ 0.3d) (Figure 3-10).

In the near-bed layer (z ≤ 0.10d), the turbulent velocities reach their maxima near to the re-attachment point; here, the $\sqrt{\overline{u'^2}}$ and $\sqrt{\overline{w'^2}}$ values are 2.5 to 3.5 times those over flat bed, for minimum and maximum mean flow speeds, respectively (Table 3-2). In the lee of the bedform, the near-bed velocity fluctuations are only slightly larger than those over a flat bed (~1.5 times larger); this is due to the low mean velocity and mean velocity shear in this region (Figure 3-6). The turbulent velocities remain high up to large distances downstream of the bedform: they are still up to 1.5 times the flat bed values at x = 25H.

Downstream of the bedform (for x ≥ 3.3H and up to x = 25H, or more), the vertical velocity

presence of a free-shear layer, propagating from the point of flow separation, at the bedform crest. The streamwise turbulent velocities in the far wake region (16.7H ≤ x ≤ 25H) and at x = 3.3H, also increase with height or remain approximately constant with height. These conditions are favourable for vertical mixing of re-suspended bed sediments and their maintenance in suspension.

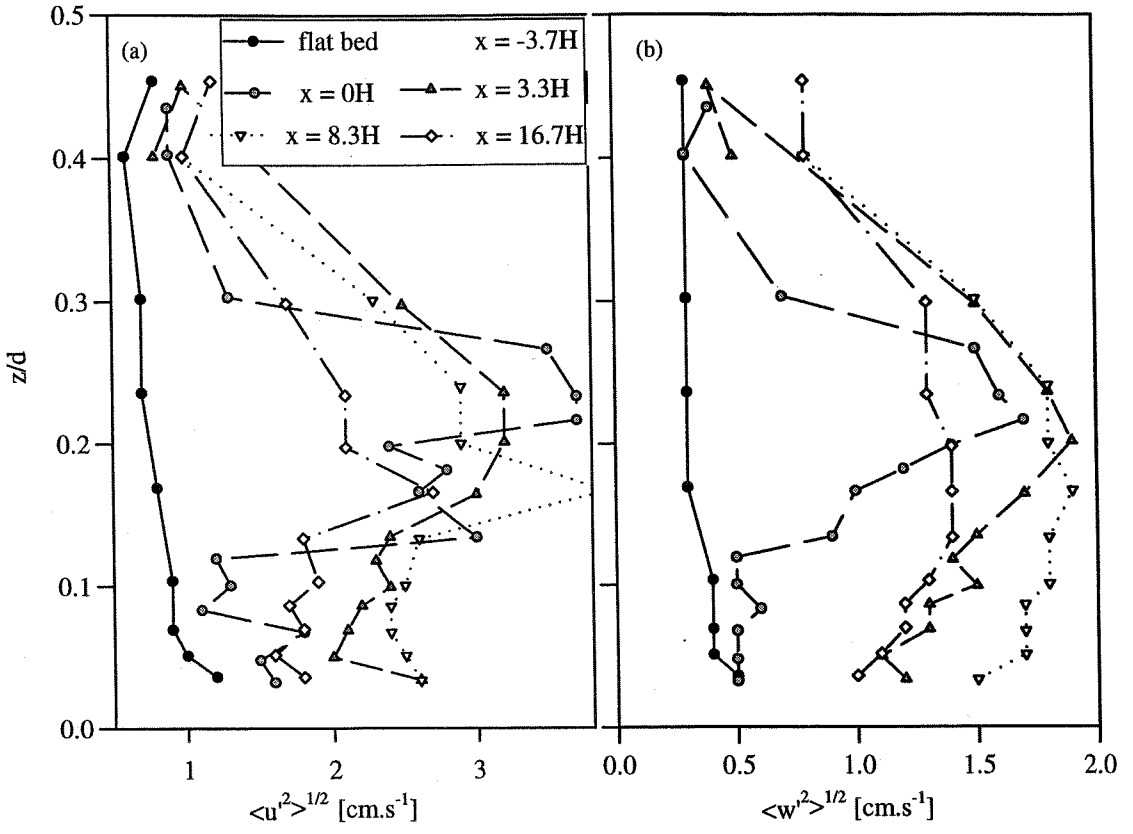

Figure 3-10: Vertical profiles of (a) horizontal and (b) vertical turbulent velocity fluctuations, at different positions from the bedform (along the streamwise Profile J1, Table 3.1).

(ii) Turbulent velocity excursions from the mean and signal intermittence.

Excursions (in terms of magnitude and sign) of the turbulent velocities, u•(t) and w•(t), from the mean, are studied now using the skewness factors (Su• and Sw•, respectively). The velocity signal intermittence (i.e. 'peakiness') is analysed using the kurtosis factors (Ku• and Kw•) (Section 1.3.1(1)). The streamwise variation of these factors, averaged over the entire velocity range sampled at each position, is shown in Figure 3-11.Over the flat bed, Su• is negative and Sw• is positive; the opposite is characteristic of the flow downstream of the bedform (3.3H < x < 16.7H, Figure 3-3) (S u• > 0 and Sw• < 0). This difference indicates that the turbulent velocity

field is dominated by large upward and high-velocity streamwise turbulent flows over the flat bed, whereas it is dominated by large downward low-streamwise velocities downstream of large-scale bedforms. The largest u′ and w′ departures from the mean are reached within the re-circulation region and near the re-attachment point (x = 3.3H and 8.3H). The departures decrease progressively with increasing distance downstream. u′ and w′ velocity signals are highly intermittent in the lee of the bedform and at x = 3.3H; they are, interestingly, slightly less intermittent farther downstream (x ≥ 8.3H), than over flat bed.

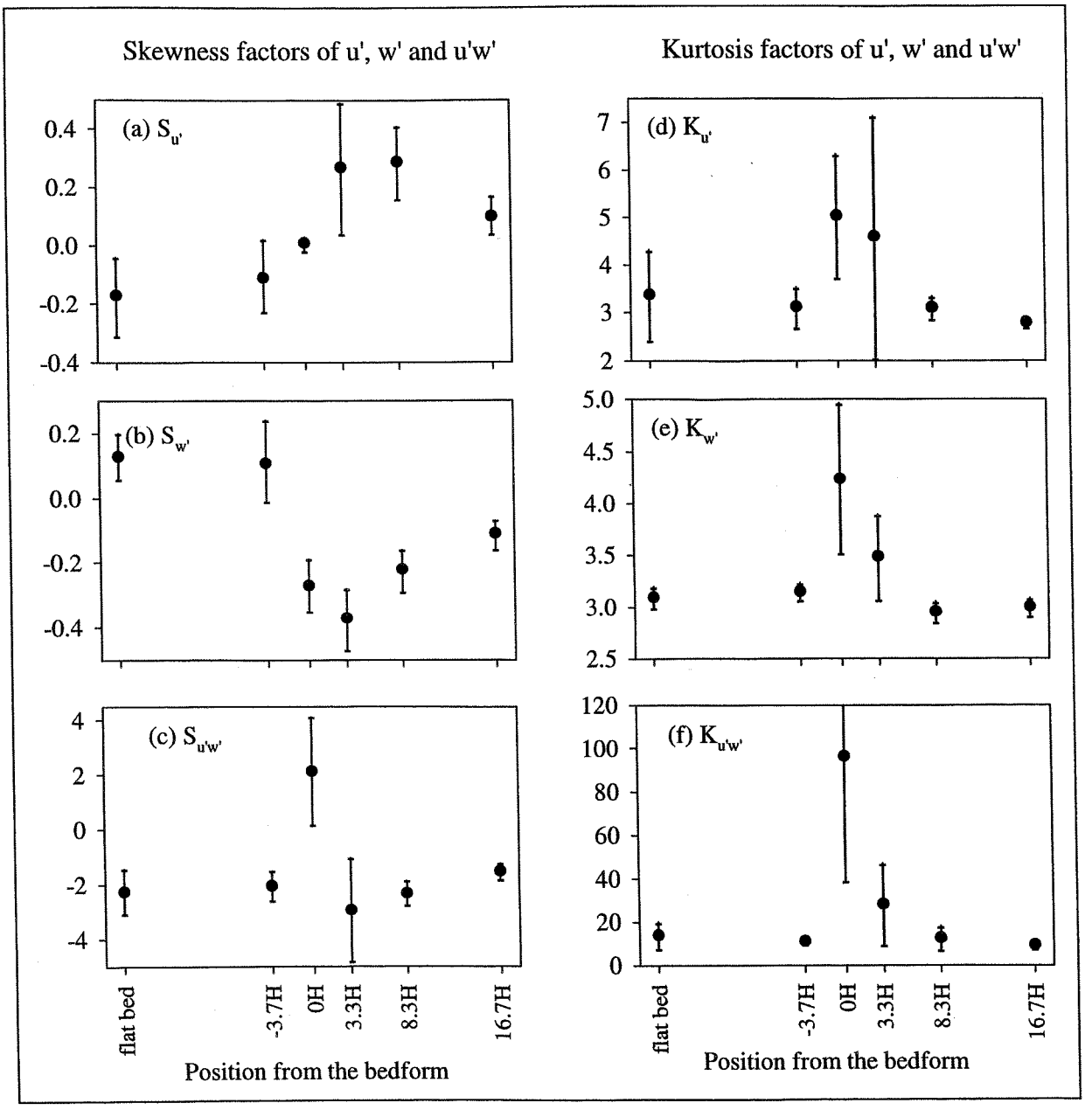

Figure 3-11: Skewness (S_x) and Kurtosis (K_x) factors of the near-bed turbulent velocity field (u' and w') and of the Reynolds stress (u'w'), at different positions from the bedform. The values are averaged over all velocity records, recorded between z= 1 cm and z = 0.10d.

Whereas over the flat bed $S_{u'}$ remains negative throughout the sampled water depth (up to z ~ 0.5d), $S_{u'}$ changes from positive values near the bed, to negative values above z ~ H, at all positions (0H ≤ x ≤ 16.7H). This change indicates a reduction in the u′ excursions from the mean, with height above the bed. It contrasts with the increasing mean turbulent velocities (rms velocities) (Section (i)). Likewise, $K_{u'}$ and $K_{w'}$ generally reach minimum values at z ~ H, although their variation with height is sometimes irregular.

2) The Reynolds stress

(i) Spatial variation

At a given flow speed, the bed shear stress τ_0 ($\tau_0 = -\rho\overline{u'w'}\big|_{z\in CSL}$, where CSL is the constant stress layer) is similar over the flat bed and just upstream of the bedform (Figure 3-12). It decreases in the lee of the bedform (x = 0H) (by 35% to 60%, depending upon the mean flow speed) and increases sharply downstream of the bedform, to reach 3 to 4 times its flat bed value between x = 2.5H and x = 8.3H. τ_0 is still about 3 times the flat bed value at x = 16.7H, at the low speed regimes (U_{1cm} < 15 cm/s). At higher flow regimes (U_{1cm} ~ 20 cm/s), τ_0 is less than twice the τ_0 value over flat bed, suggesting that the far wake flow recovers its 'flat bed' characteristics more rapidly at higher flow regime.

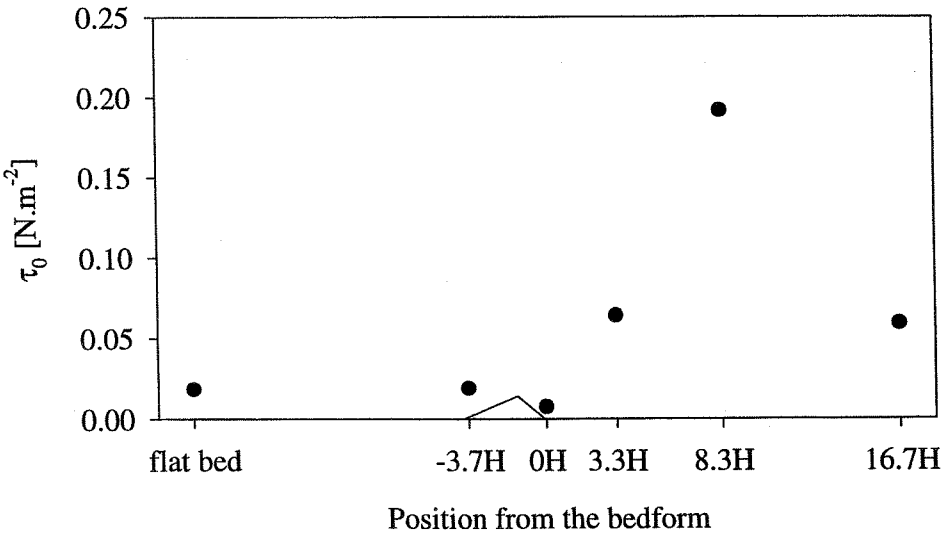

Figure 3-12: Streamwise variation in the bed Reynolds stress τ_0 (Profile J1, Table 3-1).

The magnitude in the Reynolds stress is controlled by the level of turbulent kinetic energy ($\overline{q^2}$) and by the correlation between the turbulent velocity components ($r_{u'w'}$) (Equation 3-2). Within the near-bed layer, the Reynolds stress τ increases linearly with $\overline{q^2}$. A similar increase rate is followed over the flat bed and downstream of the bedform (Figure 3-13(a)), although there is indication that the increase rate is more rapid over the flat bed, than downstream of the bedform.

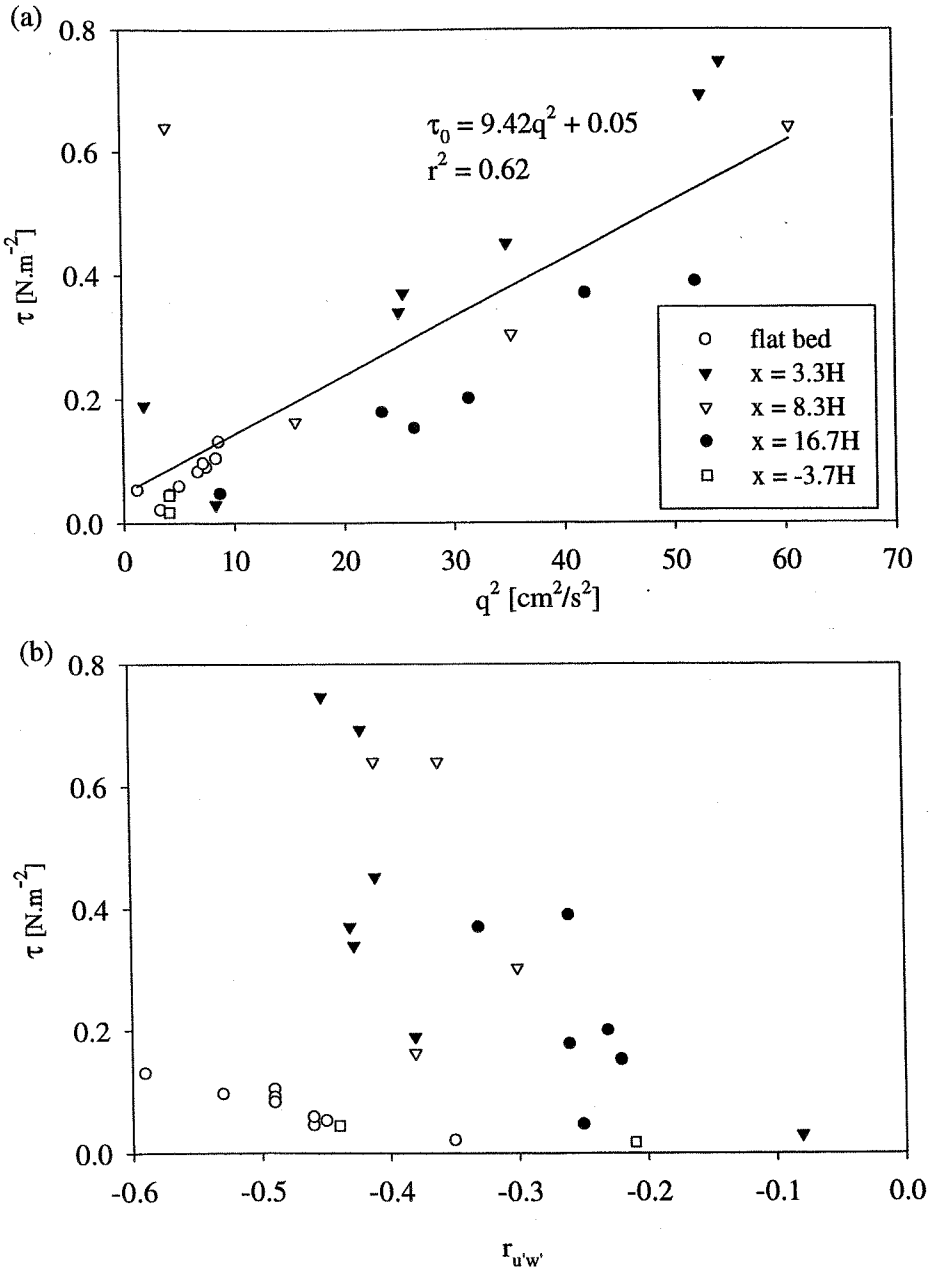

Figure 3-13: Relationships between (a) τ and $\overline{q^2}$ at 1 cm above the bed (the regression line shown is calculated over all the data points (i.e. all locations)); and (b) between τ and $r_{u'w'}$ at 1 cm above the bed.

The relationship between τ and $r_{u'w'}$ (Equation 3-1) (Figure 3-13(b)) is less distinct than the one between τ and $\overline{q^2}$; it differs also strongly over the flat bed condition and at positions downstream of the bedform (where a common trend is apparent for all the sampled positions). This difference reveals that the structure of the Reynolds stress (characterised, here, by the two-dimensional u'-w' correlation coefficient $r_{u'w'}$) is different over a flat bed and downstream of a bedform.

$$r_{u'w'} = \frac{\overline{u'w'}}{\sqrt{\overline{u'^2}}\sqrt{\overline{w'^2}}} \qquad \text{Equation 3-2}$$

(ii) Variation in the Reynolds stress correlation coefficient, $r_{u'w'}$

$r_{u'w'}$ characterises the level of 3-D coherence in the turbulent velocity field: the higher the $r_{u'w'}$ values, the stronger the turbulence vortical structures, compared to non-coherent turbulence (Section 1.2.2). The near-bed layer $r_{u'w'}$ values are always largest over the flat bed (Table 3-4) and lowest within the lee of the bedform, where they approach 0. The correlation coefficient increases towards x = 3.3H, then decreases with increasing distance from the bedform. $r_{u'w'}$ decreases with height above the bed over the flat bed and just upstream of the bedform, but increases with height at all positions downstream of the bedform.

Locations	Flat bed and upstream	X = 0H	3.3H ≤ X ≤ 8.3H	X = 16.7H	X = 21H	X = 25H
$r_{u'w'}$	[-0.49 ; -0.45]	~ 0	[-0.44 ; -0.30]	[-0.26 ; -0.22]	-0.25	-0.30

Table 3-4: Correlation coefficient $r_{u'w'}$ of u' and w' measured over the flat bed and downstream of the bedform. The values were measured within the near-bed layer and include the entire range of flows (Table 3-2).

$r_{u'w'}$ values are close to the values associated with 'classic' flows, over the flat bed and downstream of the bedform, except at x = 0H (Section 1.2.4(6)).

(iii) Excursions from the mean and intermittence in the Reynolds stress signal

In a similar manner to u' and w', the Reynolds stress signal (u'w') is more intermittent and displays larger (negative) excursions from the mean, in the lee of the bedform (0H ≤ x ≤ 3.3H), than elsewhere (Figure 3-11). In the intermediate and far wake regions (x > 8.3H), in contrast with u' and w', u'w' displays smaller excursions (i.e. less negative u'w' magnitudes) than over flat

bed. This pattern results partly from the lower larger participations of the negative-stress events to the total stress, as discussed in the following Section.

3) Scaling of the turbulent velocity field with the Reynolds stress and mean flow speed.

(i) Scaling with the friction velocity: $\sqrt{\overline{u'^2}}/u_*$ and $\sqrt{\overline{w'^2}}/u_*$

$\sqrt{\overline{u'^2}}/u_*$ and $\sqrt{\overline{w'^2}}/u_*$ measured over the flat bed and downstream of the bedform, except at x=0H, occur within narrow ranges, throughout the near-bed layer and at all the flow speeds sampled. Except at x = 0H, the averaged $\sqrt{\overline{u'^2}}/u_*$ values range within [1.8 to 2.3] and the averaged $\sqrt{\overline{w'^2}}/u_*$ range within [1.0 to 1.5]. These values are close to the 'universal' range (Section 1.2.4(4)) (Figure 3-14). Thus, the turbulent motions scale, together with the shear velocity, as in 'classic' uniform flows (except at x=0H). The smaller ratios within the re-circulation region and near the re-attachment point show, however, that the streamwise velocity fluctuations are smaller (by ~ 20%) than that which might be expected in uniform flows. At x = 0H, the ratios are approximately double the 'universal' values, showing that large turbulence fluctuations occur in one direction, but not at the same time in the three directions of space (hence the small Reynolds stress values). This reflects that 'non-three-dimensional-coherent' turbulence dominates.

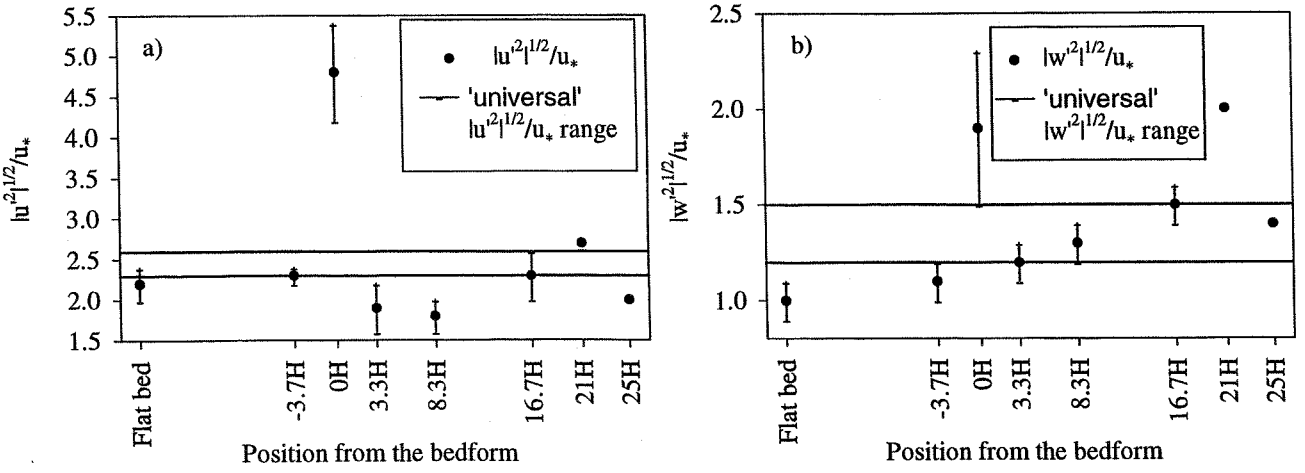

Figure 3-14: Streamwise variation in the turbulent velocity intensities u'/u_* (a) and w'/u_* (b). The 'universal' range, typical in uniform BBL flows, is shown in both graphs. The over-bars represents the standard deviations of the data over the flow speeds sampled (Table 3-2).

(ii) Scaling with the mean flow speed: $\sqrt{\overline{u'^2}}/U$ and $\sqrt{\overline{w'^2}}/U$

In contrast with the previous ratios, $\sqrt{\overline{u'^2}}/U$ and $\sqrt{\overline{w'^2}}/U$ are significantly higher than the 'classic' flow range (Table 1-1) downstream of the bedform, up to x = 16.7H (Table 3-5). Farther downstream (x ≥ 21H), the ratios become close to the 'universal' range. Hence, the turbulence field does not scale with the mean flow velocity as in 'classic' flows, for x ≤ 21H. The small standard deviation in the ratios, over the entire velocity range, indicates that a particular equilibrium sets up between the turbulence and the mean flow, at each position downstream of the bedform.

	Flat bed	X=-4H	X=0H	X=3.3H	X=8.3H	X=16.7H	X = 21H	X = 25H
$\sqrt{\overline{u'^2}}/U$	0.09 ± 0.01	0.14 ± 0.03	0.59 ± 0.08	0.70 ± 0.06	0.61 ± 0.08	0.23 ± 0.05	0.14	0.13
$\sqrt{\overline{w'^2}}/U$	0.04 ± 0.01	0.05 ± 0.01	0.23 ± 0.04	0.46 ± 0.06	0.44 ± 0.05	0.15 ± 0.03	0.08	0.07

Table 3-5: Ratios of streamwise and vertical rms velocities, to mean flow velocity averaged over the near-bed layer at different positions from the bedform, for all the flow regimes (Table 3-2).

(iii) Scaling of the total turbulent kinetic energy: $-\overline{u'w'}/\overline{q^2}$ ratio

The ratio of shear stress to total turbulent kinetic energy $-\overline{u'w'}/\overline{q^2}$ is surprisingly close to the 'flat bed' values, at positions between x = 3.3H and x = 8.3H. Farther downstream, the ratio becomes smaller (by ~ 35%), following the decrease in the Reynolds stress (compared to the vertical velocity fluctuations discussed in Section (i)). At x = 0H, the ratio is approaching zero (Table 3-6). All $-\overline{u'w'}/\overline{q^2}$ values are close to the 'universal' Reynolds stress to TKE ratio proposed by Soulsby (1983), for uniform BBLs (where $\tau = 0.19\rho TKE = 0.095\overline{u'w'}\overline{q^2}$, Section 1.6.2(4)). The much smaller ratios at x = 0H, suggest that 'chaotic' turbulence (high velocity fluctuations and relatively weak u'-w' coherence) dominates in the lee of the bedform. The results obtained by Towsend (1976) (Section 1.3.5), suggest that the smaller ratios measured downstream of the re-attachment point in comparison to the flat bed, result either from a higher pressure gradient, or less homogenous turbulence.

Position	Flat bed	X=-4H	X=0H	X=3.3H	X=8.3H	X=16.7H	X = 21H	X = 25H
$-\overline{uw}/\overline{q^2}$ $(=0.5\times\tau/TKE)$	0.12 ±0.02	0.08 ±0.04	0.01 ±0.01	0.12 ±0.03	0.12 ±0.02	0.09 ±0.02	0.07	0.08

Table 3-6: Ratio of the shear stress to total turbulent kinetic energy, within the near-bed layer.

4) Comparison of bed shear stress estimates from different models

The eddy-correlation technique (Reynolds stress) is the most direct method available to estimate the bed shear stress (Section 1.6.2). Complete information on the turbulence field is not, however, always available e.g. in numerical models (which do not provide full solutions of the turbulence motions), or when two-dimensional or low sampling frequency velocity probes are used. Other techniques, described in Section 1.6.2, may be applied: the Law of the Wall (LW), the inertial dissipation method (ID) or the TKE method. Therefore, it is important to determine how these estimates compare to each other, downstream of large-scale bedforms.

(i) Limitations in the methodology

In the lee of the bedform and in the re-circulation region (x = 0H and 3.3H), the LW method cannot be applied, since a logarithmic profile cannot be measured. The TKE and Reynolds bed shear stress estimates are obtained by averaging the stress values, throughout the constant stress layer. At locations where the constant stress layer is absent or too thin to be measured, the bed shear stress (τ_0) value is taken as the value measured at z = 1 cm above the bed. This approach assumes that the shear stress is constant below this height and equal to the bed shear stress. The ID method is applied using the vertical and horizontal velocity spectra of the near-bed layer, where the spectra follow a '–5/3' slope, within the inertial sub-range. The inertial sub-range is determined by estimating the scale separation between energy production and dissipation, using the expressions of Corrsin (1958) and Soulsby (1983) (Equations 1.23 to 1.25). The range of wavenumbers where those conditions are respected is limited by the resolution range of the ADV. The wavenumber limits, estimated for minimum and maximum flow discharge rates and within the near-bed layer, are presented in Table 3-7. Corrsin's equations indicate a significant scale separation between the production and the dissipation of turbulent energy. The approximation of the production wavenumber by Soulsby (1983) provides a much narrower range.

The characteristic '-5/3' slope, of the velocity spectra in the inertial sub-range, is followed generally at all positions, except near the re-attachment point. The higher resolvable wavenumber obtained by the ADV, is controlled usually by the size of the sampling volume D

(D=9x10^{-3} m): for a signal attenuation of less than 50%, $k_{max} \approx 2\pi/2.2D \approx 317$ m^{-1} (Soulsby, 1983). The sampling frequency (25 Hz) becomes the limiting factor only at the largest flow velocities (U > 0.25 m/s). The lower resolvable wavenumber is determined by the length of the sampling period T; in the present investigation, it is never a limiting factor. The results obtained suggest that a resolvable inertial sub-range exists within the near-bed layer, except near the re-attachment point. However, this range is very narrow at the position nearest to the bed (z=0.01 m), if Soulsby's expression for the energy production wavenumber is used.

Z [cm]	k_{min} [m^{-1}]			k_{max} [m^{-1}]		
	Sampling period	Energy production		ADV averaging volume	Sampling frequency	Energy dissipation
	$\frac{2\pi z}{TU}$	$\left\|\frac{dU}{dz}\right\|\left(\overline{u'^2}\right)^{1/2}$	$\frac{\pi}{z}$	$\frac{2\pi}{2.2D}$	$\frac{2\pi F_s/2}{U}$	$0.1k_\kappa$
1.0	8 x10^{-3}	70	314	317	1963	2327
2.0	35 x10^{-3}	10	157	317	> 317[*1]	2327

Table 3-7: Wavenumber limits of the inertial sub-range and of the resolvable range by the ADV, at 2 heights within the near-bed layer. The k_{min} values correspond to the minimum k_{min} values estimated at all flow regimes and positions from the bedform; the k_{max} values correspond to the maximum k_{max} values computed. T = velocity record length.

(ii) Inter-comparisons

Estimates of the bed shear stress (τ_0) using the three methods, are shown in Figure 3-15, for the different sampled positions and mean flow speeds.

The results obtained by the Reynolds stress and TKE methods agree well at all of the positions, except at x = 0H. This agreement results from the $-\overline{u'w'}/\overline{q^2}$ values (Table 3-6) being similar to the 'classic' flow value used in the TKE method to estimate τ (as discussed above). Table 3-6 indicates that the TKE method value of '0.19' represents an appropriate average for the streamwise profile, upstream and downstream of a bedform. The Reynolds and TKE method τ_0 values increase with the mean flow speed, as in 'classic' flows.

The LW τ_0 estimates are similar to the Reynolds stress values, only over the flat bed. Upstream of the bedform, the Law of the Wall provides significantly higher τ_0 values than the Reynolds stress, particularly at the smallest velocity regime. In contrast, at all locations downstream of the re-circulation zone, LW provides τ_0 values which are 50 to 90 % lower than those derived on the basis of the Reynolds stress, with the differences decreasing with distance from the bedform (Figure 3-15).

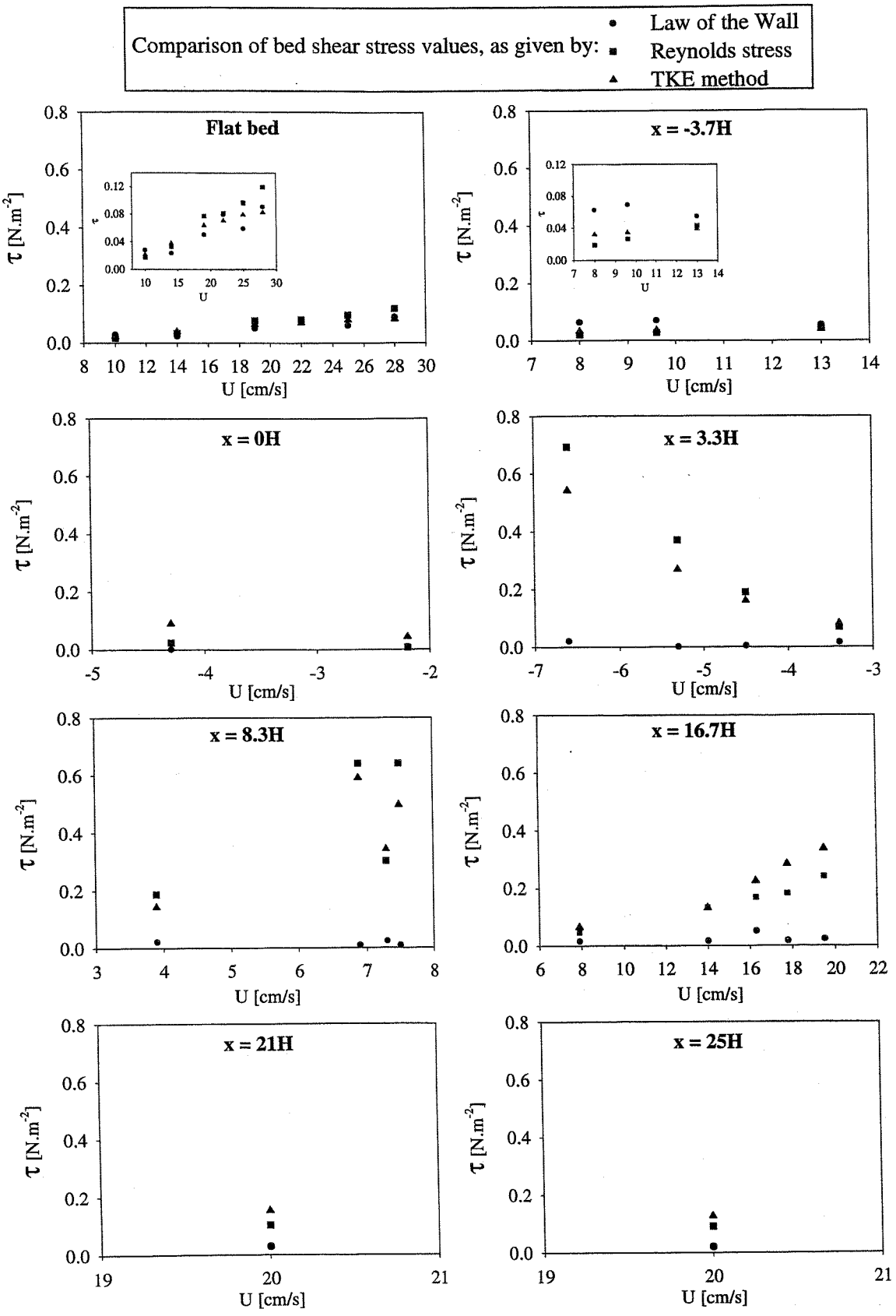

Figure 3-15: Bed shear stress estimated on the basis of the Reynolds stress, the Law of the Wall and the TKE methods, at different positions from the bedform and for different mean velocities.

Downstream of the bedform, the LW τ_0 is not related positively to the mean flow speed. Large differences exist, even at x=16.7H, where a well-developed logarithmic layer exists. These results demonstrate that the turbulence structures forming the Reynolds stress are not directly related to the shearing of the mean horizontal velocity, up to large distances downstream of the bedform. The higher Reynolds stress τ_0 than the LW $\tau_{0'}$ indicates that Reynolds stress is not only produced from the mean shear, but also from bottom friction effects. Kelvin-Helmhotz instabilities developing along the vortex lines of the free-shear layer, constitute probably an additional source of Reynolds stress production. The higher LW τ_0 values just upstream of the bedform, can be attributed to flow obstruction effects induced by the bedform. The horizontal velocity is more obstructed near the bed (since the bedform is closer to the measuring point) than higher above the bed where the flank of the bedform is farther downstream. This interruption increases the vertical variation of horizontal velocity and, hence, the LW $\tau_{0'}$ compared to the velocity variation induced by bottom drag effects only.

The ID τ_0 values are always much higher than the other stress estimates, even over the flat bed (60% to 150% larger). The differences are larger when using the vertical velocity (see section 1.2) than when using the horizontal velocity; this reflects the turbulence anisotropy in the flume. The large ID τ_0 values show that energy is not dissipated solely through bottom friction, but that other sources of turbulence exist in the flume, such as sidewall friction. The absence of a true inertial sub-range *i.e.* of a sufficient energy production and dissipation scales separation, is believed to invalidate the application of the ID method to velocity records obtained in the flume.

5) The bursting events

(i) Mean characteristics and spatial variation

The characteristics of the 4 bursting events (ejection, sweep, outward interaction (OI) and inward interaction (II)) are analysed in detail now, using the method of Gordon and Witting (1977) as modified by Soulsby (1983) (Section 1.2.3 (iii)). The characteristics determined at each position, include: (i) stress magnitude of each bursting event $-\rho\overline{u'w'}_{event}$, normalised by the total stress (Figure 3-16); (ii) duration of each bursting event (Figure 3-16); (iii) total period of time occupied by each bursting event (Table 3-8); and (iv) contribution of each bursting to 90% of the total stress τ (Table 3-9). The values are averaged within the near-bed layer (z<0.10d), where the bursting parameters remain approximately constant, over the velocity range sampled, at each position (Table 3-2). Since similar bursting characteristics are measured upstream of the bedform to those over the flat bed, the 'upstream' data are not presented in this Section.

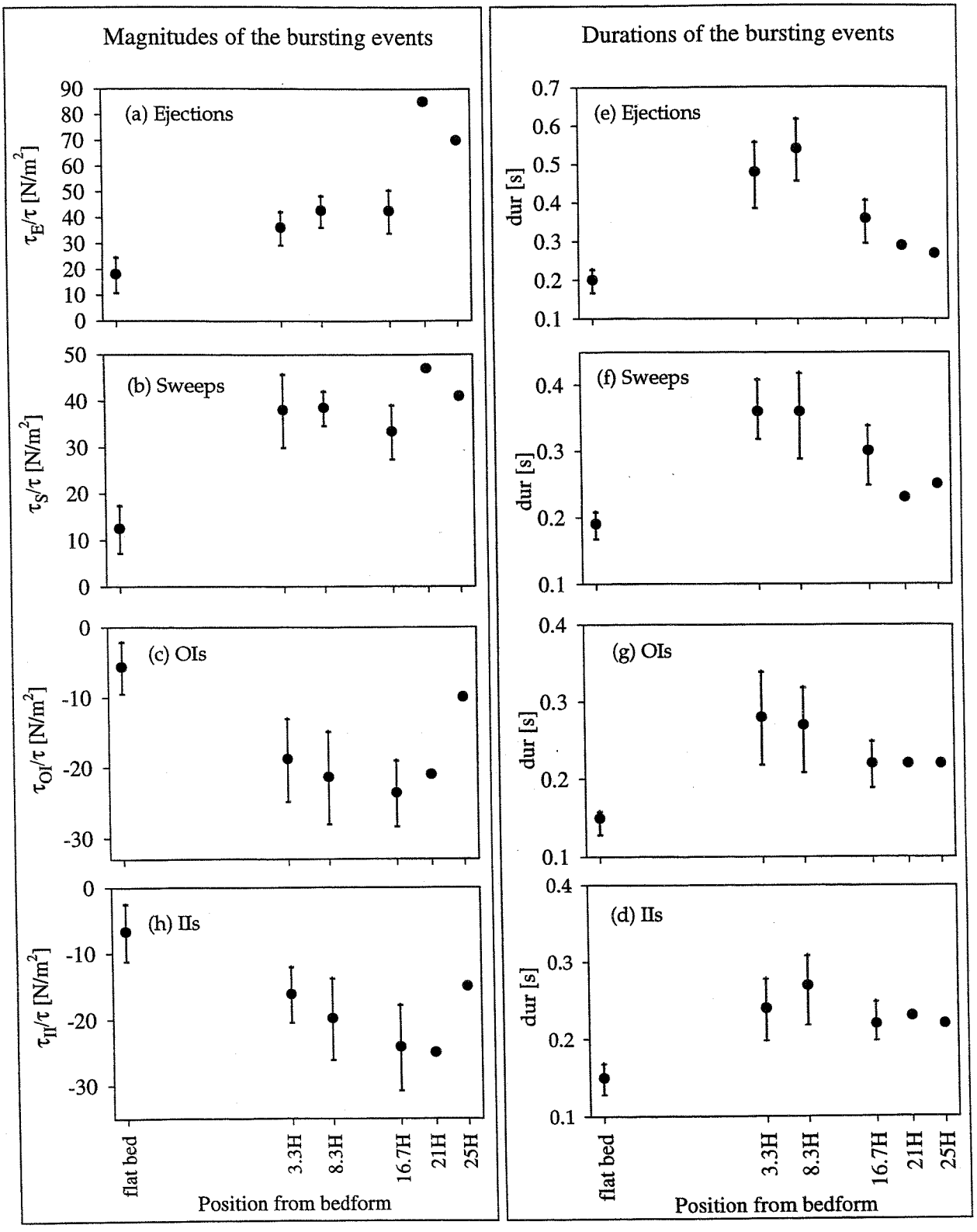

Figure 3-16: a to d: Mean stress magnitude ($-\rho\overline{u'w'}$) of each bursting event, normalised by the total stress, measured at each position from the bedform. e to h: mean duration of the 4 bursting events at each position from the bedform. All data are averaged over all velocity records collected in the near-bed layer (Table 3-2).

There were no bursting events detected in the lee of the bedform (x = 0H). This absence reflects the small $r_{u'w'}$ values, resulting from the absence of significant mean flow shear in this region (which controls the generation of turbulent structures). Farther downstream (x ≥ 3.3H), the bursting events are 3 to 4 times as strong and as long than those over the flat bed (Figure 3-16). Sweeps reach their maximum magnitude (compared to the total stress τ) and maximum duration, near at the re-attachment point: the other bursting events reach their maxima farther downstream (x ≥ 16.7H). As a result, τ is produced in less time downstream of the bedform than over the flat bed (Table 3-8).

Position from the bedform	Time (in %) occupied by each bursting event				Total time (in %) occupied by all 4 events
	Ejections	Sweeps	OI	II	
Flat bed	17 ±2	18 ±3	3 ±2	3 ±2	41
X=3.3H	14 ±1	14 ±1	2 ±1	2 ±1	32
X=8.3H	13 ±2	13 ±1	3 ±1	2 ±1	31
X=16.7H	13 ±2	12 ±1	3 ±1	3 ±1	31
X = 21H	11	8	4	4	27
X = 25H	12	9	4	4	29

Table 3-8 : Percentage of time occupied by the 4 bursting events, in the near-bed velocity time-series (0.03d<z<0.10d), over the flat bed and downstream of the bedform. The values are averaged over all the velocity records collected within the near-bed layer (Table 3-2).

The small standard deviations of the averaged event magnitudes and durations, over the entire velocity range and at each position, indicate that the bursting process varies little with the mean flow speed. The relative contributions of the bursting events to τ vary with distance from the bedform. The contribution of sweeps increases by 40% to 60%, downstream of the bedform, compared to the flat bed conditions (Table 3-9). In contrast, the relative contribution of ejections decreases by about 20% from the lee-side of the bedform, up to the re-attachment point. The contribution increases then rapidly (by about 40%) in the far wake region; it becomes equivalent, or higher, for x ≥ 16.7H, than the sweep contributions. The contributions of OIs and IIs increase constantly from the flat bed to the lee region, up to distances of 21H downstream of the bedform. At this latter location, their contributions are about 4 times those obtained over the flat bed.

The ratio of the sum of the contributions of OI and II to τ (which contribute negatively to τ), over the sum of the contributions of ejections and sweeps to τ (which contribute positively to τ), $(OI_{\%\tau} + II_{\%\tau})/(E_{\%\tau} + S_{\%\tau})$, increases downstream of the bedform (Table 3-9). The increase in the negative stress events compared to the positive stress events, reduces the Reynolds stress values. Hence, lower Reynolds stress values are measured downstream of a large-scale bedform, than

those expected from: (i) the mean flow speed; (ii) the general turbulence level; and (iii) the stress contributions of ejections and sweeps. This aspect is important to take into account for the modelling of turbulence and for the prediction of sediment transport, based upon the Reynolds stress value.

Position	% of contribution of each bursting event to τ				
	$E_{\%\tau}$	$S_{\%\tau}$	$OI_{\%\tau}$	$II_{\%\tau}$	$(OI_{\%\tau}+II_{\%\tau})/(E_{\%\tau}+S_{\%\tau})$
Flat bed	55 ±8	40 ±4	-4 ±3	-5 ±3	8 ±5
X=3.3H	44 ±3	58 ±5	-6 ±2	-6 ±2	11 ±3
X=8.3H	46 ±7	63 ±10	-11±9	-8 ±7	16 ±10
X=16.7H	63 ±11	55 ±8	-13 ±5	-14 ±8	22 ±8
X = 21H	88	47	-21	-25	34
X = 25H	79	41	-13	-16	24

Table 3-9: Contributions of each bursting event to the total stress τ, in the near-bed layer (0.03d<z<0.10d), over the flat bed and downstream of the bedform. The values are averaged over all the velocity records collected within the near-bed layer (Table 3-2).

(ii) Vertical dissipation of the bursting events

Over the flat bed and in the far wake region, the magnitude of the 4 bursting events remain relatively constant over the bottom layer, within the water column, up to z = 0.2-0.3d above the bed (Figure 3-17). In contrast, within the re-circulation region (x = 3.3H), and to a lesser extent near the re-attachment point, the magnitudes of the 4 bursting events increase upward; they reach a maximum at around z = 0.15-0.2d above the bed. This pattern favours the vertical mixing of sediments.

6) Modulation of the bursting process by macro-turbulence

The majority of the sweeps (~80%) and OIs (~75%) are associated with high-streamwise speed macroturbulent structures ($U_{macro} < 0$) (Figure 3-18). Most of the ejections (~80%) and IIs (~70%), in contrast, occur within the macro-scale features of low-streamwise current speed ($U_{macro} < 0$). The percentages of occurrence of the 4 bursting events during macro-scale flow structures of high and low horizontal current speed (compared to the mean current speed), are similar over the flat bed and at all positions in relation to the bedform (Figure 3-18). The mean magnitude and duration of the ejections, and to a less extent of the IIs, are smaller during $U_{macro}>0$ than during $U_{macro}<0$ (Figure 3-19). In opposition, the mean magnitude and duration of sweeps and, to a less extent, of OIs, are larger during $U_{macro} > 0$ than during $U_{macro} < 0$. The differences in the bursting events characteristics between $U_{macro}>0$ and $U_{macro}<0$, are larger downstream of the bedform, than over the flat bed.

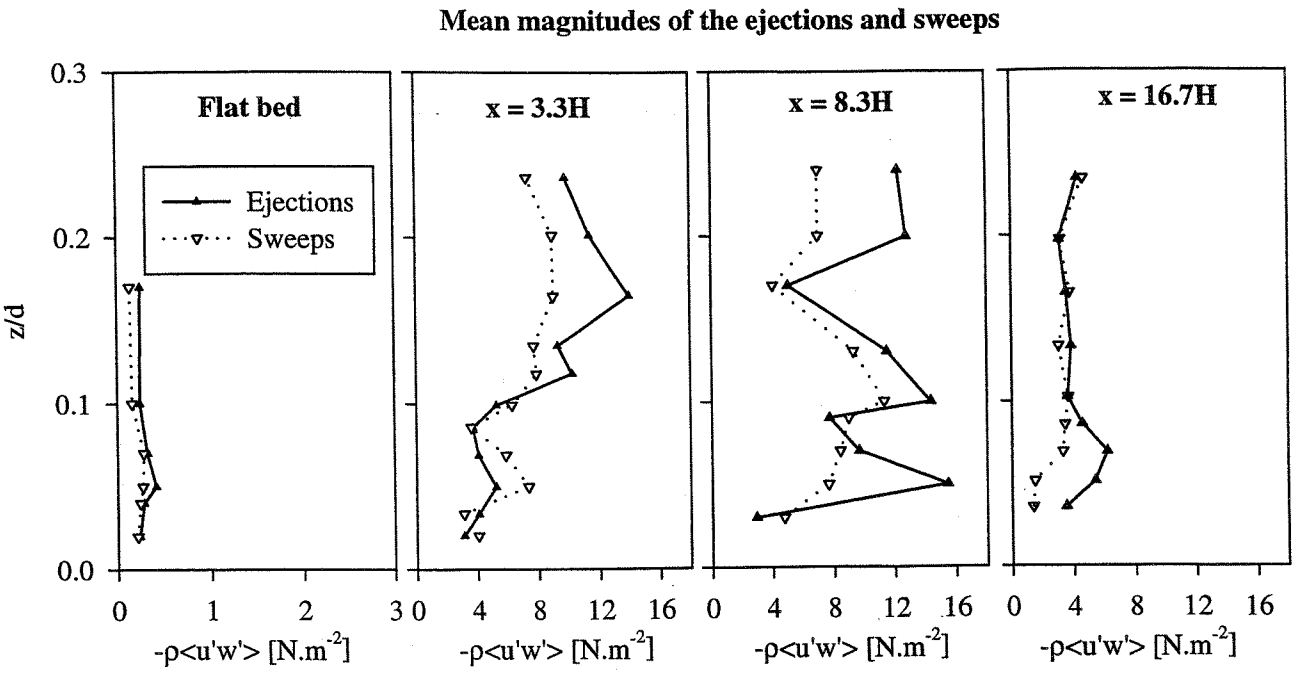

Figure 3-17: Typical vertical variation in the magnitude of the ejections and sweeps, over the flat bed and downstream of the bedform (streamwise profile J1).

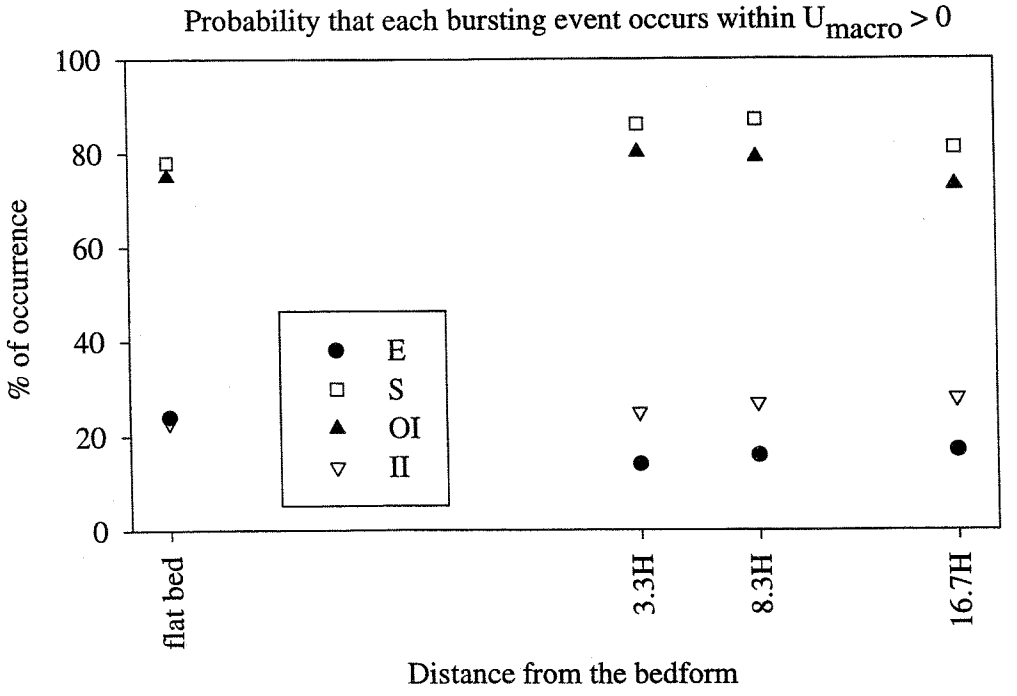

Figure 3-18: Percentages of occurrence of each bursting event, within the macro-turbulence structure of high streamwise current speed. The values are averaged over all the records collected in the near-bed layer (0.03d<z<0.10d).

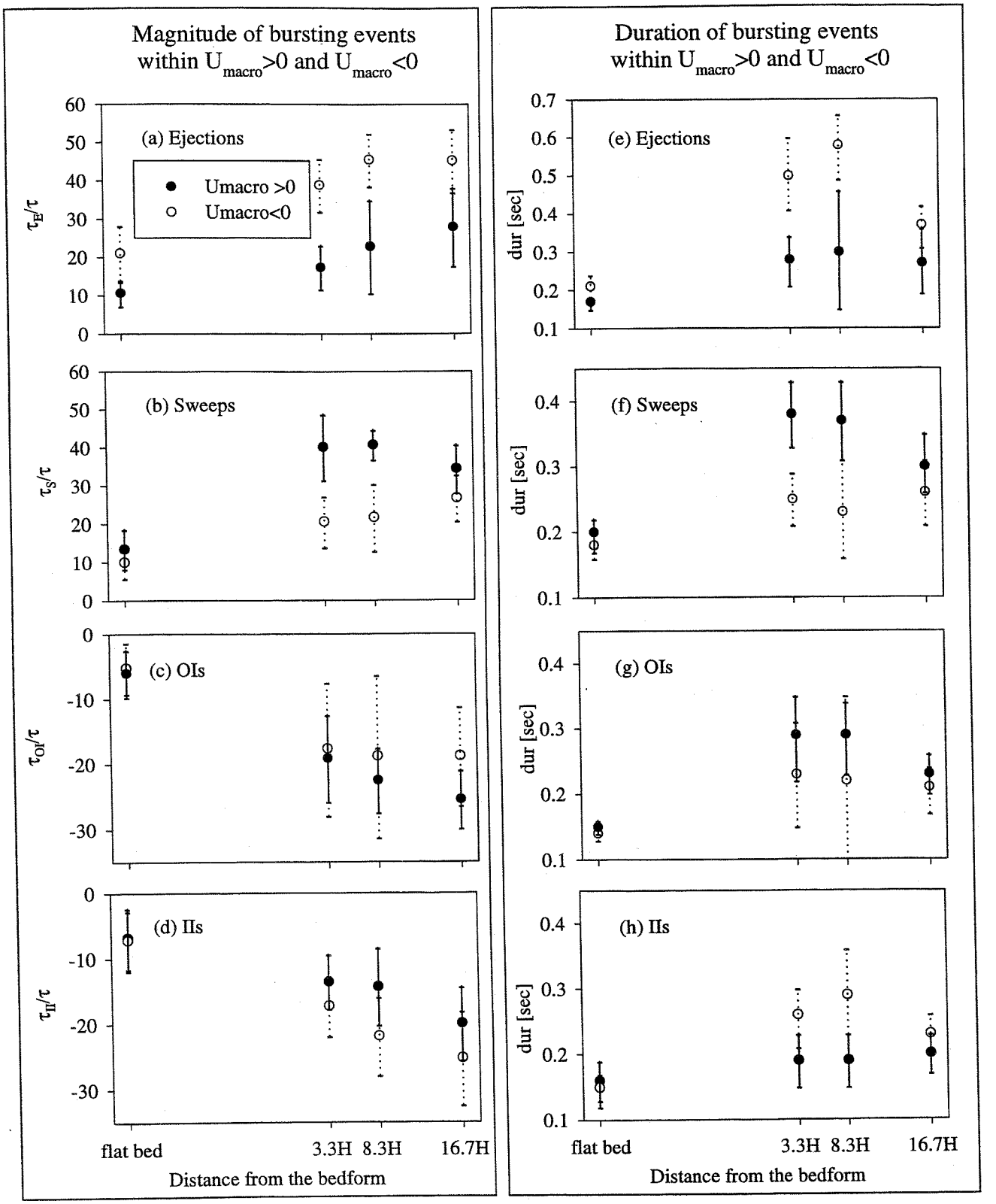

Figure 3-19: Mean magnitude of each bursting event stress contributions, normalised by the total stress (a to d) and the mean duration of each bursting event (e to h), within the macro-turbulence structures of high and low streamwise current speed. The values are averaged over all the velocity records collected within the near-bed layer (0.03d<z<0.10d).

3.2.5 Hydrodynamic control of bedload transport

1) Characteristics of the bed sediment movements

The critical mean flow speeds for sand and gravel movement are significantly lower downstream of the bedform than over the flat bed, even at x = 16.7H. Hence, the threshold for gravel movement initiation could not be obtained (within the flume) over the flat bed; however, it could be reached easily at any of the locations downstream of the bedform. The sediment grains moved differently over the flat bed than downstream of the bedform. Over the flat bed, the sediment grains moved mainly by rolling or small saltations, but were rarely re-suspended. The grains moved essentially in the direction of the flow, so that the sediment was transported away rapidly from the sediment (test) section area. The transition between rare individual movements and continuous 'sheet' grain movements (where surface grains are moving almost continuously, throughout the sediment (test) section area) was very rapid. In contrast, downstream of the bedform, re-suspension events were not infrequent: both the bedload and re-suspension movements involved usually many grains simultaneously, even at low flow regimes. The movements were more intermittent than over the flat bed, for a wide range of mean flow discharge and occurred in every direction: almost equally in all directions near the re-attachment point; dominantly upstream before the re-attachment point; and dominantly downstream after the re-attachment point. Such 'multi-directional' movements slowed down greatly the removal of the material from the sediment (test) section: departures of grains from any point were compensated by the arrival of new material from another location. The more intermittent and larger movements downstream of the bedform, in comparison to those over the flat bed, occurred even in the far wake region, where: (i) the turbulent motions were less intermittent than over the flat bed; and (ii) the skewness factors of the Reynolds stress and of the vertical velocity fluctuations, were also smaller than over the flat bed, revealing less large positive excursions from the mean. This type of movement can only be explained in terms of the large positive skewness factor of the streamwise turbulent velocity. This observation supports the hypothesis proposed by Thorne *et al.* (1989), that the streamwise velocities have a dominant control on bedload transport (Section 1.5.2).

The lower mean speed required for the initiation of sediment movement downstream of the bedform, in comparison to over the flat bed, results from the larger magnitudes of the turbulent velocities and bursting events in this region. The 'grouped' sediment grain movements reflect the larger bursting event durations (and, hence, the bursting structure sizes) acting on the bed, downstream of the bedform. Multi-directional transport is generated by the increased vertical and cross-stream turbulent velocities downstream of the bedform; these are otherwise small, compared to the streamwise turbulent velocities over the flat bed. The higher intermittence of bedload movements downstream of the bedform opposes the lower intermittence of the

turbulent velocity signal at $x \geq 8.3H$ (Section 3.2.4(1)).

2) Turbulent velocity signals associated with bedload movements

In this Section, only the ADV records collected during the sediment transport observations are analysed; this ensures a more accurate correlation between the sediment transport and the hydrodynamic parameters.

Five types of velocity signals characterise the records, at the time of the sediment movements: individual ejection; sweep; OI; II; or multiple (usually 2 or 3) bursting events occurring in various sequences.

The percentages of movements associated with the different turbulent velocity signals are surprisingly similar for the sand and gravel particles (Table 3-10). This observation contrasts with the concept that the mechanisms for the initiation of movement differs for small and large particles (Sechet, 1996). Given this similarity, the discussion is based on averages of the results obtained over both sand and gravel beds.

Position	% of sand and gravel movements associated with each of the velocity signals									
	E		S		OI		II		Multiple uw	
	S	Gr	S	Gr	S	Gr	S	Gr	S	Gr
Flat bed	14	-	55	-	3	-	4	-	24	-
X=3.3H	16	17	62	52	6	11	7	10	9	10
X=8.3H	13	13	64	62	5	3	5	3	13	18
X=16.7H	21	22	55	55	7	11	4	0	13	12

Table 3-10: Percentage of sand (S) and gravel (Gr) movements associated with different turbulent velocity signals in the near-bed layer records (see text above).

The percentage of the sediment movements associated with each velocity signal, within the near-bed layer and within the upper layer, are similar at all positions downstream of the bedform and over the flat bed (Figure 3-20). The contribution of sweeps increases slightly near the re-attachment point and decreases farther downstream; ejection contributions follow the opposite trend. However, the general similarity of the percentages is an important result in terms of the modelling of sediment dynamics processes; it indicates that the mechanisms initiating sediment movements are similar in uniform flows, over flat beds, and in non-uniform flows downstream of bedforms.

Within the near-bed layer, sweeps are the dominant bursting event associated with sediment movements, over the flat bed and downstream of the bedform (Tables 3-10 and 3-11); they generate about 57% of all the movements. Ejections are the second largest contributing event,

generating, on average, 17% of the sediment movements (Figure 3-20). OIs and IIs are related weakly to bed sediment movements. About 14% of all sediment movements are associated with multiple Reynolds stress peaks *i.e.* with 2, or more, successive bursting events. This percentage is higher over the flat bed than downstream of the bedform.

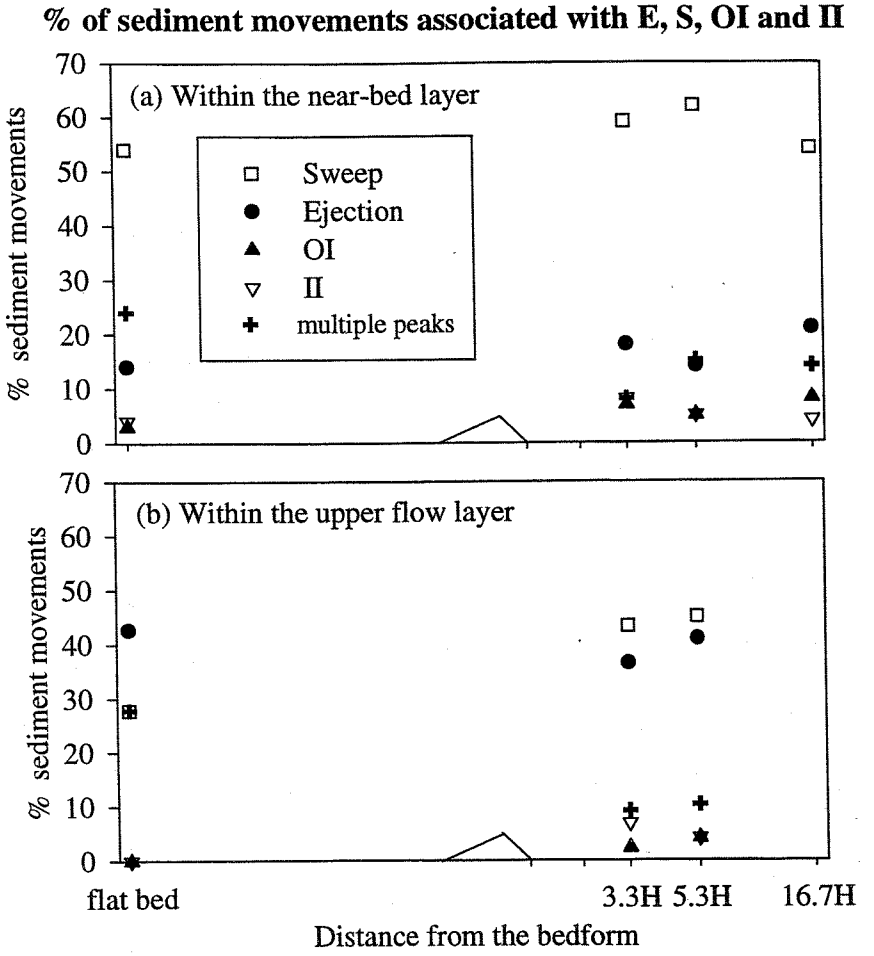

Figure 3-20: Percentage of the sediment movements associated with each bursting event and with multiple Reynolds stress peaks: (a) within the near-bed layer ($0.03d \leq z \leq 0.10d$); and (b) within the upper layer ($0.15d<z<0.35d$) (Figure not in scale).

Within the velocity records collected higher above the bed ($0.20d<z<0.35d$) (Table 3-11), the proportion of sediment movements associated with a clear velocity signal is reduced, compared to that within the near-bed layer. Within the 'clear velocity signal' data set, sweeps and ejections contribute equally to sediment movements. The decrease in the contributions of the sweeps to bed sediment transport, together with the increase in the ejection contribution, with increasing height above the bed, result probably from the fact that the sweeps are only strong near the bed; in contrast, the ejections can penetrate into high regions of the flow, with little dissipation (Grass,

1971). The strength of the ejection-flow, penetrating into the upper flow, is illustrated in Figure 3-5. The percentages of sediment movements associated with OIs and IIs, in the upper layer velocity records, remain small.

% of sediment movements associated with each velocity signal averaged over all positions relative to the bedform					
Flow layer	Ejection	Sweep	OI	II	Multiple uw
Near-bed layer	17 ± 5	57 ± 3	6 ± 3	6 ± 2	14 ± 8
Upper layer	41 ± 8	39 ± 8	2 ± 1	2 ± 2	16 ± 12

Table 3-11 : Percentages of sediment movements associated with each bursting event and with multiple stress peaks, within the near-bed layer and within the upper layer. The values are averaged over all the positions downstream of the bedform and over the flat bed.

Downstream of the bedform, most of the re-suspension events (50%) are generated by sweep events (Table 3-12). Given the small number of re-suspension events observed over the flat bed, re-suspension processes are not analysed for the flat bed conditions. The control of re-suspension by ejections contrast with previous suggestions, where the role of ejection in generating bed sediment re-suspension has been proposed (e.g. Sumer and Deigaard, 1981; Garcia *et al.*, 1996 (Section 1.4)). However, the number of resuspension events observed in the current work is small (46 events); thus, the results must be considered cautiously.

The reasons why the sweeps are associated dominantly with bed sediment movements may result from:

(i) the highest efficiency of the sweeps in moving bed sediment; or

(ii) the dominant occurrence of sweeps in the velocity records, compared to that of ejections, OIs and IIs.

% of re-suspension events associated with each velocity signal, within the near-bed and upper flow layers.					
Flow layer	Ejections	Sweeps	OI	II	Multiple uw
Near-bed layer	16	66	4	3	11
Upper layer	32	67	2	6	2

Table 3-12 : Percentage of resuspension events associated with each bursting event in the near-bed layer ($0.03d<z<0.10d$) and in the upper flow layer ($0.15d<z<0.35d$). The values are averaged for all of the positions downstream of the bedform.

To examine this particular process, the frequencies of occurrence of each bursting event are compared with the percentages of sediment movements associated with each of the bursting

events. To facilitate the comparison between the sweeps and the other bursting events, the following approach has been adopted:

(i) the frequencies of occurrence of the bursting events have been divided by the frequency of occurrence of the sweeps; and

(ii) the percentages of sediment movements associated with each bursting event have been divided by the percentage associated with the sweeps.

The results obtained, presented in Table 3-13, are summarised below:

(i) Ejections and sweeps occur with a similar frequency, but the contributions of the ejections to sediment movements are always about 3 times less than that of the sweeps.

(ii) The frequencies of occurrence of the sweeps is smaller downstream of the bedform, than over the flat bed; they decrease with increasing distance from the bedform (from x=3.3H to 16.7H), but the percentages of sediment movements attributed to the sweeps remain constant (range between 34 and 39%).

(iii) Sweeps occur some three to six times as frequently than the OIs or IIs; however, the percentages of sediment movements associated with the sweeps are about 10 times more than the percentages associated with OIs or IIs.

Position	Ratios of frequencies of occurrence of bursting events			Ratios of % of sediment movements, associated with bursting events		
	E_{freq}/S_{freq}	OI_{freq}/S_{freq}	II_{freq}/S_{freq}	E_{sed}/S_{sed}	OI_{sed}/S_{sed}	II_{sed}/S_{sed}
Flat bed	1.0	0.2	0.2	0.3	0.1	0.1
X=3.3H	1.1	0.3	0.2	0.3	0.1	0.2
X=8.3H	1.1	0.2	0.2	0.2	0.1	0.1
X=16.7H	1.1	0.4	0.3	0.4	0.2	0.1

Table 3-13 : The 3 columns on the left-hand side: ratios of the frequency of occurrence of ejections, OI and II, over that of sweeps (E_{freq}/S_{freq}, OI_{freq}/S_{freq} and II_{freq}/S_{freq} respectively). The 3 columns on the right-hand side: ratios of the percentage of sediment movements associated with ejections, OI and II, over that associated with sweeps (E_{sed}/S_{sed}, OI_{sed}/S_{sed} and II_{sed}/S_{sed} respectively). Legend: sed. mvts = sediment movements

These observations indicate that the relationships between sweeps and sediment movements are not related to the relative frequency of occurrence of the bursting events. However, to investigate if the larger contribution made by the sweeps to sediment movements is due to their higher efficiency in moving bed sediments, the magnitude and duration of the sweeps are compared with those of the 3 other bursting events. The following comparative ratios are used: (i) the mean magnitudes of ejections, OIs and IIs, divided by the mean magnitude of the sweeps; and (ii) the mean duration of ejections, OIs and Iis, divided by the mean duration of the sweeps (Table 3-14).

The results obtained demonstrate a number of observations, as outlined below:

(i) The sweep structures last slightly longer than the OI and II structures (sweeps last 10% to 20% longer than OIs and 10% to 30% longer than IIs). The sweeps are, in contrast, 30% to 60% shorter than the ejections, except over the flat bed, where the ejections and sweeps have similar duration.

(ii) The averaged magnitude of the ejections is comparable to that of the sweeps, at all of the positions (in relation to the bedform). The sweeps are, in contrast, more intense than the OIs and IIs. The magnitude of the sweeps is about three times that of OIs and IIs over flat bed, but the difference decreases with increasing distance from the bedform (Table 3-14).

Position	Ratios of the magnitudes of the bursting events			Ratios of the durations of the bursting events		
	E_{mag}/S_{mag}	OI_{mag}/S_{mag}	II_{freq}/S_{mag}	E_{dur}/S_{dur}	OI_{dur}/S_{dur}	II_{dur}/S_{dur}
Flat bed	1.3	0.3	0.3	1.0	0.8	0.8
X=3.3H	0.8	0.5	0.4	1.3	0.8	0.7
X=8.3H	0.9	0.6	0.5	1.6	0.8	0.9
X=16.7H	1.1	0.7	0.6	1.4	0.9	0.9

Table 3-14: The 3 columns on the left-hand side: ratios of the magnitude of the ejections, OI and II, over that of the sweeps (E_{mag}/S_{mag}, OI_{mag}/S_{mag} and II_{mag}/S_{mag} respectively). The 3 columns on the right-hand side: ratios of the duration of the ejections, OI and II, over that of the sweeps (E_{dur}/S_{dur}, OI_{dur}/S_{dur} and II_{dur}/S_{dur}, respectively)

The shorter duration and weaker magnitude of the OI and II events, in comparison with the sweeps, explain their lower capacity to move sediments, compared to that of the sweeps. However, sweeps and ejections are of similar magnitude and duration; this shows that the magnitude and duration of the bursting events do not control entirely their efficiency in moving bed material. Other possible controlling factors are summarised below:

(i) The orientation of the bursting structures in relation to the bed surface. This controls their momentum impact onto the seabed sediments: the downward flowing sweeps 'hit' directly the bed sediment grains, whereas the upward flowing ejection structures are expected to induce weaker 'disturbing' forces onto the bed sediment, in spite of similar stress magnitudes.

(ii) The macro-turbulence structures are expected to play a significant role. The influence of high-speed flow modules, in which most sweeps are embedded, on bedload transport, is investigated in the next Section.

3) Macro-turbulence influence on bedload movements.

The average percentage of bedload sediment movements occurring during macro-turbulent events of high current speed, compared to the mean (i.e. $U_{macro} > 0$), has been estimated over the flat bed and at each position downstream of the bedform (Table 3-15). Those movements occurring during low macro-turbulent current speed ($U_{macro} < 0$) are the complements to 100% of the values shown in the Table. The results indicate that the majority of bedload transport occurs during macro-turbulent structures, of high mean velocity. This result was expected, since most sweeps (which control, dominantly, the sediment movements) occur during $U_{macro} > 0$. It supports the concept, however, that the higher macro-scale flow speeds associated with sweeps (compared to those associated with ejections) favours the bed sediment disturbance initiated by the sweeps.

Position	Number of sediment movements	% of sediment movements occurring during Umacro>0
Flat bed	62	69%
X=3.3H	283	65%
X=8.3H	243	60%
X=16.7H	179	65%
All positions	767	64%

Table 3-15: Percentages of sediment movements observed during macro-turbulent structures of high mean current speed. The percentages of the first 4 lines are the averaged values for the ADV record obtained over the flat bed and at different position downstream of the bedform. The precentages in the last line is the averaged value of all of the data.

4) Concluding remarks

The efficiency of the sweeps in moving sediment is considered, on the basis of the detailed laboratory investigations, to be a combination of the following factors:

- the direct impact of the sweep flow structures onto the bed sediment (downward velocity);
- the large stress magnitude of the sweeps;
- the high turbulent and macro-turbulent streamwise flow speeds associated with the sweeps;
- the high frequency of occurrence of the sweeps.

3.3 Synthesis of the laboratory results

The laboratory experiments provided detailed measurements, under controlled and simplified conditions, of the processes observed *in situ* (see Chapter 2). Many aspects of the laboratory results are in agreement with the field observations, but differences were also apparent. The main

difference in the observations was the recovery of the logarithmic velocity profile at closer distances from the bedform in the laboratory flume than in the field. This difference was attributed to the larger scale of the velocity fluctuations generated *in situ*, downstream of the bedforms; the longer wavelength of the disturbances allows them to propagate further downstream, before being dissipated.

The main findings of the laboratory investigations are synthesised below:

- A large-scale bedform modifies the structure of the mean flow, the turbulence and the sediment transport, up to large distances (x) downstream of the bedform (of height H). The most significant differences in the BBL characteristics, compared to those of 'classic' flows are:

  (i) thicker BBL, up to $x \geq 25H$;

  (ii) larger turbulent velocity fluctuations, up to $x \geq 25H$;

  (iii) increasing turbulent velocity with height above the bed, up to $8.3H < x < 16.7H$;

  (iv) different scaling of the turbulent velocity with the mean flow, up to $x \geq 25H$;

  (v) increased contribution of OI and II to the total stress, up to $x \geq 25H$;

  (vi) longer and more intense bursting events, up to $x \geq 25H$;

  (vii) the Reynolds bed shear stress does not relate to the mean velocity shear, up to $x \geq 25H$;

  (viii) lower critical mean velocity speed for sediment movement initiation , up to $x \geq 16.7H$; and finally,

  (ix) bedload transport occurs in terms of larger groups of particles and is more intermittent, up to $x \geq 16.7H$.

  These modifications are attributed to additional turbulence generated from the free-shear layer, separating from the crest of the bedform. At this location, Kelvin-Helmotz instabilities develop along the vortex lines of the free-shear layer, which provide additional turbulent motions to the BBL from those induced by bed friction. This process disrupts the vertical organisation of the turbulent flow, and increases the amplitudes of the turbulent motions.

  The movements of sediment as large groups, downstream of the bedform, respond to the longer bursting events, in comparison to over a flat bed. The higher intermittence in the sediment movements is considered to be linked, partially, to the larger skewness of the velocity fluctuation distributions (i.e. larger intermittent positive excursions of the streamwise from the mean).

- Macro-scale turbulence structures are generated in the lee of large-scale bedforms, through bedform/flow interaction processes. These structures are attributed to the large-scale

vortical-like motions, characterising the free-shear layer.

The macro-turbulence structures modify the bursting process and the sediment transport, as follows:

(i) most sweeps and IIs occur during macro-scale modules of high-streamwise speed; sweeps and IIs are also longer and stronger during these modules - in contrast, most ejections and OIs occur during macro-scale events of low streamwise speed, where they also longer and stronger; and

(ii) some 60% to 70% of bedload movements occur during macro-scale events of high streamwise velocity

- Bedload sediment movements of the sand and gravel particles are controlled essentially by the sweeps (to ~57%), both over flat bed and downstream of the bedform. The control of bedload transport by the sweeps is attributed, mainly, to: (i) their high momentum-impact on the bed (fast downward flow); and (ii) to their high frequency of occurrence.

- Multiple Reynolds stress peaks, where two or three sweeps succeed each other, or, less frequently, where different bursting events alternate, contribute to about 15% of the observed sediment movements. 'Multiple stress peaks' cannot be explained by the traditional 'bursting' model, involving streamwise or hairpin vortices (Grass *et al.*, 1991; Smith, 1996). They can be related, however, to the dynamics of 'funnel' vortices in the near-bed layer (Kaftori *et al.*, 1994) (Section 1.2.2).

- The 4 bursting events contribute to the overall bedload transport, in the same way over a flat bed and downstream of a bedform. These results suggest that a similar flow parameter could be used to predict bedload transport in: (a) 'classic' flows; and (b) in more complex flows, associated with topographic features.

- Differences in some aspects of the turbulence are observed; these are important to take into account in the modelling of turbulence parameters. These differences include: (i) larger contributions of the negative stress events to the Reynolds stress, which lower its value; (ii) a Reynolds stress which is not related directly to the mean horizontal velocity shear; and (iii) different scaling of the turbulent velocities and of the Reynolds stress, with the mean flow velocity than that typical of 'classic' flows.

- Other aspects of turbulence are little affected by the bedform, except very close to its lee-side *i.e.* (i) similar scaling of the turbulent velocities with the Reynolds stress; and (ii) similar scaling of the Reynolds stress with total turbulent kinetic energy. Hence, the '0.19' values used in the TKE method to estimate bed shear stress $(\tau = 0.5\rho TKE)$is found to be a reasonable mean value, for the streamwise profile across the bedform.

Chapter 4

Discussion

4.1 Comparison between the field and laboratory study conditions

The measurement methods and the prevailing environmental conditions during the field and laboratory experiments are compared here before synthesising the results. The common aspects and the characteristics specific to each study, are summarised in Table 4-1.

Both the field and laboratory experiments investigate the effects of bed/flow interaction downstream of large-scale singular bedforms, in shallow BBLs. The measurement heights at the field site were between z = 0.03d and z = 0.09d above the bed; this corresponds approximately to the near-bed layer in the laboratory investigations ($0.03 \leq z \leq 0.10d$). The mean flow (free from the bedform influence) is steady and unidirectional in both environments. Small wind-induced gravity waves were present at the field site, but their influence on the turbulence structure has been shown to be negligible. Flow separation above the bedform crest occurred in both of the investigations. The (bed) area just beneath the velocity measurements and at the level of the sediment transport observations was flat in both environments. If ripples were present at the field site, these are smaller than 15 cm in wave-length (side-scan sonar resolution); such bedforms, if present, would not generate the particular characteristics in the turbulence and sediment transport observed at the site.

The characteristics specific to the field and to the laboratory experiments are outlined below.

(i) The complexity of the topography.

The topography around the field experimental site was more complex than in the laboratory flume, where only one bedform was present. The presence of various bedforms around the *in situ* experimental site does not allow the determination of the exact distance of the bedforms, influencing the measurements. However, the nature of the bedform/flow interaction processes is similar to those in the laboratory *i.e.* large-scale bedforms (compared to the water depth), 'singular' bedforms, and flow separation conditions.

(ii) The nature of the sediment transport observations.

The field experiments concentrated on the study of suspended sediment transport, whereas the laboratory experiments investigated the bedload and re-suspension processes.

(iii) The sampling frequency.

The sampling frequency in the field experiments (Fs = 5 Hz) is 5 times lower than the one used in the laboratory experiments (Fs = 25 Hz). Although both of the sampling frequencies extend to within the turbulence scales (whose lower limit is about 1 Hz), the field data do not incorporate

the contributions of the smallest motions (*i.e.* those which are associated with a frequency $F > F_N$ = 2.5 Hz). Soulsby (1980) estimated spectral losses, resulting from sampling frequency limitations, in turbulent velocity measurements collected in conditions similar to the field experiment described here. Soulsby (*op. cit.*)'s experiments where characterised by: sampling frequency of 5 Hz; tidal BBL 14 m deep; mean current speed of up to 0.60 m/s; current velocity measurements using electromagnetic current meters, positioned at z = 0.30 and 1.40 m above the bed. The high-frequency contribution losses to the velocity variances were estimated to be less than 1% at both heights. Differences in the turbulent quantity estimations due to the smaller sampling frequency in the field experiments (than in the laboratory) can be considered, therefore, to be negligible.

Similarities/Differences		
	Field experiment	Laboratory experiment
Near-bed measurements	• $0.03 \leq z/d \leq 0.09$ • Fs = 5 Hz	• $0.03\text{-}0.05 \leq z/d \leq 0.10$ • Fs = 25 Hz
Flow	• Unidirectional current • Steady flow speed	• Unidirectional current • Steady flow speed
Bedform	• Various scales of bedforms • H = 1.5 – 20 m • $0.2 \leq H/d < 1$	• One bedform • H = 0.06 m • H/d = 0.2 & 0.3
Mean flow scale	• d = 13 m • flow width = 'infinite' • $U_\infty \cong 0.5 - 1.0$ m/s	• d = 0.20 & 0.30 m • flow width = 0.30 m • $U_\infty \cong 0.15 - 0.35$ m/s
Turbulence scale	• $T_{\text{bursting event}} = 2 - 5$ s	• $T_{\text{bursting event}} = 0.1 - 0.6$ s

Table 4-1 : Characteristics of the experimental conditions in the field and laboratory environments. Legend: H = bedform height; d = water depth; U_∞ = mean free-stream flow speed; $T_{\text{bursting event}}$ = mean period of the bursting events.

(iv) The scales of the mean and turbulent flows.

In the field BBL, the water depth, the flow width, the BBL thickness, the mean flow magnitude and the turbulence structure scales, are much larger at the field site than the in laboratory flume (Table 4.1). For example, the bursting event duration is an order of magnitude lower in the laboratory flume than at the field site. The difference in the mean and turbulent flow scales in both environments provide an interesting comparison for the investigation; it permits the

exploration of the 'universal' characteristics of the turbulence (such as the ratios between turbulent velocity fluctuations and mean velocity or friction velocity) within the context of two different scales. The 'scale' difference may be more problematic for the study of the response of sediment grains to the flow structures. It is possible, for example, that the turbulence scales, which are an order of magnitude smaller in the laboratory flume than in the field, are associated with different onset or rate of movements of a particular size of particles, in the laboratory and in the field. The results concerning the nature of the turbulence structures involved in the different type of sediment transport processes, as analysed in this work, are expected to be independent of the scale of the flow. Comparison between the field and laboratory results (described later) shows that the control of the characteristics of the turbulence by the mean flow or by the macro-turbulence, is mostly unaffected by the scale difference in the environments.

4.1.1 Concluding remarks

Although the laboratory and field investigations present some differences (such as the topography, the scale of the flow or the measurement sampling frequency), the results are comparable and complementary. The field experiments provide information on processes occurring in natural BBLs, while the laboratory experiments provide more extensive measurements, collected under controlled conditions. The laboratory measurements have extended, sometimes repeated (confirming or disagreeing with), the findings observed initially *in situ*.

4.2 Characteristics and spatial extent of flow/bedform interactions

Upstream of the bedform, the mean and turbulent flows are affected only moderately by the bedform. Just upstream of the stoss-side of the bedform, the logarithmic trend in the vertical profile of mean horizontal velocity is improved compared to flat bed conditions. The BBL is about 40% thicker and the turbulent velocity fluctuations are about 20% higher. Larger disturbances occur downstream of the bedform. From the lee of the bedform, up to the flow re-attachment point ($x \sim 8.3H$) *i.e.* the re-circulation region, the flow is detached from the bottom wall and forms a wake, with a bottom layer flowing upstream. Within the re-circulation region, the turbulent velocity magnitudes are double those associated with flat bed conditions, but the turbulence is dominated by non-three-dimensional coherent motions (small $r_{u'w'}$ values). Up to $8.3H \leq x < 16.7H$ downstream of a bedform, the turbulent velocity magnitudes increase vertically with distance from the bed, up to a height corresponding approximately to the bedform height. This increase is attributed to the effect of the free-shear layer propagating downstream from the

bedform crest, where the flow separates. In the far wake region, the flow reorganises itself progressively with increasing distance from the bedform, towards 'classic' flows characteristics. The bedform/flow interaction effects are observed, however, up to large distances downstream (x > 25H). The main differences in the flow structures of the far wake region, compared to 'classic' flows, consist of: (i) a thicker BBL than over flat bed and departure from the logarithmic profile; (ii) the presence of macro-turbulence structures; (iii) the structure of the Reynolds stress; and (iv) increased and 'patchy' suspended sediment transport and bedload sediment movements. These points are discussed in the next Sections. The vertical velocity profile departs from the logarithmic trend at larger distances downstream of the bedform *in situ* than in the laboratory. This difference is believed to result from the larger scale of the 'wave-disturbance train' in the field (see below) (against similar viscous dissipative forces), whose longer wavelength and larger energy allow them to propagate farther downstream from the flow separation zone.

4.3 Control of sediment transport by bursting events

4.3.1 Maintenance of suspended sediment into suspension by ejections

Cross-correlation analysis of velocity and SSC indicate that ejections induce increases in the suspended sediment concentration. Two aspects of ejections are favourable to suspended sediment transport: (i) they are associated with upward flows which provide uplifting forces to raise particles into the water column against the gravity force. The upward transport of sediment into the water column and/or the maintenance of material into suspension was shown to be related to the positively skewed turbulent vertical velocity distributions i.e. dominant upward turbulent flow, characterising the bottom layer (Leeder (1983); Wei and Willmarth (1991)); and (ii) ejections propagate high into the water column with little dissipation and, hence, they can transport sediment from the lower more turbid waters into higher layers. Transport of sediment into suspension, downstream of bedforms, is also favoured by the larger turbulent velocity fluctuations in general; these enhance the vertical mixing.

4.3.2 Initiation of bedload movement by sweeps

Sweeps generate most of the bedload movements (~57%) over a flat bed and downstream of a bedform. This percentage is in close agreement with the estimation of McLean *et al.* (1996), who estimated that 54% of the sediment flux over 2-D dunes was generated during sweep events. These observations agree also with previous results obtained over flat bed (*e.g.* Grass, 1971; Yung *et al.*, 1989; Drake *et al.*, 1988; Thorne *et al.*, 1989). In contrast, Sechet and Le Guennec (1999)

indicated the primary role of ejections in the control of medium-sized sand movement over smooth beds. The method used in their study is, however, somewhat controversial. Firstly, they detected only ejection events in the velocity records (using the VITA method), whereas sweeps were detected indirectly, assuming that they occur after the last ejection event of a burst. This assumption has not been proven and is invalid in the funnel-vortex model, where bursting events can appear in any order. Secondly, the association of bedload movements with ejections was based on statistical comparisons between the time-scale of ejections and that of bedload movements. Hence, no direct correlation was made between the occurrence of bedload movements and the characteristics of the velocity signals. The role of ejections in bedload transport, as suggested by these investigations, is, however, interesting to be considered in more detail. Sweep structures provide a much stronger tractive (tangential) force on the sediment grains (due to $u' > 0$), than ejections ($u' < 0$). This characteristic could explain their higher efficiency in moving sediment particles along the bed. However, ejections display much larger uplifting forces ($w' > 0$), than sweeps ($w' < 0$); this can favour bedload movements by counteracting the gravity force, which induces bed friction and inhibits the sliding of particles along the bed.

The percentage of bedload sand movements attributed to each bursting event are similar over flat bed and at the different positions downstream of the bedform. This similarity indicates that the bursting mechanisms generating bedload movements are similar in uniform flows over flat beds and in non-uniform flows downstream of large-scale bedforms. This conclusion suggests that similar flow parameters can be used to predict bedload transport over flat bed and downstream of topographic features; this would simplify greatly the modelling of sediment transport, in areas of variable topography.

4.3.3 Entrainment of bed sediment into suspension: uncertainties about the processes

Control of re-suspension of bed particles by sweeps, downstream of large-scale bedforms, is indicated in the laboratory results. Only limited data has been published on this particular subject, but most authors have suggested the control of re-suspension processes by ejections. However, some experimental work has been undertaken on almost neutrally buoyant particles (*e.g.* Sumer and Deigaard, 1981; Yung *et al.*, 1988), which are expected to have a different control for their resuspension, than (heavier) sand particles. The lighter particles are more likely to follow the pattern of fluid motions, such as the upward flow of ejections, even under low flow momentum conditions. Heavier (natural bed) particles, in contrast, require strong fluid momentum impact to be mobilised and placed into suspension. Although ejections are associated with slightly longer period and higher Reynolds stress magnitude than sweep events (Tables 3.4 and 3.5), the movement of ejection structures is directed upwards. This generates a smaller fluid-

transmitted force to the bed sediment, than that induced by sweeps, which impact directly onto the bed. Garcia *et al.* (1996) used natural sand particles and found also that ejections re-suspend bed sediment. In these experiments, however, only ejections were visualised (and not the other bursting events), so conclusions cannot be drawn concerning the relative efficiency of the 4 bursting events. Another possible explanation for the difference between the results obtained here and those of previous investigations can be proposed: in the present experiments, only the initial velocity signal associated with each sediment movement was recorded (*i.e.* the signal recorded at the start of the movement and above the origin point of the movement). It is possible that once a sweep has mobilised and lifted up the sediment grains slightly, the grains are entrained farther up into the water column by an ejection event; this would occur slightly later and farther downstream of the recording point. This phenomenon could explain the observation that some sweeps events generate re-suspension events, whereas others, with a similar stress-magnitude, generate only bedload movements.

4.3.4 The role of OI and II events in sediment transport

The laboratory results suggest that OI and II events play a negligible role in the transport of sand and gravel as bedload. This observation is in agreement with most of the previous findings over a flat bed. However, the role of these events on sediment transport cannot be disregarded, particularly downstream of large-scale bedforms, where their frequencies of occurrence and intensities are large. Past measurements have suggested their importance on both re-suspension and bedload movements, over a flat bed and over bedforms (Thorne *et al.*, 1989; Bennett and Best, 1995; McLean et al., 1996). Thorne *et al.* (1989) considered that the smaller contribution of OIs to gravel movements compared to that of sweeps, is due their smaller frequency of occurrence. These authors have suggested that it is the tangential force (*i.e.* the sign and magnitude of u'), not the vertical force, which controls the movement of gravel on the bed.

4.3.5 Multiple Reynolds stress peaks

A significant fraction of sediment movements have been found to be associated with successive $u'w'$ peaks *i.e.* with 2 or 3 successive sweep events, or, in a smaller proportion, with a succession of some of the 4 bursting events in a variable order. This observation disagrees with the traditional bursting cycle model in which, typically, 1 sweep follows (1 or more) ejection events event (Nakagawa and Nezu, 1983; Smith *et al.*, 1991). These measurements support the hypothesis that the near-bed layer is occupied by 'funnel' vortices (Figure 1.3(b)). Multiple $u'w'$ peaks in turbulent velocity signals were recorded elsewhere by Kaftori *et al.* (1994) and Sechet (1996). Kaftori *et al.* (op. cit.) suggested that multiple $u'w'$ peaks can be explained by the

motion of funnel-shape vortices near the bed. A funnel-vortex consists in an expanding oblique spiral, with its narrow opening-end positioned upstream and close to the wall, and its wide opening-end pointing downstream and away from the wall. The flow inside the vortex alternates between the low-speed region near the wall and the high-speed region away from the wall; this generates large vertical and horizontal rms velocities which are, respectively, about 25% and 40% higher than those of the surrounding flow. The motion of the flow along the 'spiral' funnel-vortex can appear, for a stationary observer, as one of the four bursting events. Observation of the ascending part of the vortex spiral, appears as an ejection event; conversely, the downward motion of the vortex can be perceived as a sweep event (Kaftori *et al.*, 1994).

4.4 Macro-turbulence structures and their role in the bursting process and sediment transport

Macro-turbulence structures are observed to be generated in the BBL flow downstream of large-scale bedforms. For the first time, the influence of such macro-turbulence, on the bursting process and on the sediment transport, have been shown, both *in situ* and in a laboratory flume.

The macro-turbulence structures manifest themselves as large-scale current speed and suspended sediment concentration (SSC) oscillations within the BBL. Several observations show that the large-scale flow oscillations result from bedform/flow interaction processes. These observations are outlined below:

In the laboratory investigation:

(i) the large-scale velocity oscillations disappear after removal of the bedform from the flume;

(ii) the frequencies of the large-scale velocity oscillations are similar to the shedding frequency of vortices downstream a sphere (Abarbanel et al., 1991); and

(iii) the break in the vertical variation of turbulent parameters downstream of the bedform at $z \sim H$, indicates the presence of a free-shear layer, propagating from the bedform crest separation point.

In the in situ experiment:

(i) sea surface signatures on SAR images revealing strong bedform/flow interactions; and

(ii) the energy in the macro-turbulence structures increases, with increasing mean tidal current speed.

The macro-scale structures are considered to consist of large-scale eddies (large-scale vortical motions), formed in the lee of upstream bedforms, and advected downstream by the mean flow (Figure 4.1(a)). Along the vortex lines of these flow structures, turbulent instabilities develop, which transport low-horizontal speed fluid upwards. At the same time, 'scour loops' (Figure 4.1(b)) are created, which transport high-horizontal speed fluid downwards.

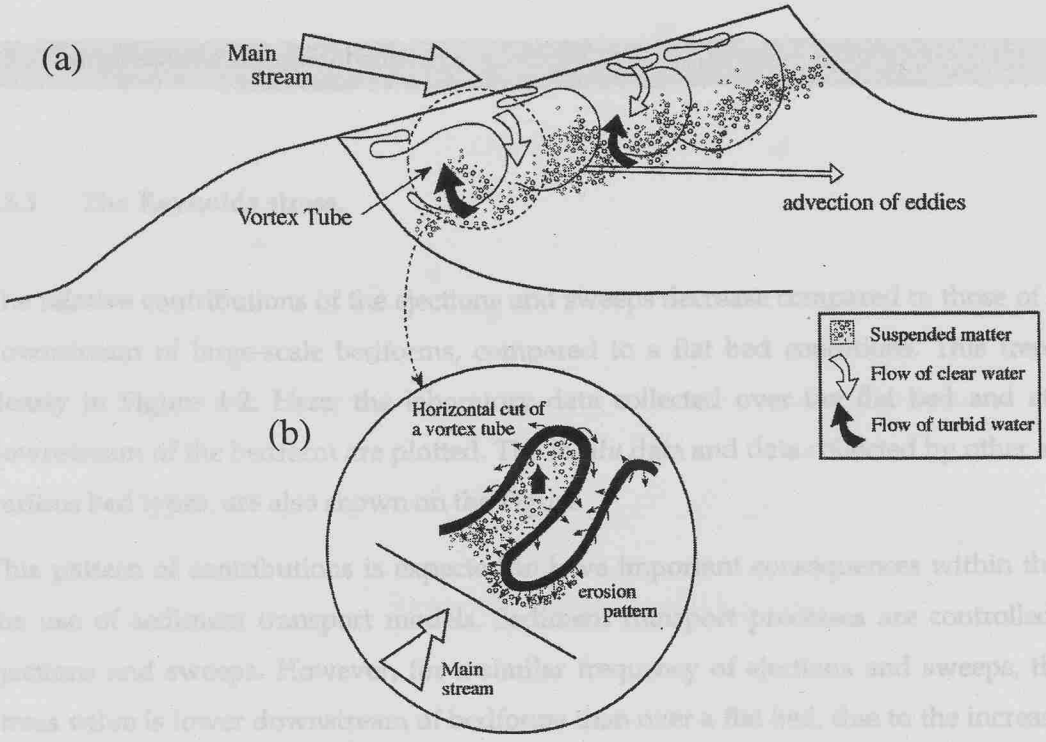

Figure 4-1: (a) Vortical structures generated in the lee region of a large bedform by a tidal flow flowing over it. (b) Horizontal section of the vortex tube, showing the development of turbulent coherent structures, carrying turbid water upward and clear water downward (after Muller and Gyr, 1996).

These processes modify the structure of the Reynolds stress, inducing uneven temporal and spatial distribution (*i.e.* 'patchiness') of the bursting events, of the bedload movements and of the suspended sediment concentration. Patches of high suspended sediment concentration result from high-frequencies of strong and long ejection events within macro-scale modules of low streamwise speed ($U_{macro} < 0$). This process can explain the generation of the surface 'boils', observed in rivers or marine shallow BBL flows, over a bed characterised by large-scale bedforms (Jackson, 1976; Bennett and Best, 1995; Kostaschuk, 2000).

In contrast with the ejections, the sweeps are more frequent and are larger in magnitude and duration, during macro-scale modules of high-streamwise-speed flow structures ($U_{macro} > 0$). These characteristics are associated with larger bedload movements and a more intermittent bedload transport, downstream of bedforms, compared to over flat bed.

Intensification of sweep and OI events, both having $u' > 0$, during $U_{macro} > 0$, is explained by: (i) the additional flow momentum associated with the long-scale streamwise flow acceleration associated with the $U_{macro} > 0$. These large-scale accelerations are believed to trigger turbulent small-scale flow accelerations; and (ii) the 'inhibition' of ejections and IIs, both associated with $u' < 0$, during $U_{macro} > 0$. Intensification of ejections and IIs during periods of large-scale deceleration of the mean flow ($U_{macro} < 0$) is explained by a similar 'large-scale to small-scale cascade' process.

4.5 Implications for modelling

4.5.1 The Reynolds stress.

The relative contributions of the ejections and sweeps decrease compared to those of OIs and IIs, downstream of large-scale bedforms, compared to a flat bed conditions. This trend is shown clearly in Figure 4-2. Here, the laboratory data collected over the flat bed and at x = 16.7H downstream of the bedform are plotted. The *in situ* data and data collected by other authors over various bed types, are also shown on the Figure.

This pattern of contributions is expected to have important consequences within the context of the use of sediment transport models. Sediment transport processes are controlled mainly by ejections and sweeps. However, for a similar frequency of ejections and sweeps, the Reynolds stress value is lower downstream of bedforms than over a flat bed, due to the increased negative stress event participation. It is expected, therefore, that the Reynolds stress will not be related to sediment transport quantities, in the same way downstream of large-scale bedforms than over flat bed.

Downstream of a large-scale obstacle, the bottom Reynolds stress τ_0 is not related to the local mean velocity gradient, as it is in 'classic' flows. This lack of a relationship is due to: (i) differences in the structure of the Reynolds stress (discussed above); and (ii) the fact that the turbulence and the Reynolds stress is not generated only from the shearing of the mean flow, induced by bottom friction effects. Downstream of large-scale bedforms, where flow separation occurs, turbulence is produced also through Kelvin-Helmhotz instabilities, developing along the vortex lines of the free-shear layer propagating from the crest (Holt, 1995).

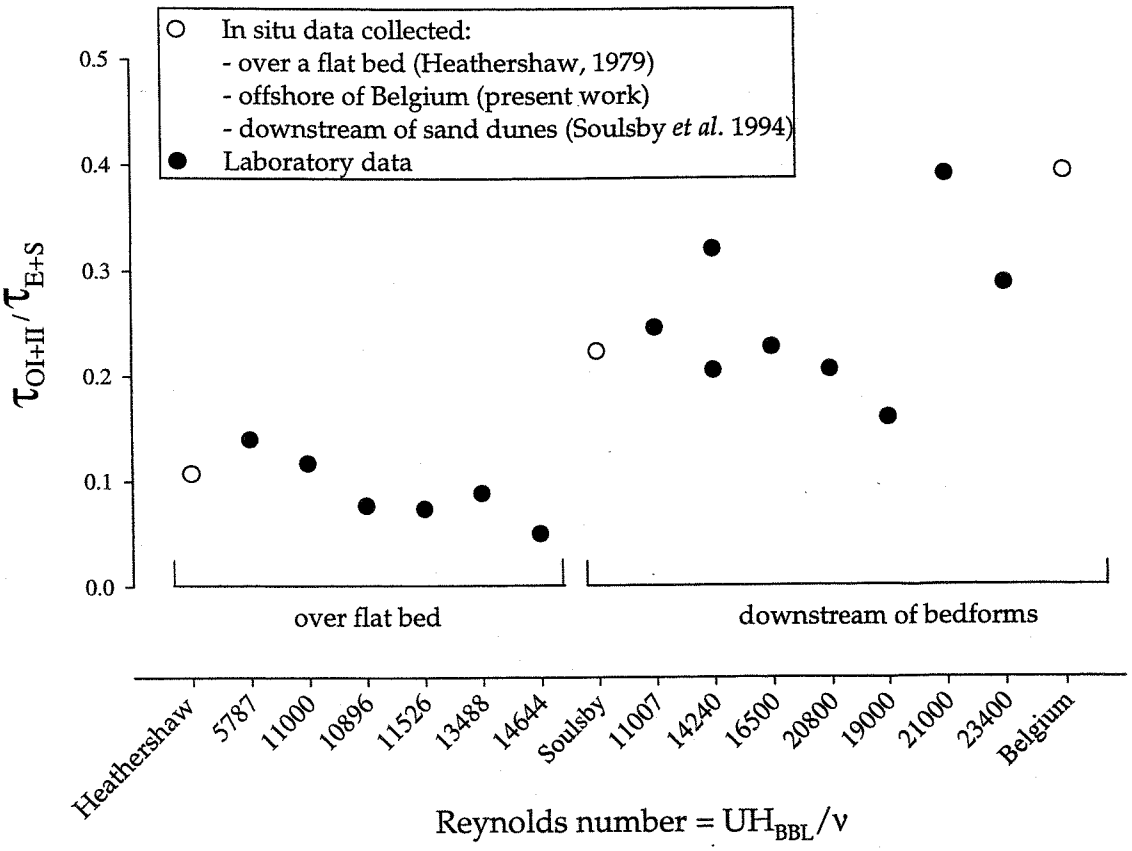

Figure 4-2: Ratios of (OI + II) contributions to the Reynolds stress τ, over (Ejections + Sweeps) contributions to τ, measured over different seabed types. The plot include: (i) the laboratory data collected over a flat bed and at x = 16.7H downstream of the bedform, indicated by their Reynolds numbers; (ii) the *in situ* data, indicated as 'Belgium'; (iii) data collected by Heathershaw and Thorne (1985) over a flat bed; (iv) and data collected by Soulsby *et al.* (1994), over sand dunes.

τ_0 is related to the total turbulent kinetic energy level, in approximately the same way downstream of bedforms than over flat bed. Similar $-\overline{u'w'}/\overline{q^2}$ ratios (~0.12) were measured, in the laboratory: over a flat bed; in the re-circulation region (except at x = 0H); and near the re-attachment point. Slightly lower ratios characterise the far wake region, in the laboratory ($-\overline{u'w'}/\overline{q^2}$ ~ [0.07 0.08]) and in the field ($-\overline{u'w'}/\overline{q^2}$ ~ 0.05). This decrease cannot be explained at this present time.

4.5.2 Turbulence parameters

The flow parameter ratios studied and the characteristics of the bursting events, depend (sometimes) on distance from the bedform; they vary little with mean flow velocity, at each of the

measurement locations. This observation suggests that fully turbulent flows, downstream of large-scale bedforms, display a particular turbulent structure and scaling with the mean flow; this depends weakly upon the mean flow regime. This resembles the display of 'universal' turbulent characteristics of high Reynolds number flows over a flat bed.

The scaling of the turbulent velocities and of the total turbulent kinetic energy, with the Reynolds stress, are similar at most distances from the bedform (except close to the lee-side), to those measured in classic flows (see Section 1.3.3). This result is important, since it validates modelling of turbulence motions using the Reynolds stress parameters; this forms the basis on which most present hydrodynamic models are developed.

The large differences in the ratios of the turbulent velocities, with the mean streamwise speed at each position upstream and downstream the bedform ($x \leq 21H$), show that the mean flow cannot be used to estimate the turbulent velocities close to bedforms.

In the far wake region (at distances greater than 21H downstream of the bedform in the laboratory and at the *in situ* sites), most turbulent parameters have recovered, or maintained, their classic flow values. This is the case for the turbulent velocities to the mean flow speed ratios, the turbulent velocities to the Reynolds stress ratios and the turbulent energy dissipation rate.

It is important to note that these turbulence quantities are estimated by 'bulk' methods, which imply a certain degree of spatial averaging. It is, therefore, the spatial average of these quantities which appear to remain unchanged compared to those values found in 'classic' uniform flows.

4.5.3 Sediment transport prediction

- Sweeps control bedload movement over a flat bed and downstream of a bedform.
- The four bursting events participate in sediment transport processes the same way downstream of the bedform as over a flat bed.

The above observations suggest that bedload sediment transport is related to the contribution of the sweeps in the same way downstream of the bedform as over flat bed.

However:

- sweeps are longer downstream of a bedform; and
- sweeps move sediment grains as larger groups downstream of a bedform, than over a flat bed.

Therefore, bedload transport is not expected to be related only to the mean magnitude of the sweep-induced stress, but to a 'weighted-stress' value including the bursting event duration.

Further,

- the frequency of occurrence of OI and II events increases compared to that of ejections and sweeps, downstream of a bedform; and
- the increased (negative) participation in OIs and IIs to the Reynolds stress reduces the Reynolds stress values downstream of a bedform. Hence, lower Reynolds stress values are measured downstream of a bedform than over flat bed, for similar contributions of sweeps.

Thus, the Reynolds stress is not considered, for the above reasons, an appropriate quantity to be used in the prediction of sediment transport, in complex topography environments.

Conclusion and future work

4.1 Conclusion

Sweeps and ejections have been shown to be the dominant factors controlling sediment transport, over a flat bed and downstream of bedforms. Sweeps were associated with most of the bedload resuspension events of the sediments, whereas ejections appeared to control the upward diffusion of material through the water column. The two other bursting events i.e. the outward and the inward interaction events (OIs and IIs), had little effect on the sediment transport. This observation is not in agreement with the suggestions of Bennett and Best (1995), who proposed that the increased contributions of OIs downstream of bedforms, compared to that over a flat bed, may explain the erosion occurring in the trough and lower back of dunes. Such erosion may, instead, be the result of the larger contributions of both the sweeps and ejections in these areas.

A significant fraction of the observed bedload movements (~14%) was associated with multiple bursting events, consisting generally of two or three successive sweeps or alternating bursting events, in variable sequence. Such events cannot be explained by the traditional models of the bursting process. In such models, the bursting events are generated by the flow dynamics of quasi-streamwise vortex, where each bursting event triggers a different and a particular bursting event. The observations of multiple stress events support the hypothesis that the near-bed layer is characterised by the presence of funnel vortices, as suggested by Kaftori *et al.* (1994) .

The flow downstream of the large-scale bedforms (characterised by a bedform height to water depth ratio > 0.2) was characterised by large oscillations in the mean flow speed (with the length-scales of the oscillations of the order of the water depth). The presence of high-turbidity large-scale modules, appearing sometimes as surface 'boils', has been observed many times in flows over dunes, in rivers and in shallow marine BBLs. The present study has, for the first time, investigated in detail the effects of macro-turbulence structures on the bursting process. This study provided an explanation for their effect on the sediment transport patterns observed in flows over bedforms. It was shown that the concentration and amplification of ejection events, within macro-turbulence modules of low streamwise velocity, increase the sediment concentration within the modules. This process can explain the high turbidity of the surface 'boils' which can be observed in areas of large-scale bedforms. In contrast, the macro-scale flow modules of high streamwise speed are associated with a higher frequency of sweeps, which also have a larger amplitude and duration within these modules; this pattern can explain how the bedload movements occur as larger groups and in a more intermittent fashion than over a flat bed.

The structure of the Reynolds stress, the parameter used in models to predict sediment transport, was modified downstream of a bedform. As the current flowed over a bedform, the four bursting

events increased in magnitude and duration and the Reynolds stress value increased. This followed the general increase in the turbulence level and in the sediment transport rate. The negative contributions of the OIs and IIs increased more than the positive contributions of the ejections and sweeps. This resulted in lower Reynolds stress values than those which are associated, over a flat bed, with similar contributions of ejections and sweeps. These results indicate that the Reynolds stress is likely to underestimate the onset of sediment movement and the quantity of sediment transport downstream of bedforms.

Other aspects of the turbulence were, in contrast, little affected by the proximity of large-scale bedforms. Hence, the ratio of the turbulent kinetic energy to the Reynolds stress was similar throughout the streamwise profile across the bedform (except close to the lee-side); this suggests validity of applying the scaling of the turbulence parameters by the Reynolds stress used in 'classic' flow models, to flows over complex topography. In the far wake region at the field site, parameters such as the turbulent energy dissipation rate and the turbulent kinetic energy were similar to those observed in uniform shallow BBL flows over flat bed ('classic' flows). These similarities, measured in a flow characterised by large-scale flow oscillations and non-logarithmic vertical velocity profiles, indicate that the small-scale turbulence is de-coupled from the large-scale motions in this region, as in 'classic' flows.

4.2 Future work

Firstly, it would be of interest to investigate quantitatively whether the Reynolds stress values can be corrected by a simple factor, to compensate for the decrease due to the increase in the OIs and IIs contributions downstream of bedforms. Such a correction, if possible, should be applied to the Reynolds stress values measured downstream of bedforms. In this way, a similar Reynolds stress value would be associated with the onset of movement and rate of transport of a particular sediment, over a flat bed and downstream of a bedform. Hence, similar relationships could be used to predict sediment transport such parts of a bed. The measurements to undertake to achieve this task could involve:

(a) the comparison of the critical Reynolds stress values for the initiation of movement of different sediments, over a flat bed and downstream of large-scale bedforms; and

(b) the comparison of the Reynolds stress values generating a similar rate of transport of a given sediment, over a flat bed and downstream of large-scale bedforms.

Secondly, more work is needed to determine the detailed mechanisms involved in the re-suspension of bed material and its diffusion into the water column. Such investigation is needed for flat bed conditions as well as for beds characterised by bedforms. The laboratory

measurements undertaken in this investigation, over a flat bed and downstream of bedforms, suggest that sweeps are the first bursting event to initiate re-suspension events. It was also suggested, however, that ejections may be required to occur soon after and slightly downstream (*i.e.* at the new position of the sweep-lifted sediment particle) to transport material higher into the water column. This mechanism could explain the discrepancies between the observations made in the present work and suggestions of past authors who attributed the dominant control of re-suspension events to ejections. The investigation of this aspect could be achieved by positionning several high-frequency current sensors (two- or three-dimensional), closely spaced (i.e. by ~ 1 cm), along a streamwise line.

Thirdly, the effects of movable bedforms on the turbulence and on the associated sediment transport needs to be determined. For practical reasons, the laboratory investigation was conducted using a fixed artificial bedform. The following aspects are important to investigate:

(a) the process of erosion over a bedform (on the stoss-side, on the crest and on the trough); and

(b) the effects of the loss of flow energy, as the flow erodes the bedform, on the turbulence structures and associated sediment transport.

Finally, it would be interesting to observe how the different turbulence quantities are controlled by the small-scale coherent structure in the flows. Variation in the turbulence properties within the coherent flow structures is expected to affect significantly the turbulent mixing and transport processes (essentially re-suspension and vertical mixing). No studies have yet examined this aspect of flow dynamics, due mainly to technical limitations. For example, the investigation of the variation in the energy dissipation rate, during the sweep or ejection events of the bursting cycle, if possible, would require very high-resolution friction probes (small measurement volume (~ 1 mm) and a high sampling frequency (~ 20 Hz)).

References

Abarbanel S.S., W.S Don. D. Gottlieb, D.H. Rudy and J.C. Townsend (1991) Secondary frequencies in the wake of a circular cylinder with vortex shedding, Journal of Fluid Mechanics, 225, 557-575.

Adams C.E., J. Georges, and L. Weatherly, 1981. Some effects of suspended sediment stratification on an oceanic Bottom Boundary Layer. *Journal of Geophysical Research*, 86, 4161-4172.

Adams C.E., J.J. Wells and Y. Park (1990) Internal hydraulics of a sediment-stratified channel flow. *Marine Geology*, 95, p. 131-145.

Baetke F., H. Werner and H. Wengle (1990) Numerical simulation of turbulent flow over surface-mounted obstacles with sharp edges and corners. *Journal of Wind Engineering and Industrial Aerodynamics*, 35, 129-147.

Bagnold, R.A. (1966) An approach to the sediment transport problem form. *General Physics Geological Survey Prof. Paper 422-I*, Washington.

Bendat J.S. and A.G. Piersol (1971) *Random Data: Analysis and Measurement Procedures*, Wiley Interscience, New York, 407 pp.

Bennett S.J. and J.L. Best, 1995, Mean flow and turbulent structure over fixed, two-dimensional dunes: implications for sediment transport and bedform stability. *Sedimentology*, 42, 491-513.

Bennett S.J. and J.L. Best (1993) Structure of turbulence over two-dimensional dunes. In M. Belorgey, R.D. Rajaona and J.F. Sleath (editors), *Sediment Transport Mechanisms in Coastal Environments and Rivers*, Euromech 310, 13-17 Sept 93.

Bernard P.S., J.M. Thomas and R.A. Handler (1993) Vortex dynamics and the production of Reynolds stress. *Journal of Fluid Mechanics*, 253, 385-419.

Best J. (1992) On the entrainment of sediment and initiation of bed defects: insights from recent developments within turbulent boundary layer research. *Sedimentology*, 39, 791-811.

Blackadar A.K. and H. Tennekes (1968) Asymptotic similarity in neutral, barotropic atmospheric boundary layers. *Journal of Atmospheric Sciences*, 25, 1015-1020.

Blackwelder R.F. (1983) Analogies between transitional and turbulent boundary layers, *Physics of Fluids*, 26, 2807-2815.

Blackwelder R.F. and H. Eckelmann (1979) Streamwise vortices associated with bursting phenomena. *Journal of Fluid Mechanics*, 94, 577-594.

Bowden K,F. (1962) Measurements of turbulence near the sea bed in a tidal current. *Journal of Geophysical Research*, 67, 8, 3181-3186.

Bowden K.F. and L.A. Fairbairn (1952) A determination of the frictional forces in a tidal current. *Proceedings of the Royal Society of London*, A214, 371-393.

Bowden K.F. and M.R. Howe (1963) Observations of turbulence in a tidal current. *Journal of Fluid Mechanics*, 17, 271-284.

Bradshaw P. and F.V.F. Wong (1972) The reattachment and relaxation of a turbulent shear layer. *Journal of Fluid Mechanics*, 72, 113-135.

Brooke J.W. and T.J. Hanratti (1993) Origin of turbulence-producing eddies in a channel flow. *Physics of Fluids*, A5, 1011-1022.

Castro I.P. (1987) A note on the lee wave structures in a stratified flow over three-dimensional obstacles. *Tellus*, 39A, 72-81

Chriss T.M. and D.R. Cadwell (1984) Universal similarity and the thickness of the viscous sublayer at the ocean floor. *Journal of Geophysical Research*, 89, 6403-6414.

Celik I. And W. Rodi (1988) Modelling suspended sediment transport in nonequilibrium situations. *Journal of Hydraulic Engineering*, 114(10), 1157-1191.

Corrsin S. (1958) On local isotropy in turbulent shear flow. *NACA R & M* 58B11.

De Souza, V.D. Nguyen and S. Tavoularis (1995) The structure of highly sheared turbulence. *Journal of Fluid Mechanics*, 303, 155-167.

Dewey R.K., P.H. Leblond and W.R. Crawford (1988) The turbulent boundary layer and its influence on local dynamics over the continental shelf. *Dynamics of Atmospheres and Oceans*, 12, 143-172.

Drake T., R.L. Shreve, W.E. Dietrich, P.J. Whiting and L.B. Leopold (1988) Bedload transport of fine gravel observed by motion-picture photography. *Journal of Fluid Mechanics*, 192, 193-217.

Earle M.D. and J.M. Bishop (1984) *A Practical Guide to Wave Measurement and Analysis*, ENDECO INC, USA, 78pp.

Elder S.A. and J. Williams (1996) *Fluid Physics for Oceanographers and Physicists*, 2nd edition, Butterworth Heinemann, 395pp.

García N., Y. Niño and F. López (1996) Laboratory observations of particle entrainment into suspension by turbulent bursting. In *Coherent Flow Structures in Open Channels*, Chicheser : John Willey and Sons Ltd, Chichester, 63-86.

Gordon C.M. and J. Witting (1977) Turbulent structure in a benthic boundary layer. In J.C.J. Nihoul (editor) *Bottom Turbulence*, Elsevier, 59-81.

Grant W.D. and O.S. Madsen (1986) The continental-shelf bottom boundary layer. *Annual Review of Fluid Mechanics*, 18, 265-305.

Grant W. D., A.J. Williams and S.M. Glenn (1984) Bottom Stresses Estimates and their prediction on the Northern California Continental Shelf during CODE-1: the importance of wave-current interaction. *Journal of Physical Research*, 14, 506-527.

Grant W.D., R.W. Stewart and A. Moillet (1962) Turbulence spectra from a tidal channel. *Journal of Fluid Mechanics*, 12, 241-263.

Grass A.J. (1971) Structural features of turbulent flow over smooth and rough boundaries. *Journal of Fluid Meachanics*, 50, 233-255.

Grass A.J., R.J. Stuart and M. Mansour-Tehrani (1991) Vortical structures and coherent motion in turbulent flow over smooth and rough boundaries, *Philosophical Transactions of the Royal Society*, London, A336, 35-65.

Green M.O., J.M. Rees and N.D. Pearson (1990) Evidence for the influence of wave-current interaction in a tidal boundary layer. *Journal of Geophysical Research*, 95(C6), 9629-9644.

Grochowski N.T.L. (1995) *(Re)suspension of fine-grained sediments by currents and waves*. MPhil-PhD Upgrade Report, Department of Oceanography, University of Southampton, 28pp.

Gross T.F. and A.R.M. Nowell (1983) Mean flow and turbulence scaling in a tidal boundary layer. *Continental Shelf Research*, 2, 109-126.

Gross T.F. and A.R.M. Nowell (1985) Spectral scaling in a tidal boundary layer. *Journal of Physical Oceanography*, 15, 496-508.

Haidari A.H. and C.R. Smith (1994) The generation and regeneration of single hairpin vortices. *Journal of Fluid Mechanics*, 277, 135-162.

Heathershaw A.D. (1979) The turbulent structure of the bottom boundary layer in a tidal current. *Geophysical Journal of the Royal Astronomical Society*, 58, 395-430.

Heathershaw A.D. and P.D. Thorne (1985) Sea-bed noises reveal role of turbulent bursting phenomenon in sediment transport by tidal currents. *Nature*, 316, pp 339-342.

Heathershaw A.D. and D.N. Langhorne (1988) Observations of near-bed velocity profiles and seabed roughness in tidal currents flowing over sandy gravels. *Estuarine,, Coastal and Shelf Sciences*, 26, 459-482.

Hinze J.O. (1975) *Turbulence*, 2nd Edition, McGraw-Hill series in Mech. Eng., McGraw-Hill, New York, 618p.

Hoerner S.F. (1965) Pressure Drag, Chapter III. *In Fluid-Dynamic Drag*, Theoretical, Experimental and Statistical Information (2nd edition), Midland Park, p3.1-3.4.

Holt J.T. (1995) *Topographic Influences on Kelvin-Helmholtz instability*, PhD Thesis, Southampton University, 290pp

Huntley D.A. (1988) A modified inertial dissipation method for estimating seabed stresses at low Reynolds numbers, with application to wave/current boundary layer measurements. *Journal of Physical Research*, 18, 339-346.

Jackson R.G. (1976) Sedimentological and fluid dynamics implications of the turbulent bursting phenomenon in geophysical flows. *Journal of Fluid Mechanics*, 77, pp. 531-560.

Jimenez J. and P. Moin (1991) The minimal flow unit in near-wall turbulence. *Journal of Fluid Mechanics*, 225, 213-240.

Kaftori D., G. Hetsroni and S. Banerjee (1994) Funnel-shaped vortical structures in wall turbulence. *Physics of Fluids*, 6(9), 3035-3050.

Kirkbride A. (1993) Observation of the influence of bed roughness on turbulence structure in depth limited flows over gravel beds. In Clifford N.J., French J.R. and Hardisty J. (editors) *Turbulence: Perspective on Flow and Sediment Transport*, John Wiley & Sons Ltd, Chichester, 185-196.

Kline S.J., W.C. Reynolds, F.A. Schraub and P.W. Runstadler (1967) The structures of turbulent boundary layers. *Journal of Fluid Mechanics*, 95, 741-773

Kolmogorov A.N. (1962) A refinement of previous hypotheses concerning the local structure of turbulence in a viscous incompressible fluid at high Reynolds number. *Journal of Fluid Mechanics*, 26, 37-47.

Kolmogorov A.N. (1941) The local structure of turbulence in incompressible viscous fluid for very large Reynolds numbers. *C.R. Acad. Sci.* URSS, 30, 301

Kostaschuk R.A. and M.A. Church (1993) Macroturbulence generated by dunes: Fraser River, Canada, *Sedimentary Geology*, 85, 25-37.

Kostaschuk R.A. and P.V. Villard (1999) Turbulent and sand suspension over dunes: Fraser river, Canada. Sedimentology, 43, 849-863.

Kostaschuk R. (2000) A field study of turbulence and sediment dynamics over subaqueous dunes with flow separation. Sedimentology, 47, 519-531.

Krogstad P.A., R.A. Antonia and L.W.B. Browne (1992) Comparison between rough- and smooth-wall turbulent boundary layers. *Journal of Fluid Mechanics*, 245, 599-617.

Lamb K.G. (1994) Numerical simulations of stratified inviscid flow over a smooth obstacle. *Journal of Fluid Mechanics*, 260, 1-22.

Lanckneus J. and G. De Moor (1995) Bedforms on the Middelkerke Bank, southern North Sea. In Flemming B.W. & A. Bartholoma (editors) *Tidal signatures in modern and ancient sediments*, International Association of Sedimentologists Special Publication. London: Blackwell Science Limited, London, 33-51.

Larsen L.H., R.W. Sternberg, N.C. Shi, M.A.H. Marsden and L. Thomas (1981) Field investigations of the threshold of grain motion by ocean waves and currents. *Marine Geology*, 42, 105-132.

Lawrence G.A. (1987) Steady flow over an obstacle. *Journal of Hydraulic Engineering*, 113(8), 981-991

Lecouturier M., N. Grochoswki, C. Bishop, M. Wilkin, J. Avoine, F. Levoy and M.B. Collins (1998) Measurements of processes at the sediment/water interface, *Hydrodynamics, Biogeochemical processes and fluxes in the Channel*, Fluxmanche II Final Report (MAST II).

Lecouturier M., N.T. Grochowski, A.D. Heathershaw, E. Oikonomou and M.B. Collins (2000) Turbulent and macro-turbulent structures developed in the benthic boundary layer downstream of topographic features, Estuarine, *Coastal and shelf Sciences*, 50, 817-833

Leeder M.R. (1983) On the dynamics of sediment suspension by residual Reynolds stresses – confirmation of Bagnold's theory. *Sedimentology*, 30, 485-491.

Little and Mayer (1976) Stability of Channel Bed by armouring. *Journal of Hydraulic Division*, 102, 1647-1660.

Lou J., T. Wolf and W. Rosenthal (1999) Modeling sediment resuspension in coastal areas. In J. Harff, W. Lemke and K. Stattegger (editors), *Computerized modeling of Sedimentary Systems*, Springer-Verlag, Berlin, 452p, 23-36.

Lumley J.L. (1965) Interpretation of time spectra measured in high intensity shear flows. *Physics of Fluids*, 8, 1056-1062.

Lumley J.L (1972) *A First Course in Turbulence*. H. Tennekes (editor), The MIT Press, Cambridge (USA), 300pp.

Luyten P.J., E. Deleersnijder, J. Ozer and K.G. Ruddick (1996) Presentation of a family of turbulence closure models for stratified shallow water flows and preliminary application to the Rhine outflow region. *Continental Shelf Research*, 16, 101-130.

Martinuzzi R. and C. Tropea (1993) The flow around surface-mounted, prismatic obstacles placed in a fully developed channel flow. *ASME Journal of Fluid Engineering*, 115, 85-92.

McLean S.R, J.M. Nelson and S.R. Wolfe (1994), Turbulence structure over two-dimensional bed forms : implications for sediment transport. *Journal of Geophysical Research*, 99(C6), 12,729-12,747

McLean S.R., J.M. Nelson and R.L. Shreve (1996) Flow sediment interactions in separating flows over bedforms. In *Coherent Flow Structures in Open Channels*, Ashworth P.J., S.J. Bennett, J.L. Best and S.J. McLelland (eds), John Willey and Sons, Chicheser, 203-226.

Mestayer P. (1982) Local isotropy and anisotropy in a high-Reynolds-number turbulent boundary layer. *Journal of Fluid Mechanics*, 125, 475-503.

Ministerie van de vlaamse gemeeschap (1994) Lodingen Uitgevoerd Door Het BEASAC III – Platform, Baggerstortvak Bruggen En Wegen 'S1', Datum van opname 25, 26, 30 Augustus, 6 September 1994, Departement Leefmilieu En Infrastruktuur, Administratie Waterinfrastruktuur En Zeewezen Dienst Der Kusthavens.

Muller A. and A. Gyr (1996) Geometrical analysis of the feedback between flow, bedforms and sediment transport. In *Coherent Flow Structures in Open Channels*, Ashworth P.J., S.J. Bennett, J.L. Best and S.J. McLelland (eds), John Willey and Sons, Chicheser, 237-247.

Nakagawa H. and I. Nezu (1975) Turbulence of open channel flow over smooth and rough beds. *Proceedings of Japanese Society of Civil Engineering*, 241, 155-168.

Nelson J.M. and J.D. Smith (1989) Mechanics of flow over ripples and dunes. *Journal of Geophysical Research*, 94, 8146-8162.

Nelson J.M., S.R. McLean and S.R. Wolfe (1993) Mean flow and turbulence fields over 2-dimensional bed forms. *Water Resources Research*, 29(12), 3935-3953.

Nelson J.M., R.L. Shreve and S.R. McLean (1995) Role of near-bed turbulence structure in bed-load transport and bed form mechanics. *Water Resources Research*, 31(8), 2071-2086.

Nortek AS (1998) *ADV Operation Manual*, Vollend (Norway).

O'Connor B. (1996) *Circulation and sediment Transport around Banks.* CSTAB Handbook and Final Report (MAST II): Volume 2, University of Liverpool.

Paola C. (1985) A method for spatially averaging small-scale bottom roughness. *Marine Geology, 66: 291-301.*

Pedinotti S., G. Mariotti and S. Banerjee (1992) Direct numerical simulation of particle behaviour in the wall region of turbulent flows in horizontal channels. *International Journal of Multiphase Flow*, 18, 927-941.

Pond S. (1965) *Turbulence Spectra in the Atmospheric Boundary Layer over the Sea.* PhD Thesis, University of British Columbia, Vancouver, B.C., Canada, 175pp.

Prandtl L. (1925) Uber die ausgebildete Turbulenz. Z. *Angew. Math. Mech.*, 5, 136-139.

Reynolds O. (1883) *Philosophical Transactions of the Royal Society*, 174, 935 (Papers on mechanical and Physical Subjects, 2, 51).

Robinson S.K. (1991) Coherent Motions in the turbulent boundary layer structure. *Annual Review of Fluid Mechanics*, 23, 601-639.

Rodi W. (1984) Turbulence models and their application in hydraulics. *International Association for Hydraulic Research*, 2nd edition, Delft, Netherland.

Saddoughi S.G. and S.V. Veeravali (1994) Local isotropy in turbulent boundary layers at high Reynolds number. *Journal of Fluid Mechanics*, 268, 333-372.

Sechet P. (1996) *Contribution à l'Etude des Structures Cohérentes en Turbulence de Paroi. De leur Influence sur le Transport des Sédiments dans le Cas du Charriage.* Thèse, Université de Toulouse, 203p.

Sechet P. and B. Le Guennec (1999) Bursting phenomenon and incipient motion of solid particles in bed-load transport. *Journal of Hydraulic Research*, 37(5), 683-696.

Shields A. (1936) Application of similarity principles and turbulence research to bed-load movement. *Mitt. Preuss. Versuchs. Wasserbau Schiffbau*, California Inst. Tech., W.M. Keck Lab of Hydraulics and Water Resources, Berlin, Rept No 167, 36p.

Simpson J.H, W.R. Crawford, Rippeth, A.R. Campbell and J.V.S. Cheok (1996) The vertical structure of turbulent dissipation in shelf seas. *Journal of Physical Oceanography*, 26(8), p.1579-1590.

Smith C.R., J.D. Walker, A.H. Haidari and U. Sobrun (1991) On the dynamics of near-wall turbulence. *Philosophical Transactions of the Royal Society of London*, A336, 131-175.

Smith J.D. (1993) Use of 'kernel' experiments for modelling near-wall turbulence. In R.M.C. So, C.G. Speziale and B.E. Launder (editors) *Near Wall Turbulent Flows*, Elsevier Science Publishers, Hemisphere, New York, 248-267.

Smith J.D. (1996) Coherent flow structures in smooth-wall turbulent boundary layers: facts, mechanisms and speculation. In P.J. Ashworth, S.J. Bennett, J.L. Best and S.J. McLelland (editors) *Coherent Flow Structures in Open Channels*, John Wiley and Sons Ltd, Chichester, 1-39.

Soulsby R.L. (1980) Selecting record length and digitization rate for near-bed turbulence measurements. *Journal of Physical Oceanography*, 10, 208-219.

Soulsby R.L. and K.R. Dyer (1981) The form of the near bed velocity profile in a tidally accelerating flow. *Journal of Geophysical Research*, 86(C9), 8067-8074.

Soulsby R.L. and J.D. Humphery (1990) Field observations of wave-current interaction at the sea bed. In *Water Wave Kinematics*, A. Torum and O.T. Gudmestad (editors), Kluver Academic Publishers, The Netherlands, 413-428.

Soulsby R.L. (1977) Similarity scaling of turbulence spectra in marine and atmospheric boundary layers. *Journal of Physical Oceanography*, 7, 934-937.

Soulsby R.L. (1981) Measurements of the Reynolds stress components close to a marine sand bank. Marine Geology, 42, 35-47.

Soulsby R.L., 1983, *The bottom boundary layer and shelf seas*, Elsevier, Amsterdam, 189-266.

Soulsby R.L., R. Atkins and A.P. Salkield (1994) Observations of the turbulent structure of a suspension of sand in a tidal current. *Continental Shelf Research.*, 14, 4, 429-435.

Soulsby R.L., A.P. Salkield and G.P. Le Good (1984) Measurements of the turbulence characteristics of sand by a tidal current. *Continental Shelf Research*, 3(4), 439-454.

Stips A., H. Prandke and T. Neumann (1998) The structure and dynamics of the bottom boundary layer in shallow sea areas without tidal influence: an experimental approach. *Progress In Oceanography*, 41, 383-453.

Sumer B.M. and R. Deigaard (1981) Particle motions near the bottom in turbulent flows in an open channel, Part 2. *Journal of Fluid Mechanics*, 109, 311-337.

Sutherland A.J. (1967) Proposed mechanism for sediment entrainment by turbulent flows, *Journal of Geophysical Research*, 72, 191-198.

Tennekes H. (1973) The logarithmic wind profile. *Journal of Atmospheric Sciences*, 30, 234-238.

Thorne P.D., J.J. Williams and A.D. Heathershaw (1989) *In situ* acoustic measurements of marine gravel threshold and transport. *Sedimentology*, 36, 61-74.

Thornton E.B. (1979). Energetics of breaking waves within the surf zone. *Journal of Geophysical Research*, 84, 4931-4938.

Tomlinson B.N. (1993) *Erosion Studies of Mixed Sand Beds under the Combined Action of Waves and Currents*, unpublished PhD Thesis, University of Southampton, 267pp.

Townsend A.A. (1976) *The structure of turbulent shear flow*, 2nd edition, University Press, Cambridge, 429pp.

Townsend A.A. (1980) The response of sheared turbulence to additional distortion, *Journal of Fluid Mechanics*, 81, 171-191.

Trowbridge J.H. (1998) Notes and correspondence : On a technique for measurement of turbulent shear stress in the presence of surface waves, *Journal of Atmospheric and Oceanic Technology*, 15, 290-298.

van Rijn L.C. (1993) *Principles of Sediment Transport in Rivers, Estuaries and Coastal Seas*, Acqua Publications, The Netherlands, various pagination.

Wei T. and W.W. Willmarth (1991) Examination of v-velocity fluctuations in a turbulent channel flow in the context of sediment transport. *Journal of Fluid Mechanics*, 223, 241-252.

Wiberg P.L. and J.M. Nelson (1992) Unidirectional flow over asymmetric and symmetric ripples, *Journal of Geophysical Research*, 97, 12745-12761.

Williams J.J., P.D. Thorne and A.D. Heathershaw (1989) Measurements of turbulence in the benthic boundary layer over a gravel bed, *Sedimentology*, 36, 959-971.

Williams P.B. and P.H. Kemp (1971) Initiation of ripples on flat sediment beds, *Journal of Hydraulic Division of the American Society of Civil Engineers*, 97, 133-145.

Wyngaard J.C.and S.F. Clifford (1977) Taylor's hypothesis and high-frequency turbulence spectra, *Journal of Atmospheric Sciences*, 34, 922-929.

Yalin M.S. (1972) *Mechanics of Sediment Transport*. Pergamon Press, Oxford, 298pp.

Yung P.K., H. Merry and T.R. Bott (1989) The role of turbulent burst in particle re-entrainment in aqueous systems. *Chemical Engineering Science*, 44(N4), 873-882.

Zhou J., R.J. Adrian, S. Balachandar and T.M. Kendali (1999) Mechanisms for generating coherent packets of hairpin vortices in channel flow. *Journal of Fluid Mechanics*, 387, 353-396.

Annexes

Annexe 1

Lecouturier M.N., N.T. Grochowski, A.D. Heathershaw, E. Oikonomou and M.B. Collins (2000) Turbulent and macro-turbulent structures developed in the benthic boundary layer downstream of topographic features, *Estuarine, Coastal and shelf Sciences*, 50, 817-833

Estuarine, Coastal and Shelf Science (2000) **50**, 817–833
doi:10.1006/ecss.1999.0602, available online at http://www.idealibrary.com on IDEAL®

Turbulent and Macro-turbulent Structures Developed in the Benthic Boundary Layer Downstream of Topographic Features

M. N. Le Couturier[a], N. T. Grochowski[c], A. Heathershaw[b], E. Oikonomou[a] and M. B. Collins[a]

[a]*School of Ocean and Earth Sciences, University of Southampton, Southampton Oceanography Centre, European Way, Southampton SO14 3ZH, U.K.*
[b]*U.K. Defence Research and Evaluation Agency, Southampton Oceanography Centre, European Way, Southampton SO14 3ZH, U.K.*

Received 21 December 1998 and accepted in revised form 23 November 1999

The characteristics and effects of large-scale flow structures developed in the benthic boundary layer downstream from large topographic features were analysed throughout a tidal cycle. The observed signature of the macro-turbulent features consisted of streamwise modules of low horizontal velocity and high suspended sediment concentration (SSC), alternating with modules of high horizontal velocity and low SSC. These modules extended 10 to 20 m streamwise and exceeded 1 m vertically, and are believed to be related to flow separation effects over large bedforms upstream of the deployment site. The macroscale flow modules intensified the 'burst-like' turbulent events and favoured sediment transport. 'Ejection-like' events were magnified during modules of decreasing horizontal velocity and increasing turbidity, whereas 'sweep-like' events were magnified during modules of increasing horizontal velocity and decreasing SSC. The enhanced turbidity of the macroscale modules may be the result of enhanced upward diffusion of sediment by ejection events, whereas the low-turbidity modules may be induced by increased downward transport of suspended sediment by sweep events. These hypotheses were supported by cross-spectral analysis performed on velocity and suspended sediment concentration time-series recorded at the site. An enhanced (negative) contribution of outward and inward interaction events to the Reynolds stress, compared to those reported in uniform BBLs, resulted in 'abnormally' low stress values.

Keywords: turbulence; macro-turbulence; bedform; bursting; sediment; transport; Reynolds stress; boundary layer

Introduction

The occurrence of coherent structures in the near-bed turbulent flow over smooth and rough seabeds has been known for some time (Grass, 1971). These turbulent flow structures consist of small-scale vortices which are associated with the formation of elongated streaky patterns of high speed downward flows and low-speed upward flows. These streaks induce bursting events which are responsible for seabed sediment movements and, eventually, sediment ejection into the outer flow (Sutherland, 1967; Sumer & Deigaard, 1981; Garcia *et al.*, 1996).

Large-scale flow structures usually occur in the presence of large bedforms. Kondrat'ev *et al.* (1959) observed that the periodicity of macro-turbulent features in the water column matched the wavelength of dunes present at the seabed. The authors inferred that dunes are formed by large eddies occurring naturally within the flow. Later, a more complex mechanism was suggested, whereby bedforms and flowstructures interact with each other in a 'feed-back' loop, with bedform geometry determining the 3-D flow field, while flow structures control and enhance bedform shapes (Jackson, 1976; Heathershaw & Hammond, 1980; Muller & Gyr, 1996). These ideas indicate that understanding the turbulent and macroturbulent coherent structures of the flow is critical to the prediction of suspended sediment and bedload transport (Heathershaw, 1974; Jackson, 1976; Heathershaw & Thorne, 1985). The mechanisms involved in the control of macroscale structures, however, together with the detailed characteristics of the complex wake-flow generated behind obstacles, are still a matter of controversy (Richards *et al.*, 1992).

The present work describes small-scale and large-scale flow structures in a benthic boundary layer influenced by large bedforms. An insight into

[c]Deceased.

0272–7714/00/060817+17 $35.00/0

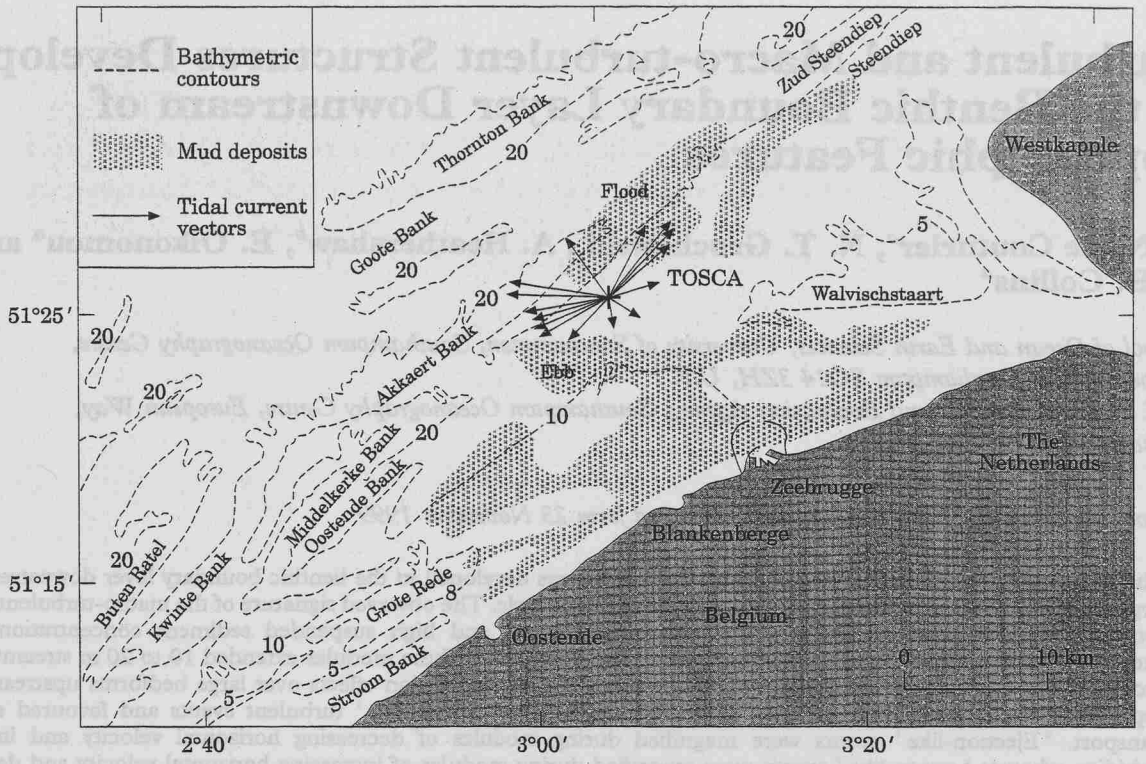

FIGURE 1. General bathymetry of the Flemish Bank System off the Belgium coasts and location of the deployment site of TOSCA (September 1994); the arrows indicate the magnitude and directions of the mean currents throughout a tidal cycle.

their effects on the turbulent processes and sediment transport in such environments is provided and the possible generation mechanisms of the observed patterns are also discussed.

Area under investigation

The benthic instrumented platform TOSCA (transport of sediment under the combined action of waves and currents) was deployed approximately 10 km offshore in the Flemish Bank area (southern North Sea) (51°25.81N, 3°5.02E), in a mean water depth of 11 m (Figure 1). Grain size analysis of the top 3 cm of Reinech box-corer samples collected at the deployment site and 1 km to the north, east, west and south of the site revealed that the seabed consisted of homogeneous fine to medium size sand (median grain diameter of 220 μm). A detailed echo-sounder bathymetric survey and a side-scan survey were carried out prior to deployment to determine seabed roughness. Three 1-km long transects orientated north–south and separated by 150 m (side-scan sonar range) were surveyed with the side-scan sonar around the site; the echo-sounder survey extended 3 by 9 km around the deployment site. (Figure 2). These surveys indicated that the seabed was flat over an area of at least 500 m around the TOSCA deployment site; further away, the seabed was covered by bedforms of various scales. A field of sand dunes (approx. 1·5 m high and 100 m long) was present 1 km to the NW of TOSCA and numerous smaller bedforms (0·3 to 1 m high and 0·5 to 3 m long) were distributed around the investigated site. Three km to the south was the navigational channel for the Zeebrugge port and 4 km to the W-NW of the TOSCA site, a large swale (13 m deep and 2 km wide approx.) lay along the SE flank of the Akkaert Bank. To the north-west and west, a series of sand banks, typically 30 km long, 10 to 20 m in height and 1 to 2 km in width, formed the Flemish Bank system. Hydrodynamic models (O'Connor, 1996) and Synthetic Aperture Radar (SAR) images (Figure 3) have provided evidence that during spring tides separation of the tidal currents occur over the bedforms of the area. These flow structures are thought to result in bedload and suspended sediment transport processes which are critical for sandbank maintenance (O'Connor, 1996).

The deployment took place during spring tide (5 m tidal range), when tidal currents reached speeds of 0·70 m s^{-1} at 1·2 m above the seabed. The wind was weak (~4·5 to 5 m s^{-1}) and blew seawards (180°N)

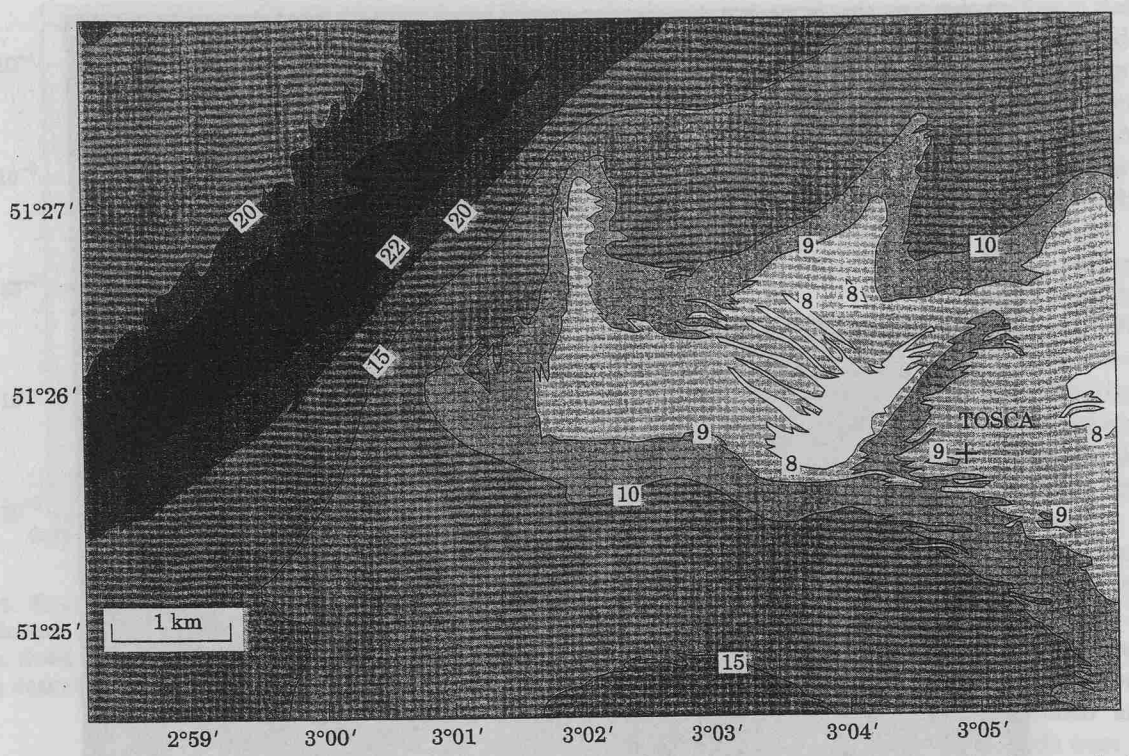

FIGURE 2. Detailed bathymetry of the area surrounding TOSCA deployment site (after Ministerie van de Vlaamse Gemeeschap, 1994).

so the waves were generally small (significant wave height H_s <0·40 m). No significant resuspension of the underlying sandy sediment (i.e. above the height of the lowest suspended sediment concentration (SSC) measurements at 0·35 m above the seabed) was observed during the deployment period. These measurements agree with the observations of Lanckneus and De Moor (1995) who found that even during peak tidal flows sand resuspension events were rare and, even when they occurred, were limited to heights below 0·15 m above the seabed. The Optical Back-Scatter (OBS) sensors, however, recorded the presence of a significant level of fine-grained sediment in the water column. This appeared to have been re-suspended from adjacent muddy deposits which was advected across the measurement site by tidal currents (Le Couturier *et al.*, 1998).

Methods and results

BBL measurements

The benthic platform TOSCA simultaneously recorded at 5-Hz, time-series of horizontal current velocity and direction at 0·35 m, 0·78 m and 1·20 m above the seabed, vertical current speed at 0·78 m above the seabed, and suspended sediment concentration (SSC) at all three heights. Simultaneous high-frequency measurements of water pressure (from which sea surface elevation was derived) were also obtained at z=1·8 m above the bed. Sea surface elevation time-series were obtained by correcting the water pressure records for depth attenuation using the frequency-dependent correction of Earle and Bishop (1984). The current velocities were measured using two spherical (5·5 cm diameter) and two annular (11·5 cm diameter) electromagnetic current meters (EMCM) (Series 800, Valeport Marine Scientific). Water pressure was measured by a TransInstruments BHL-4250 pressure transducer and SSC records were obtained using three D&A OBS sensors. The measurements were recorded in hourly bursts of 30 min duration throughout a tidal cycle (15 h). This sampling regime provided a complete set of data for the analysis of both the turbulent and macroscale tidal flow patterns.

Preparation of the time series

Estimation of turbulent flow parameters in shallow water shelf environments is subject to the possible contamination of the turbulent velocity field by wave orbital velocities (Grant & Madsen, 1986;

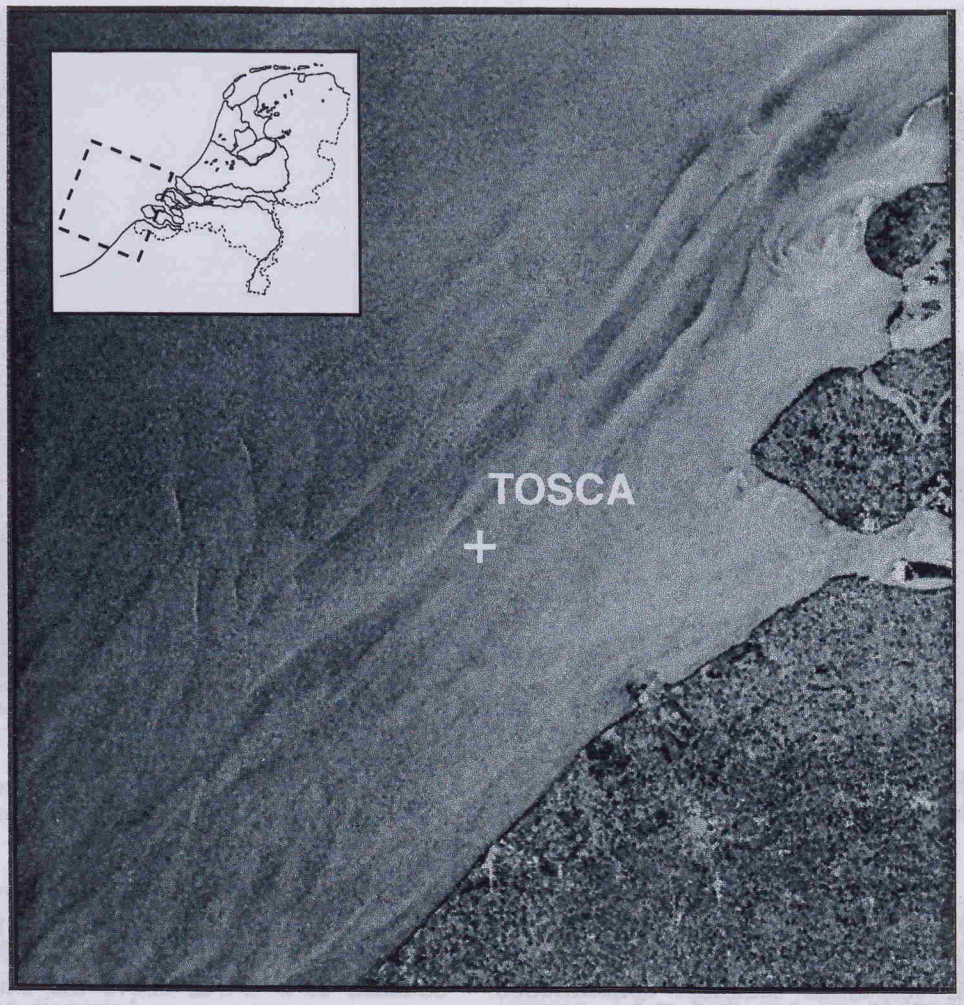

FIGURE 3. Synthetic Aperture Radar (SAR) image of the area around the experimental site (orbit 16034, frame 2565, date 9/8/94). The image shows the presence of linear sea surface macroturbulent features (white bands) above the sandbanks generated by the interaction between the tidal flow and the sandbanks. The white linear bands on the image are related to enhanced sea surface roughness generated by flow/topography interaction processes.

Trowbridge, 1998). Indeed, wave orbital velocities may have similar scales and intensities as those the turbulent velocity fluctuations. Here, contamination of the near-bed flow by waves was believed to be negligible, due to the small surface waves (H_s<0·40 m and T<6 s) and the relatively strong tidal currents. This was confirmed by spectral energy plots of total velocity fluctuations (Figure 4) and Reynolds stress (Figure 5), which showed that energy in the turbulence velocity and Reynolds stress fields at the wave frequencies were small. Nevertheless, it was decided to apply the linear filtration technique of Thornton (1979) to remove any wave contributions before computing the turbulent parameters. This technique separates total-velocity spectra ($E_u(f)$) into turbulent ($E_{u'}(f)$) and wave-driven ($E_w(f)$) components, by using co-located measurements of sea surface elevation (ζ)(or water pressure) and current velocity. The wave-component spectrum is defined as that part of the spectra that is in coherence with the sea surface elevation fluctuations (Equation 1), while the turbulent component is defined as the incoherent part and is retrieved using Equation 2. This equation assumes that waves approach the mean flow at a right angle. This was true during the flood phase of the tide, but during the ebb phase, the wave approach was around 45° to the current direction. Hence, the effectiveness of the filtration technique during the ebb period is probably limited.

$$E_w(f) = \gamma_{u,\zeta}^2(f) E_u(f) \quad (1)$$

$$E_u(f) = E_w(f) E_{u'}(f) \quad (2)$$

where $\gamma_{u,\zeta}$ is the coherence function between ζ and u.

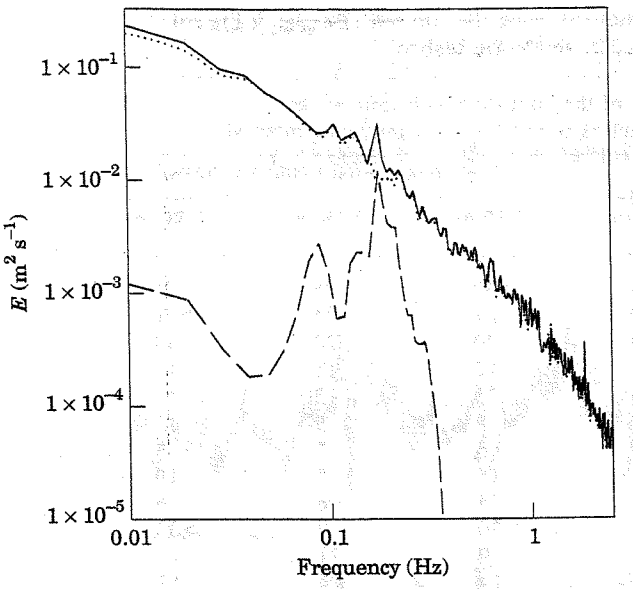

FIGURE 4. Energy spectra of total (unfiltered) and turbulent (wave-filtered) horizontal velocity fluctuations and of water pressure. Solid line: unfiltered velocity; dotted line: filtered velocity; dashed line: water pressure.

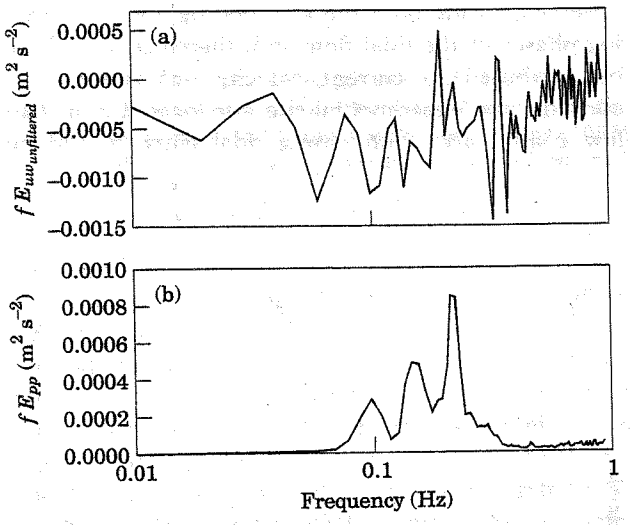

FIGURE 5. Energy spectra of (a) Reynolds stress and (b) water pressure, based on simultaneous measurements of velocity and water pressure.

Figure 4 illustrates the removal of the narrow wave-related energy peak in the velocity spectra using this technique. The filtration of wave contributions removed about 9% of the total turbulent kinetic energy (TKE). The averaged TKE value over the deployment period was about 32 m^2 s^{-2} when wave-induced fluctuations were included, and 29 m^2 s^{-2} when wave fluctuations were removed (see ' Estimation of turbulence parameters ', below).

In the present study, the turbulent flow is described using mean and variance quantities, auto- and cross-correlation functions and probability density functions, which require stationary time-series (Bendat & Piersol, 1971). This means that the time Δt over which the quantities are estimated and averaged should (a) exceed the time scale of the turbulence to include a statistically significant number of the Reynolds stress contributing events, (b) be representative of the mean flow and (c) be short enough not to include trends such as tidal variations. Previous studies have shown that Δt is in the order of 8–12 min in tidal flows (e.g. Soulsby, 1980). Stationarity of the time-series has been tested here by applying a run test (Bendat & Piersol, 1971) which enables the determination of the shortest record length where trends in the mean root-mean-square (rms) velocities can be detected. Since it can be considered that any non-stationarity of interest can be revealed by non-stationarity in the rms values (Bendat & Piersol, 1971), it is not necessary to test the stationarity of any other estimates. The run test has been applied to each time-series of 30 min for the mean and rms parameters. The 30 min velocity records were divided into 30 s intervals over which mean velocities and rms velocities were averaged; this resulted in two time-series of 60 estimates spanning a period of 30 min. The run test was then applied to sub-series of 5 to 30 min duration using a 1 min step. The results of the test (Table 1) showed that the shortest record length Δt to be non-stationary is highly variable (from 5 min to periods exceeding 30 min) although most of the stationary record length exceeded 11 min (in 33 cases out of 45). The frequency of occurrence of each stationary record length (from 5 to 30 min) was computed for all bursts and parameters; this showed that the most common stationary records lengths were 6 and 10 min (in 42 out of 45 records).

Based on the above information, it was decided that each 30 min time-series would be divided into three sub-series of 10 min for the computation of the mean and turbulent parameters.

Evidence of flow separation processes behind bedforms

Sea surface signatures of flow interactions with topographic features. SAR images of the area around the deployment site (Figure 3) showed the presence of elongated patches of enhanced sea surface roughness above the sandbanks. The increased sea surface roughness over the bedforms resulted in enhanced radar back-scatter and appears as white bands on the images (Figure 3). These features reveal that strong interaction processes are taking place between the tidal flow and

TABLE 1. Shortest non-stationary record length computed using the run test (Bendat & Piersol, 1971) for the three measuring heights (0·35, 0·78 and 1·20 m above the seabed)

	Duration (in min) of the stationary sub-time series with the following parameters tested (at 5% confidence interval)					
	Mean velocity (U) (with trend)			Root mean square velocity (urms)		
Burst no.	0·35 m	0·78 m	1·20 m	0·35 m	0·78 m	1·20 m
1	30	29	29	>30	28	28
2	22	25	>30	21	25	>30
3	20	14	14	20	20	14
4	12	12	11	12	11	11
5	25	15	24	23	15	15
6	10	5	13	9	5	13
7	5	7	5	5	7	5
8	18	5	18	18	5	19
9	24	6	6	24	6	6
10	>30	8	>30	>30	8	>30
11	9	21	9	9	21	10
12	14	15	17	14	16	17
13	20	28	>30	20	>30	>30
14	13	13	24	13	13	24
15	>30	15	>30	>30	15	>30

the sandbanks. Such signatures were particularly evident during spring tides, which occurred during the experiment.

Vertical velocity structure. The vertical profile of mean horizontal velocity is logarithmic in Bottom Boundary Layers (BBLs) where the flow is steady and unidirectional, and where the seabed is flat and has a uniform distribution of roughness elements (Heathershaw & Langhorne, 1988; Soulsby & Dyer, 1981). The vertical velocity profile at the study site departed significantly from this behaviour during most of the tidal cycle. When the current was flowing towards directions within the section NW–SW (approx. 50% of the time, Figure 1), the velocity profile displayed a downward curvature when plotted on a semi-logarithmic graph of log z versus $U(z)$ (Figure 6). On a few occasions (approx. 20% of the time), when the current was flowing towards opposite directions (i.e. E to NE), the velocity profile displayed an upward curvature (Figure 6). Non-logarithmic velocity profiles may occur for a variety of reasons: (a) unsteadiness in the flow velocity (Soulsby & Dyer, 1981), (b) presence of internal waves (Adams *et al.*, 1990), (c) flow stratification (Green *et al.*, 1990), (d) heterogeneous distribution of bottom roughness (Paola, 1985; Heathershaw & Langhorne, 1988 or (e) presence of large bedforms associated with flow separation and eddy shedding (Hoerner, 1965; Adams *et al.*, 1981). Downward curvature in vertical velocity profiles was observed during both the accelerating and decelerating phases of the tidal flow and, therefore, could not be attributed to current velocity unsteadiness. In addition, the experimental site was located in a shallow coastal area with strong tidal currents and no

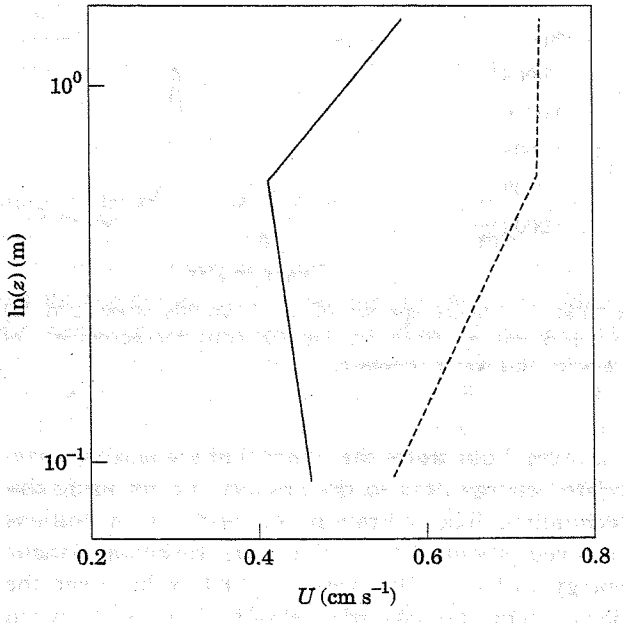

FIGURE 6. Vertical profiles of mean horizontal velocity typical for the ebb phase of the tide (3 h after high water, solid line) and the slack water period (2 h after low water, dashed line).

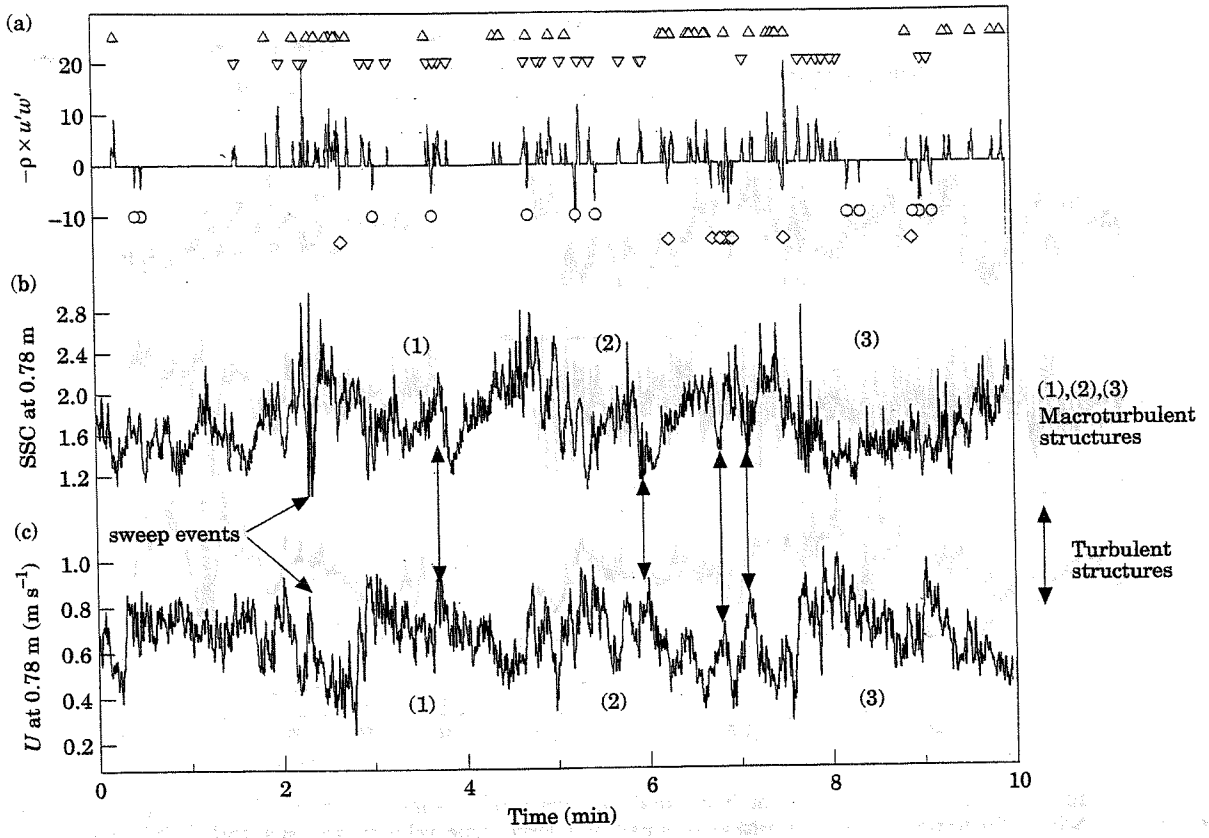

FIGURE 7. Typical time-series for ebb and flood tide of SSC (b) and horizontal velocity (c) showing the occurrence of macroturbulent structures. (a) The major bursting events detected within the $\rho \times u'w'$ time-series using the method of Gordon and Witting (1977) and modified by Soulsby (1983). The symbols indicate the types of bursting event corresponding to each peak. △: ejections, ▽: sweeps; ○: outward interaction; ◇: inward interaction.

major freshwater inputs. Such conditions are associated with high vertical mixing which do not allow sufficient stratification of the water column to support internal waves. The curvature in the vertical velocity profiles was more likely the result of flow separation behind the large bedforms present upstream of the deployment site. As the flow separates over the lee-side of the bedforms, wake vortices are generated, which may be advected with the mean flow to some distances downstream of the bedforms.

Description of the macroscale coherent structures

The SSC and velocity time-series were characterized by distinct small-scale (turbulent) and large-scale (macroturbulent) modules of low velocity/high SSC and high velocity/low SSC. Figures 7 and 8 illustrate the occurrence of such structures during peak ebb tide. To analyse the turbulent and macroturbulent features contained in the records, each wave-filtered time-series was separated into a turbulent and a macro-turbulent time-series. The turbulent time-series of horizontal and vertical velocity (u' and w' respectively) and of suspended sediment concentration (ssc'), were obtained by filtrating the wave-filtered velocity and SSC time-series (u, w and ssc) using a high-pass elliptic filter, with a cut-off frequency F_{cut} of 0·03 Hz. Similarly, the macroturbulent times-series (u_{macro}, w_{macro} and ssc_{macro}), containing the macroturbulent flow structures information, were obtained by filtration of the time-series using a low-pass elliptic filter (f_{cut}=0·03 Hz). The cut-off frequency of the filters was derived from the observation of the auto-correlation functions of the total horizontal velocities. It was chosen as the inverse of the time-lag value at the first zero-crossing of the auto-correlation functions, defining the approximate extent of the principal large-scale eddies (Figure 9).

The temporal scale of the small (turbulent) and large (macro-turbulent) flow structures and the relationships between velocity magnitude and SSC within these modules, were determined using the cross-correlation functions of the turbulent and

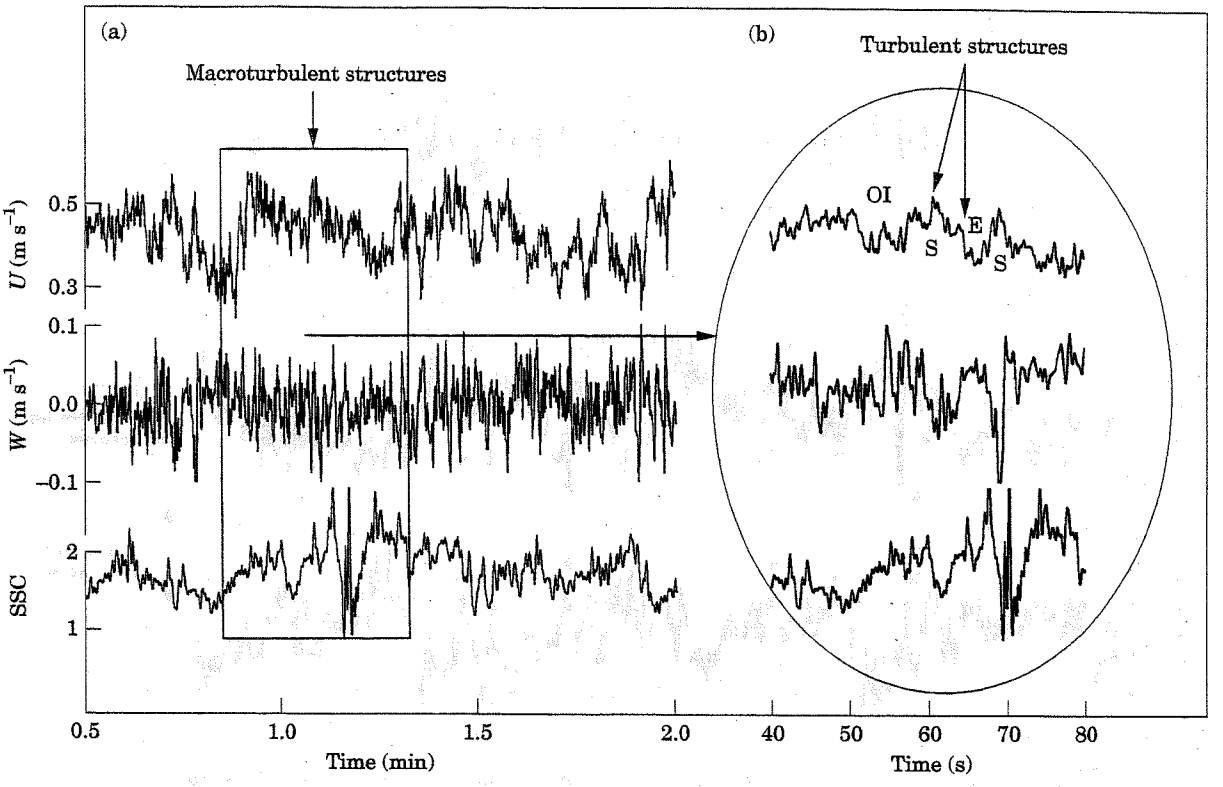

FIGURE 8. Examples of TOSCA time-series of horizontal and vertical velocities (U and W) and suspended sediment concentrations (SSC), illustrating the superposition of small and large-scale velocity and suspended sediment structures within the flow. (b) shows the occurrence of turbulent structures (bursting events), within the macroturbulent structure shown in (a). The letters, OI, E and S refer to outward interaction, ejection and sweep events, respectively, characterized by upward high velocity turbid waters, low velocity upward turbid waters, and downward low velocity clear waters respectively. No units were attributed to the SSC time-series because of the uncertainty in the nature of the suspensions and, thus, in the calibration of the OBS. The same vertical axis scales are used for the right-hand and left-hand graphs.

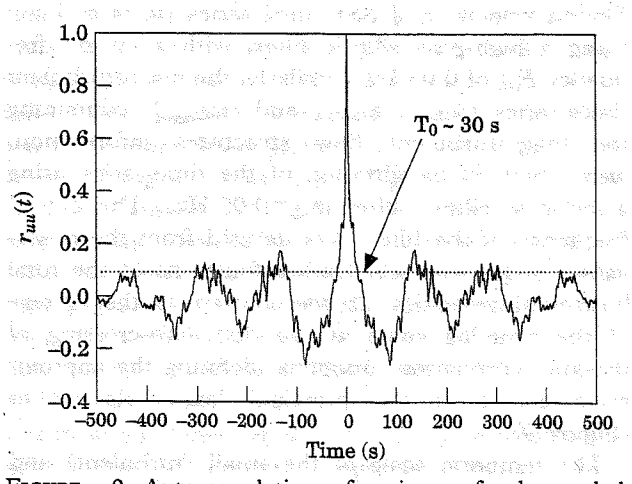

FIGURE 9. Auto-correlation function of de-trended horizontal velocity showing the first zero-crossing (T_0) used to define the limit between the background (high-frequency) turbulence and larger-scale (macro-turbulent) flow structures.

macro-turbulent SSC and velocity time-series. Typical plots of the cross-correlation functions of the macroturbulent variables (u_{macro}, w_{macro} and ssc_{macro}) are shown in Figure 10(a–c), whereas examples of the turbulent cross-correlation functions are shown in Figure 10(d–e). Analysis of these functions showed that similar velocity and suspended sediment concentration signatures exist within both the turbulent and the macro-turbulent structures. Firstly, both the turbulent and macro-turbulent cross-correlation curves are characterized by oscillating tails, which reflect the quasi-periodical occurrence of the turbulent and macro-turbulent flow structures within the flow. Secondly, the cross-correlation functions of u_{macro} and ssc_{macro}, and u' and ssc' are both negative at zero time-lag and show that high turbidity is related to low horizontal velocity and low turbidity to high velocity, in both the large and small flow structures. Similarly, the negative correlation between vertical and horizontal velocities [Figure 10(e–f)] demonstrates that low speed modules are mostly associated with positive

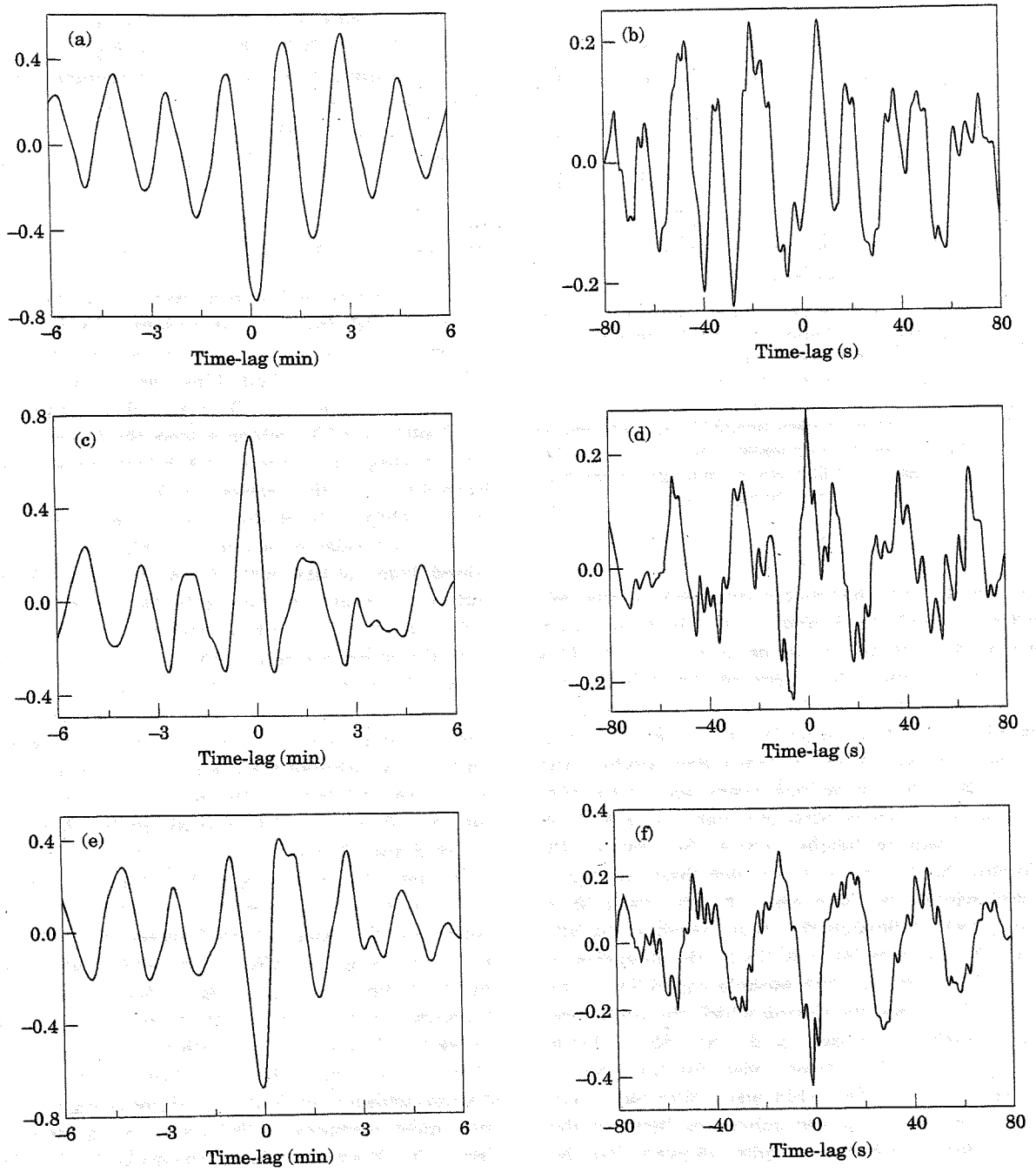

FIGURE 10. Cross-correlation functions of the turbulent and macro-turbulent components of the time-series of horizontal velocity and vertical velocity ($r_{u'-w'}$ and $r_{umacro-wmacro}$ respectively), vertical velocity and SSC ($r_{ssc'-w'}$ and $r_{sscmacro-wmacro}$), and horizontal velocity and SSC ($r_{ssc'-u'}$ and $r_{sscmacro-umacro}$). The positive or negative sign of the functions at zero time lag determines whether the variables vary ' in phase ' or ' out of phase ' respectively, and the oscillations in the curves reflects the periodicity in the oscillations of the variables. The time-series were recorded at a height of 0·78 m above the seabed. (a) $r_{sscmacro-umacro}(t)$; (b) $r_{ssc'-u'}(t)$; (c) $r_{sscmacro-wmacro}(t)$; (d) $r_{ssc'-w'}(t)$; (e) $r_{umacro-wmacro}(t)$; (f) $r_{u'w'}(t)$.

vertical velocities, whereas high speed flows tend to be associated with negative vertical velocities. Positive (upwards) velocity is also associated dominantly with increasing SSC and *vice versa* [Figure 10(c, d)]. The positive correlation between ssc' and w', together with the negative correlation between ssc' and u' [Figure 10(a and d)] suggest that ' ejection-like ' events ($u'<0$ and $w'>0$) increase suspended sediment concentration, while ' sweep-like ' events ($u'>0$ and $w'<0$) decrease it.

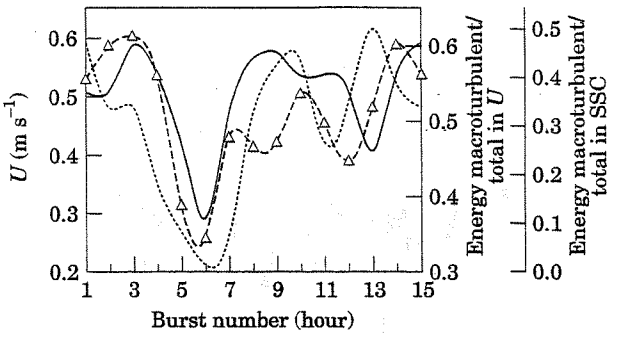

FIGURE 11. Variation in the percentage of energy contained within the low frequency band (macroturbulence band) in the SSC and horizontal velocity time-series during a tidal cycle. The macro-turbulent energy was calculated by integrating the power spectra of SSC and U over the frequency band ($0<F<0{\cdot}03$ Hz), which was divided by the total energy contained throughout the frequency range ($0<F<2{\cdot}5$ Hz). Dotted line: U mean; solid line: energy macroturbulent/total in U; dashed line with triangles: energy macroturbulent total in SSC.

The signals of the macro-turbulent structures, recorded at 0·35, 0·78 and 1 2 m above the bed, display a high vertical coherence (around 0·80). This shows that the macroturbulent structures extended at least 1 m vertically. The macro-scale structures appeared usually in a particular sequence. At first, a downward high speed low turbidity flow module was observed as a sharply defined event associated with increasing horizontal velocity and decreasing SSC at all three measuring heights above the seabed. By multiplying the time scale over which these structures extended within the time series by the mean flow velocity, it was estimated that these modules usually extended 10 to 20 m horizontally in the direction of the flow. This low turbidity module was followed by an intermediate module, during which the horizontal velocity slowly decreased and the SSC slowly increased for 10 to 30 m streamwise. An upward flow of low speed and more turbid water then occurred. The time-lags for maximum coherence between the SSC recorded at different heights, showed that the structures had an inclination of approximately 60° from the vertical.

These events were frequent during peak ebb and flood tide periods but became more intermittent and weaker during slack water. The percentage of energy contained within the low frequency band of the macroturbulent structure ($f<0{\cdot}03$ Hz) was related strongly to the mean tidal current velocity (Figure 11).

Bursting events and coherent structures

The four types of bursting events (ejection, sweep, outward and inward interactions, Table 2) were detected in each velocity time series recorded at 0·78 m above the seabed. This was achieved using the method of Gordon and Witting (1977) and modified by Soulsby (1983), which selects the bursting events by retaining the most predominant peaks in the Reynolds stress time series ($-\rho u'(t)w'(t)$), until their sum reaches 90% of the total Reynolds stress. The type of each selected event $-\rho u'w'_{peak_i}$ is then determined from the sign of the u' and w' values (Table 2) and its duration is calculated by following the (maximal) $-\rho u'w'_{peak_i}$ value backward and forward in time, until the stress value decreases to 10% of its peak value. The bursting events detected were plotted with the macro-turbulent velocity time-series (Figure 8). These plots reveal that the bursting events were not randomly distributed temporally, but that their distribution was related to the macro-turbulent velocity features. Ejection and inward interaction events occurred mainly within macroscale modules of low horizontal velocity and high SSC (Figure 8), whereas sweep and outward interaction events appeared primarily during macro-scale features of high horizontal velocity and low SSC. The percentages of each bursting event type occurring during periods of low macroscale velocity was calculated for each burst (Table 2). These results confirm that most sweeps (65%) and outward interaction events (65%) occurred within macro-scale modules of high velocity, while most ejections (67%) and inward interaction events (70%) occurred within macro-scale modules of low horizontal velocity. The mean durations of ejection and sweep events were both estimated to be

TABLE 2. Percentages of occurrence of the four bursting events during macro-scale module of high horizontal velocity ($U_{macro}>0$) (the values are averaged burst-percentages over the deployment period). The percentages occurring during low velocity macro-scale modules being the complements to 100% of those shown in the Table

Bursting event	Ejection $u'<0, w'>0$	Sweep $u'>0, w'<0$	Outward interaction $u'>0, w'>0$	Inward interaction $u'<0, w'<0$
% occurrence during $U_{macro}>0$	33% (± 7)	65% (± 11)	65% (± 10)	30% (± 8)

TABLE 3. Average stress contribution to $<\rho u'w'>$ of the four bursting events, calculated from all the time-series collected at a height of 0·78 m above the seabed offshore of Zeebrugge. The results are compared with the data obtained by Heathershaw and Thorne (1985) over a gravel bed, and by Soulsby *et al.* (1994) over a sandy seabed covered by small sand dunes (bedform height $H<1$ m)

Type of event	TOSCA data (present study)	Soulsby *et al.* (1994)	Heathershaw and Thorne (1985)
	Reynolds stress contributions		
Ejections	73·80%	60%	50·00%
Sweeps	69·90%	56%	50·90%
Outward interactions	−29·90%	−15%	−5·28%
Inward interactions	−26·80%	−11%	−5·57%

around 10 s; this duration decreased during periods of low mean velocity (down to 4–5 s). The duration of the inward and outward interaction events varied between 2 and 4 s and appeared to be independent of the macro-scale structures and tidal phase.

The results show a larger contribution from negative Reynolds stress contributing events (i.e. the outward and inward interactions) than those reported by other researchers in areas of flat seabed with small roughness elements (i.e. gravel and small sand dunes respectively, Table 3) (Heathershaw & Thorne, 1985; Soulsby *et al.*, 1994). It is interesting to note that the larger bedforms present at the measurement site of Soulsby *et al.* (1994), compared to those found in the study area of Heathershaw & Thorne, (1985), also led to higher values in the inward and outward interactions contributions to the total Reynolds stress. The increased participation of negative stress events (outward and inward interactions) in relation to that of the positive events (sweeps and ejections) reduced the Reynolds shear stress values to 60% of the values calculated using other methods based on the turbulent energy or on the mean flow velocity (i.e. inertial dissipation, turbulent kinetic energy (Huntley, 1988) and Larson *et al.* (1981) methods). Abnormally low Reynolds stress values were also measured by McLean *et al.* (1996) in separated flows: however, these authors explained this particularity by a decrease in the correlation between the vertical and horizontal velocities.

Estimation of turbulence parameters

Turbulence processes control the rate of horizontal and vertical diffusion in the tidal shear flow. To predict the general circulation pattern and the dispersion of material in the ocean, it is therefore essential to know the turbulence characteristics of the flow. Turbulent processes occur mainly at eddy sizes which are comparable with the Kolmogorov mixing length-scale: $L=\nu^{3/4}\,\varepsilon^{-1/4}$, where ν is the kinematic viscosity coefficient and ε is the energy dissipation rate (Soulsby, 1983). It is difficult, if not impossible, (Pedlovski, 1988), to describe vertical and horizontal mixing in numerical models at the level of individual turbulent events that contribute to such processes. Instead, mixing and diffusion are parameterized in the so-called 'turbulence closure schemes'. These schemes parameterize the rate at which the mean flow energy is diffused in turbulent fluctuations throughout the water column and the rate at which this turbulent energy is dissipated (Luyten *et al.*, 1996). The most commonly used method is the k–l closure scheme, which is based upon the determination of the turbulent kinetic energy (k) and the mixing length parameter (l). Such schemes do not appear to perform well in complex flows, such as at the sea surface where waves are present (Blumberg & Mellor, 1987) or near a sea-bed of complex topography (Ly, 1991). A second type of turbulent closure scheme (k–ε) uses expressions for the turbulent kinetic energy and the energy dissipation rate ε. This type of model appears to accurately represent the processes occurring near an irregular seabed or at a rough sea–air interface and is increasingly used (Ly, 191).

These models perform best when they are calibrated using *in situ* measurements of the different turbulence quantities involved: the turbulent kinetic energy, ε, and the scales of turbulent velocity fluctuations and dissipation. These quantities were estimated at the measurement site using the velocity time-series recorded by TOSCA. Their values are presented below and are discussed in relation to the flow and topographic characteristics of the site. These estimations were performed to determine whether the turbulence parameters of the flow, where large-scale flow structures were present, differed from those of typical uniform BBL flows which are commonly used in

TABLE 4. Tidally averaged variances and turbulence intensities of horizontal and vertical velocity measured off the Belgian coasts at 13 m depth (Sept '94)

z (m)	$(\overline{u'^2})^{1/2}$ (m s^{-1})	$(\overline{v'^2})^{1/2}$ (m s^{-1})	$(\overline{w'^2})^{1/2}$ (m s^{-1})	$(\overline{u'^2})^{1/2}/U \pm$ SD	$(\overline{w'^2})^{1/2}/U \pm$ SD
0·35	0·062	0·045		0·14 ± 0·02	
0·78	0·061	0·049	0·029	0·13 ± 0·02	0·062 ± 0·014
1·20	0·065	0·045		0·11 ± 0·01	

models. The horizontal and vertical velocity variances ($\overline{u'^2}$, $\overline{v'^2}$, $\overline{w'^2}$), which reflect the energy contained in the 3-D velocity field were computed by integrating the power spectra of u', v' or w' using Parseval's theorem (Equation 3):

$$(\overline{u'^2})^{1/2} = \left(\int_0^{F_N} S_{u'}(f)\, df \right)^{1/2} \tag{3}$$

where $S_{u'}(f)$ is the frequency energy spectrum of u' and F_N is the Nyquist frequency (F_N=half the sampling frequency).

The estimated variances are shown in Table 4. As usually observed in uniform BBL flows, the variances were homogeneous with depth.

The turbulent intensities of horizontal and vertical velocities ($(\overline{u'^2})^{1/2}/U$ and $(w'^{1/2})^{1/2}/U$) were also calculated for each burst. Despite some discrepancies, the turbulent intensity level was similar throughout the tidal cycle, but increased towards the bed, with mean $(u'^2)^{1/2}/U$ value increasing from 0·11 at z=1·20 m above the bed to 0·14 at z=0·35 m. Such values are within the range measured by Bowden (1962) over a firm sandy bottom, which is comparable to the seabed in the present study (Bowden's op. cit.) $u'^{2^{1/2}}/U$ values increased from 0·12 at z=1·25 m to 0·14 at z=0·50 m in depth of 12 to 22 m). These values are much higher than those found by Bowden and Howe (1963) over a smooth muddy sea-bed ($u'^{2^{1/2}}/U \approx 0{\cdot}06$ at z=0·50 m in approx. 15 m water depth), suggesting that larger seabed roughness increases turbulence intensity of the overlying flow.

The total turbulent kinetic energy level (TKE) was calculated using the 3-D velocity measurements obtained at 0·78 m above the bed (Equation 4).

$$\text{TKE} = \frac{1}{2} \quad \overline{u'^2} + \overline{v'^2} + \overline{w'^2} \tag{4}$$

TKE values varied between 12×10^{-4} m^2 s^{-2} (when the current velocity U was at its lowest: U=0 30 m s^{-1}) and 43×10^{-4} m^2 s^{-2} (when the current velocity was maximal: U=0 65 m s^{-1}), with a mean value of 29×10^{-4} m^2 s^{-2}. These measurements are comparable with those of Soulsby and Humphrey (1990) in similar mean current velocities. The length-scales of the eddies containing most of the flow energy were determined from the wavenumber spectra of ' total ' horizontal velocity fluctuation (u), calculated using detrended wave-filtered horizontal velocity time-series to which no high-pass or low-pass filtrations were applied. Two examples of typical spectra for the flood-ebb period and ' slack-water ' period are plotted in Figure 12(a) and (b), respectively. The spectral energy peaks demonstrate that during ebb and flood periods most of the turbulent energy was contained in features 8 to 10 m long. Interestingly, these values are close to those estimated above by multiplying the time-scale of the macro-scale modules (derived visually from the velocity and SSC time-series) by the concomitant mean current speed. During ' slack-water ' periods, these large eddies had lost most of their energy (small spectral energy at large wave-numbers) and smaller length-scale features were prevalent (spectral energy maxima were within wavelengths of 1 to 4 m).

Finally, the turbulent energy dissipation rates ε were estimated at each measuring height throughout the

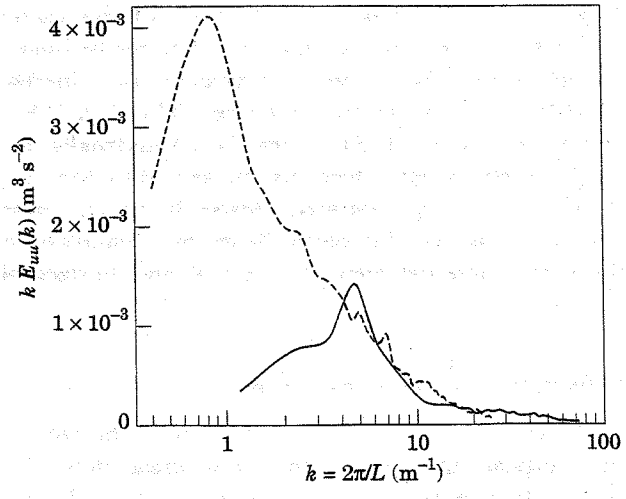

FIGURE 12. Wavenumber spectra of horizontal velocity time-series recorded during peak ebb tidal flow and during low slack water. Solid line: slack water; dashed line: ebb/flood.

TABLE 5. Energy dissipation rates measured in a variety of marine environments

Authors	Area	z (m)	ε (W m^{-3})
TOSCA data (this study)	Off Belgium (13 m depth)	0·35	0·054
		1·20	0·040
Heathershaw (1979)	Irish Sea	1·00	0·063
		1·50	0·057
Dewey *et al.* (1988)	Off Vancouver island (135 m depth)	0·32	$7{\cdot}7 \times 10^{-4}$
		0·49	$2{\cdot}6 \times 10^{-4}$
		0·65	$1{\cdot}1 \times 10^{-4}$
		2·82	3×10^{-5}
	Hecate Strait (35 m depth)	15–50	$3–5 \times 10^{-3}$
		>50	1×10^{-3}
Simpson *et al.* (1996)	Irish Sea Mixed: 50 m	near bed	0·1–0·2
		mid-water	0·001
	stratified: 90 m	near bed	0·03
		mid-water	1×10^{-6}

tidal cycle, using Equations (5) and (6). Equation (5) is valid only for wavenumbers included in the inertial sub-range ($k_{min} \leq k \leq k_{max}$) (where production equals dissipation). The range of wavenumbers [k_{min} k_{max}] was determined by (a) selecting the range of wavenumbers over which the spectral energy of u' decreases as $k^{-5/3}$ (determined visually from the wavenumber spectra) and (b) by plotting the selected ε values against k and selecting the range of k values where ε remains constant.

$$\varepsilon_k = \left(\frac{S_{u'}(k) k^{5/3}}{A\alpha} \right)^{3/2} \quad \text{with } k_{min} \leq k \leq k_{max} \qquad (5)$$

$$\varepsilon = \overline{\varepsilon_k}, \text{ for } k_{min} \leq k \leq k_{max} \qquad (6)$$

where $S_u(k)$ is the 1-D energy density spectrum of u', k is the wavenumber, $k = 2\pi f / U$ with U the mean current velocity and f the corresponding frequency, and $A = 18/55$, $\alpha = 1{\cdot}44$ (Grant *et al.*, 1962).

The wavenumbers used for the estimation of ε were also limited by the resolution of the current-meters; they had to be included within the wavenumbers [k_{low} k_{sup}], where k_{low} corresponds to the largest size of eddies observable and is controlled by the height of the sensor z and the length of the record T, whereas k_{sup} (the smallest size of eddies observable) is controlled by the size of the sensor head D, and the sampling frequency F_s (Soulsby, 1983). The values of turbulent energy dissipation ε obtained at 0·35 m and 1·20 m above the sea-bed are 0·054 and 0·040 Wm^{-3} respectively, which are typical of near-bed flows in shallow uniform BBL (Heathershaw, 1979; Simpson *et al.*, 1996) and are much higher than values reported for deeper waters (Dewey, 1988; Simpson *et al.*, 1996) (Table 5). The length scale of the eddies at which the turbulent energy is dissipated via molecular viscosity forces can be estimated from the inertial dissipation rate using Equation (7). Mean values of l equal to $0{\cdot}45 \times 10^{-3}$ m at a height of 0·35 m and $0{\cdot}48 \times 10^{-3}$ m at a height of 1·20 m were estimated

$$l = \nu^{3/4} \varepsilon^{-1/4} \qquad (7)$$

where ν is the kinematic viscosity coefficient, $\nu = 1{\cdot}3 \times 10^{-6}$ m^2/s.

Discussion: nature and significance of the coherent structures

The macro-turbulent structures observed in this study are attributed to flow separation effects in the lee of large bedforms present upstream from the deployment site, which lead to large-scale vortical motions in the flow [Figure 13(a)]. The large-scale coherent structures appear to have been advected across the flat sandy bed of the TOSCA site by the tidal flow. Along the vortex lines of these flow structures, instabilities develop which transport low horizontal speed fluid upwards, while 'scour loops' are created which transport high horizontal speed fluid downwards [Figure 13(b)]. The intense turbulent processes and strong upward velocities associated with the macro-scale turbulence may explain the discolouration of near surface waters in shallow tidal environments while the higher turbidity of the macro-turbulent modules can be explained by either coherent resuspension events occurring in the separation zone where the large eddies are formed, or from the lifting of turbid bottom water by the low-speed upward flows.

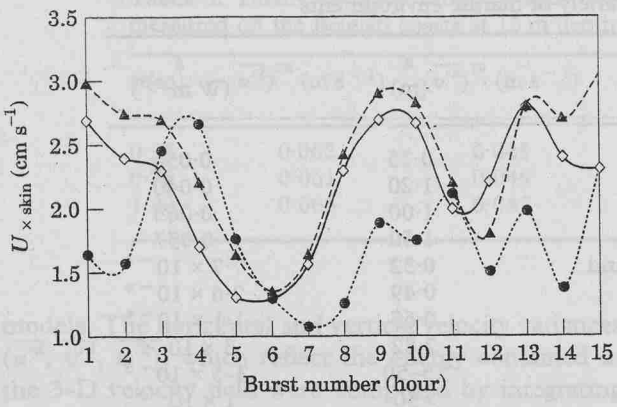

FIGURE 13. Variation of skin friction velocities calculated from TOSCA measurements (Zeebrugge, September 1994), using the Reynolds stress method, Larsen *et al.* (1981)'s model and the Turbulent Kinetic Energy method. Solid/diamond line: Larsen *et al.* (1981)'s model; dashed/triangle line: turbulent kinetic energy; dotted/circle line: Reynolds stress.

Material is then held in suspension by the strong upward velocities associated with the macroturbulent modules. Muller and Gyr (1996) and Kostaschuk and Villar (1996) proposed similar mechanisms to explain the observed SSC and velocity fluctuations (ranging from tens of seconds to several minutes) in separated flows over dunes.

The capacity of the flow to erode the sea-bed material was estimated by calculating the skin friction velocity using the Reynolds stress method, TKE method and Larsen *et al.* (1981)'s model. Since the seabed at the TOSCA site was flat, the skin friction is expected to be similar to the total friction velocity. In this study, the contribution of the different bursting events to the Reynolds stress differed significantly from values reported in the literature for uniform BBL. Ejection and sweep events dominated the Reynolds stress production almost equally, in contrast with the observations of Krogstad *et al.* (1992) who identified the dominance of sweep events over rough beds. Of potentially more importance, the participation of the inward and outward interaction events were enhanced, which led to a reduction in the Reynolds stress values during peak ebb flow and during most of the flood phases of the tide. During these periods, the Reynolds stress values were lower than the shear stress values estimated using bulk flow methods (e.g. Larsen *et al.*, 1981) or values derived from turbulence closure scheme models (e.g. TKE method) (Figure 14). In the Reynolds stress approach, the frequency of outward interaction events in the BBL is inversely related to the magnitude of the shear stress, although outward interaction events were related to the upward transport of suspended sediment. Since most sediment transport models base their predictions on the shear stress values, it is likely that the Reynolds stress approach would underestimate the transport of suspended sediment in conditions where the contribution of outward interactions are increased. These observations underline the importance of obtaining a detailed knowledge of the turbulence structures of the flow before deriving mean-value parameters of the turbulent velocity fluctuations for the prediction of sediment transport processes. The turbulent and mean structure of a current flowing over a flat bed may be affected significantly by the presence of upstream large-scale bedforms, and the relationships between mean-value parameters of the turbulent velocities, such as Reynolds stress, and sediment transport processes may not apply in the same manner as in ' classic ' uniform flows.

Some aspects of the flow turbulence appear to be unaffected by the presence of eddy structures shed from the bedforms. Indeed, the turbulence intensities, the rate of energy dissipation, and the viscous scales at which turbulent energy is dissipated are similar to the values typically observed in steady uniform flows. This result is consistent with vortex stretching in 3-D turbulent flow fields in which energy is transferred progressively to smaller scales retaining less detail of the mean and larger scale motions. The effect of flow separation processes observed at the TOSCA site therefore appears mainly to be a modulation of uniform BBL turbulence characteristics by macroturbulent eddy structures with horizontal scales from 10–20 m and vertical scales of about 1 m. It is important to note that the values of the turbulence quantities (such as ε, the rate of turbulence energy dissipation) were all estimates from ' bulk ' methods which imply a certain degree of spatial averaging. It is therefore the spatial average of these quantities which appear to remain unchanged compared to those values found in ' classic ' uniform flows. It would be interesting to observe how these turbulence quantities are controlled by the macro-turbulence and turbulence structure of the flows (e.g. whether the energy dissipation rate increases or decreases during the sweep or ejection events of the bursting cycle). The variation of the turbulence properties within the coherent flow structures can be expected to affect significantly the turbulent mixing and transport processes (essentially resuspension and vertical mixing). No studies have yet examined this aspect of the flow dynamics.

The measurements obtained during this study indicate that the macro-turbulent structures influence

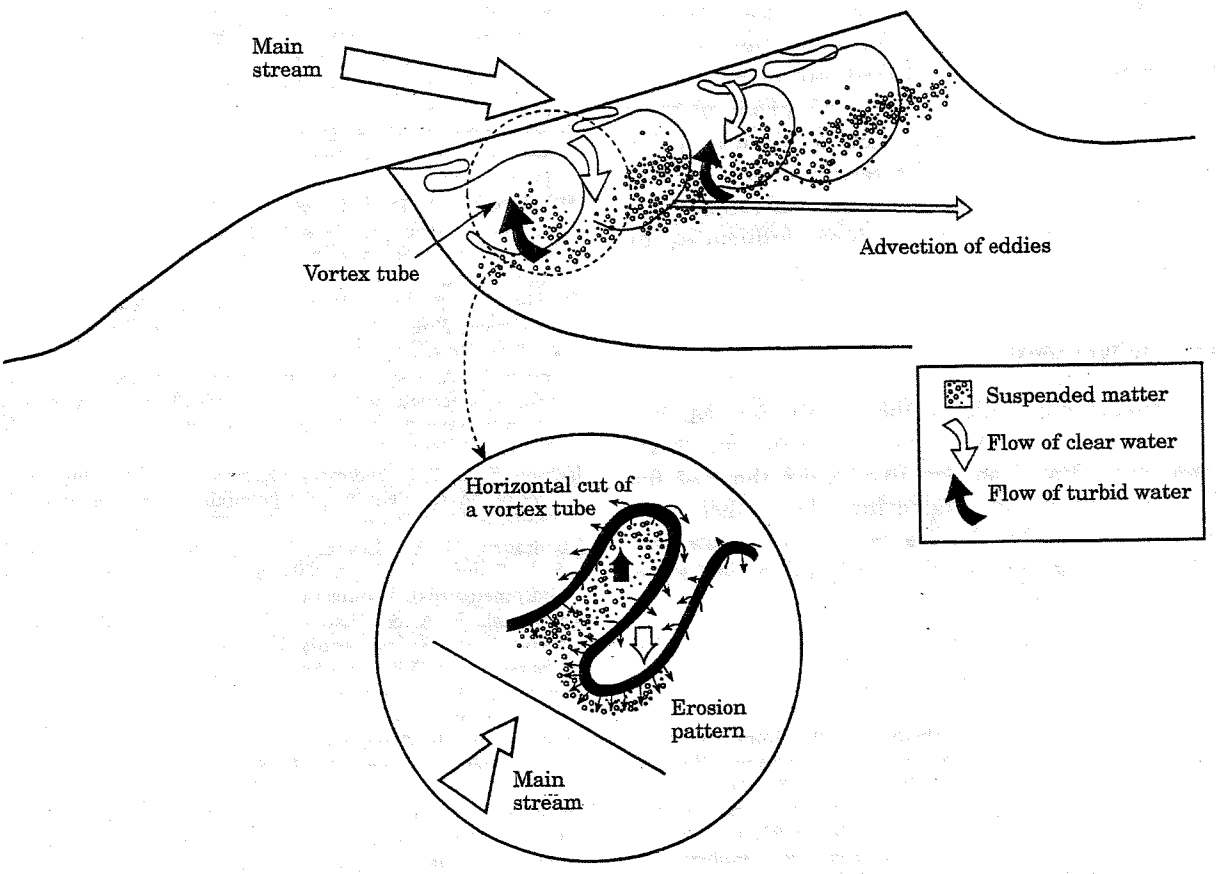

FIGURE 14. (a) Vortical structures generated in the lee region of a large bedform by a tidal flow flowing over it. (b) Horizontal cut of the vortex tube, showing the development of turbulent coherent structures, carrying turbid water upward and clear water downward.

significantly SSC in favouring the suspension of sediments by enhancing upward turbulent flows. However, further studies would be required to provide a satisfactory explanation of this observation.

Conclusions

Measurements obtained using the benthic instrumented platform TOSCA support the view that the turbulent and macroturbulent characteristics of the BBL downstream of large topographic features differ significantly from a uniform BBL and that their effects may extend over large distances downstream of the bedforms. The BBL at the experimental site was dominated by large-scale flow modules of turbid and clear waters which were related to the shedding of vortices resulting from flow separation processes over upstream large bedforms.

The measurements support the hypothesis that small-scale turbulence (at the scale of dissipation) is essentially de-coupled from large-scale motions (mean flow and large scale vortices) and is characterized by turbulent quantities typical of steady uniform BBL flows. The large-scale flow modules were superimposed on a 'background' turbulent flow field, which displayed characteristics typical of uniform BBL flows (i.e. the energy dissipation rates, the scales of the motions at which viscous forces dissipate energy and the turbulence intensity levels were similar to those found in uniform flows). The turbulence associated with the large-scale flow motions was characterized by the enhanced participation of outward interactions, which, by carrying turbid flows upward had a significant impact on the maintenance of sediment in suspension and on the subsequent transport of suspended sediment by tidal currents.

In BBLs influenced by large bedforms the use of eddy correlation or Reynolds shear stress techniques to predict sediment transport may be inadequate. Indeed, such shear stress values may not account for the particular effects of the turbulent flow structures triggered by the macro-scale flow motions mentioned above. It is possible that turbulent processes are not related to bed shear stress and sediment transport

processes by the same relationships as those found in classic uniform BBL flows. The prediction of sediment transport is usually based on extensions of formulae and equations developed for steady uniform flows (Fredsoe, 1982; McLean & Smith, 1986; Nelson & Smith, 1989). The results of our investigations may explain the poor accuracy of estimates of the local sediment fluxes in flows influenced by bedforms.

Acknowledgements

The Management Unit of the North Sea Mathematical Models (MUMM), and, in particular, Brigit Lawaert and Dries Van den Eynde, are thanked for their contribution in organizing the cruise and deployment of TOSCA. We also thank Vera van Lancker for her generous help and Kate Davis for the drawing of the figures.

References

Adams, C. E., George, Jr & Weatherly, L. 1981 Some effects of suspended sediment stratification on an oceanic Bottom Boundary Layer. *Journal of Geophysical Research* **86,** 4161–4172.

Adams, C. E., Wells J. Jr & Park, Y. 1990 Internal hydraulics of a sediment-stratified channel flow. *Marine Geology* **95,** 131–145.

Bendat, J. S. & Piersol, A. G. 1971 *Random Data: Analysis and Measurement Procedures.* Wiley and Sons, New York, 407 pp.

Blumberg, A. F. & Mellor, G. L. 1987 A description of a three-dimensional coastal ocean circulation model. *Journal of Atmospheric Sciences* **25,** 1015–1020.

Bowden, K. F. 1962 Measurements of turbulence near the sea bed in a tidal current. *Journal of Geophysical Research* **67,** 3181–3186.

Bowden, K. F. & Howe, M. R. 1963 Observations of turbulence in a tidal current. *Journal of Fluid Mechanics* **17,** 271–284.

Dewey, R. K., Leblond, P. H. & Crawford, W. R. 1988 The turbulent boundary layer and its influence on local dynamics over the continental shelf. *Dynamics of Atmospheres and Oceans* **12,** 143–172.

Earle, M. D. & Bishop, J. M. 1984 *A Practical Guide to Wave Measurement and Analysis.* ENDECO Inc, U.S.A., 78 pp.

Fredsoe, J. 1982 Shape and dimensions of stationary dunes in rivers. *Journal Hydraulic Division ASCE* **108,** 932–947.

García, N., Niño, Y. & López, F. 1996 Laboratory observations of particle entrainment into suspension by turbulent bursting. In *Coherent Flow Structures in Open Channels.* John Wiley and Sons Ltd, Chichester, pp. 63–86.

Gordon, C. M. & Witting, J. 1977 Turbulent structure in a benthic boundary layer. In *Bottom Turbulence* (Nihoul, J. C. J., ed.). Elsevier, Amsterdam, pp. 59–81.

Grant, W. D. & Madsen, O. S. 1986 The continental-shelf bottom boundary layer. *Annual Review of Fluid Mechanics* **18,** 265–305.

Grant, W. D., Stewart, R. W. & Moillet, A. 1962 Turbulent spectra from a tidal channel. *Journal of Fluid Mechanics* **12,** 241–263.

Grass, A. J. 1971 Structural features of turbulent flow over smooth and rough boundaries. *Journal of Fluid Mechanics* **50,** 233–255.

Green, M. O., Rees, J. M. & Pearson, N. D. 1990 Evidence for the influence of wave-current interaction in a tidal boundary layer. *Journal of Geophysical Research* **95,** 9629–9644.

Heathershaw, A. D. & Thorne, P. D. 1985 Sea-bed noises reveal role of turbulent bursting phenomenon in sediment transport by tidal currents. *Nature* **316,** 339–342.

Heathershaw, A. D. 1979 The turbulent structure of the bottom boundary layer in a tidal current. *Geophysical Journal of the Royal Astronomical Society* **58,** 395–430.

Heathershaw, A. D. 1974 Bursting phenomena in the sea. *Nature* **248,** 394–395.

Heathershaw, A. D. & Hammond, F. 1980 Secondary circulations near sand banks and in coastal embayments. *Dt Hydrogr Z* **33,** 135–151.

Heathershaw, A. D. & Langhorne, D. N. 1988 Observations of near-bed velocity profiles and seabed roughness in tidal currents flowing over sandy gravels. *Estuarine, Coastal and Shelf Sciences* **26,** 459–482.

Hoerner, S. F. 1965 Pressure drag. In *Fluid-Dynamic Drag, Theoretical, Experimental and Statistical Information,* (2nd edition). Midland Park, pp. 3.1–3.4.

Huntley, D. A. 1988 A modified inertial dissipation method for estimating seabed stresses at low Reynolds numbers, with application to wave/current boundary layer measurements. *Journal of Physical Research* **18,** 339–346.

Jackson, R. G. 1976 Sedimentological and fluid dynamics implications of the turbulent bursting phenomenon in geophysical flows. *Journal of Fluid Mechanics* 77, 531–560.

Kondrat'ev, N. E., Lyapin, A. N., Popov, I. V., Pin'kovskii, S. I., Fedorov, N. N. & Yakunin, I. I. 1959 *Channel processes.* Gidrometeoizdat, Leningrad.

Kostaschuk, R. A. & Villar, P. 1996 Turbulent sand suspension events, Fraser River, Canada. In *Coherent Flow Structures in Open Channels.* John Wiley and Sons Ltd, Chichester, pp. 305–319.

Krogstad, P. A., Antonia, R. A. & Browne, L. W. B. 1992 Structure investigation in a turbulent boundary using orthogonal X-wires arrays. In *Proceedings of the 11th International Fluid Mechanics Conference* (Davis, M. R. & Walker, G. J., eds). Hobart, Tasmania, pp. 251–254.

Lanckneus, J. & De Moor, G. 1995 Bedforms on the Middelkerke Bank, southern North Sea (International Association of Sedimentologists Special Publication, 24). In *Tidal Signatures in Modern and Ancient Sediments* (Flemming, B. W. & Batholoma, A., ed.). Blackwell Science Limited, London, pp. 33–51.

Larsen, L. H., Sternberg, R. W., Shi, N. C., Marsden, M. A. H. & Thomas, L. 1981 Field investigations of the threshold of grain motion by ocean waves and currents. *Marine Geology* **42,** 105–132.

Le Couturier, M., Grochoswki, N., Bishop, C., Wilkin, M., Avoine, J., Levoy, F. & Collins, M. B. 1998 Measurements of processes at the sediment/water interface—Hydrodynamics, Biogeochemical processes and fluxes in the Channel. *Fluxmanche II Final Report (MAST II).*

Luyten, P. J., Deleersnijder, E., Ozer, J. & Ruddick, K. G. 1996 Presentation of a family of turbulence closure models for stratified shallow water flows and preliminary application to the Rhine outflow region. *Continental Shelf Research* **16,** 101–130.

Ly, L. N. 1991 An application of the E-ε turbulence model for studying coupled air-sea boundary layer structure. *Boundary Layer Meteorology* **54,** 327–346.

McLean, S. R., Nelson, J. M. & Shreve, R. L. 1996 Flow sediment interactions in separating flows over bedforms. In *Coherent Flow Structures in Open Channels.* John Wiley and Sons, Chichester, pp. 203–226.

McLean, S. R. & Smith, J. D. 1986 A model for flow over two-dimensional bedforms. *Journal of Hydraulic Engineering* **112,** 300–317.

Ministerie van de Vlaanse Gemeeschap 1994 *Lodingen Uitgevoerd Door Het BEASAC III-Platform, Baggerstortvak Bruggen En Wegen 'S1'.* 25, 26, 30 August, 6 September 1994. Departement Leefamilieu En Infrastruktuur, Administratie Waterinfrastruktuur En Zeewegen Dienst Der Kusthavens.

Muller, A. & Gyr, A. 1996 Geometrical analysis of the feedback between flow, bedforms and sediment transport. In *Coherent Flow Structures in Open Channels* (Ashworth, P. J., Bennet, S. J., Best, J. L. & McLelland, S. J., eds). John Wiley and Sons, Chichester, pp. 237–247.

Nelson, J. M. & Smith, J. D. 1989 Mechanics of flow over ripples and dunes. *Journal of Geophysical Research* **94**, 8146–8162.

North Sea Task Force 1993 North Sea Subregion 4, Assessment Report. In *North Sea Quality Status Report 1993 Bilan de santéw de la mer du Nord*. Oslo and Paris Commissions, London, 195 pp.

O'Connor, B. 1996 Circulation and Sediment Transport around Banks. *CSTAB Handbook and Final Report (MAST II), University of Liverpool, Vol. 2*.

Paola, C. 1985 A method for spatially averaging small-scale bottom roughness. *Marine Geology* **66**, 291–301.

Pedlovski, I. 1987 *Geophysical Fluid Dynamics*, 2nd edition. Springer-Verlag, New York, 710 pp.

Richards, K. J., Smeed, D. A., Hopfinger, E. J. & Chabert d'Hieres, G. 1992 Boundary-layer separation of rotating flows past surface-mounted obstacles. *Journal of Fluid Mechanics* **237**, 343–371.

Simpson, J. H., Crawford Impson, W. R., Rippeth, T. P., Campbell, A. R. & Cheok, J. V. S. 1996 The vertical structure of turbulent dissipatation in shelf seas. *Journal of Physical Oceanography* **26**, 1579–1590.

Soulsby, R. L. 1980 Selecting record length and digitization rate for near-bed turbulence measurements. *Journal of Physical Oceanography* **10**, 208–219.

Soulsby, R. L. 1983 *The Bottom Boundary Layer and Shelf Seas*. Elsevier, Amsterdam, pp. 189–266.

Soulsby, R. L., Atkins, R. & Salkield, A. P. 1994 Observations of the turbulent structure of a suspension of sand in a tidal current. *Continental Shelf Research* **14**, 429–435.

Soulsby, R. L. & Dyer, K. R. 1981 The form of the near bed velocity profile in a tidally accelerating flow. *Journal of Geophysical Research* **86**, 8067–8074.

Soulsby, R. L. & Humphrey, J. D. 1990 Field observations of wave-current interaction at the sea bed. In *Water Wave Kinematics* (Torum, A. & Gudmestad, O. T., eds). Kluwer Academic Publishers, The Netherlands, pp. 413–428.

Sumer, B. M. & Deigaard, R. 1981 Particle motions near the bottom in turbulent flows in an open channel, Part 2. *Journal of Fluid Mechanics* **109**, 311–337.

Sutherland, A. J. 1967 Proposed mechanism for sediment entrainment by turbulent flows. *Journal of Geophysical Research* **72**, 191–198.

Thornton, E. B. 1979 Energetics of breaking waves within the surf zone. *Journal of Geophysical Research* **84**, 4931–4938.

Trowbridge, J. H. 1998 Notes and correspondence: On a technique for measurement of turbulent shear stress in the presence of surface waves. *Journal of Atmospheric and Oceanic Technology* **15**, 290–298.

Voulgaris, G., Wilkin, M. & Collins, M. B. 1994 Shingle movement under waves and currents: an instrumented platform for field data collection. In *Coastal Dynamics '94* (Arcilla, A. S., Stive, M. J. F. & Kraus, N. C., eds). American Society of Engineers, New York, pp. 894–909.

Annexe 2

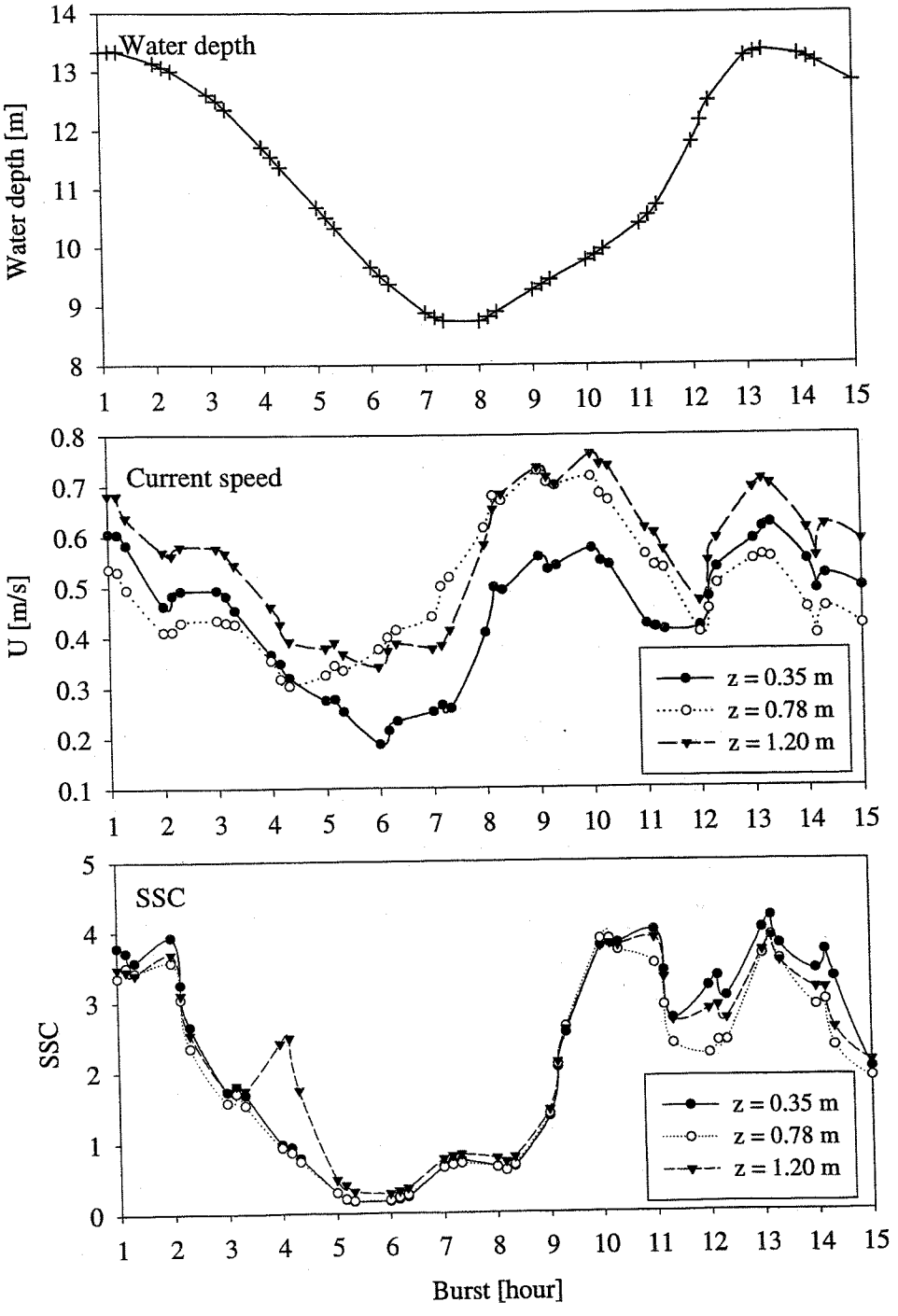

Figure A.1: Tidal variation in mean water depth (a), in mean current speed at 3 heights (b) and in mean SSC (c) at 3 heights. The measurements were collected by TOSCA (7th Sept 94).

Annexe 3

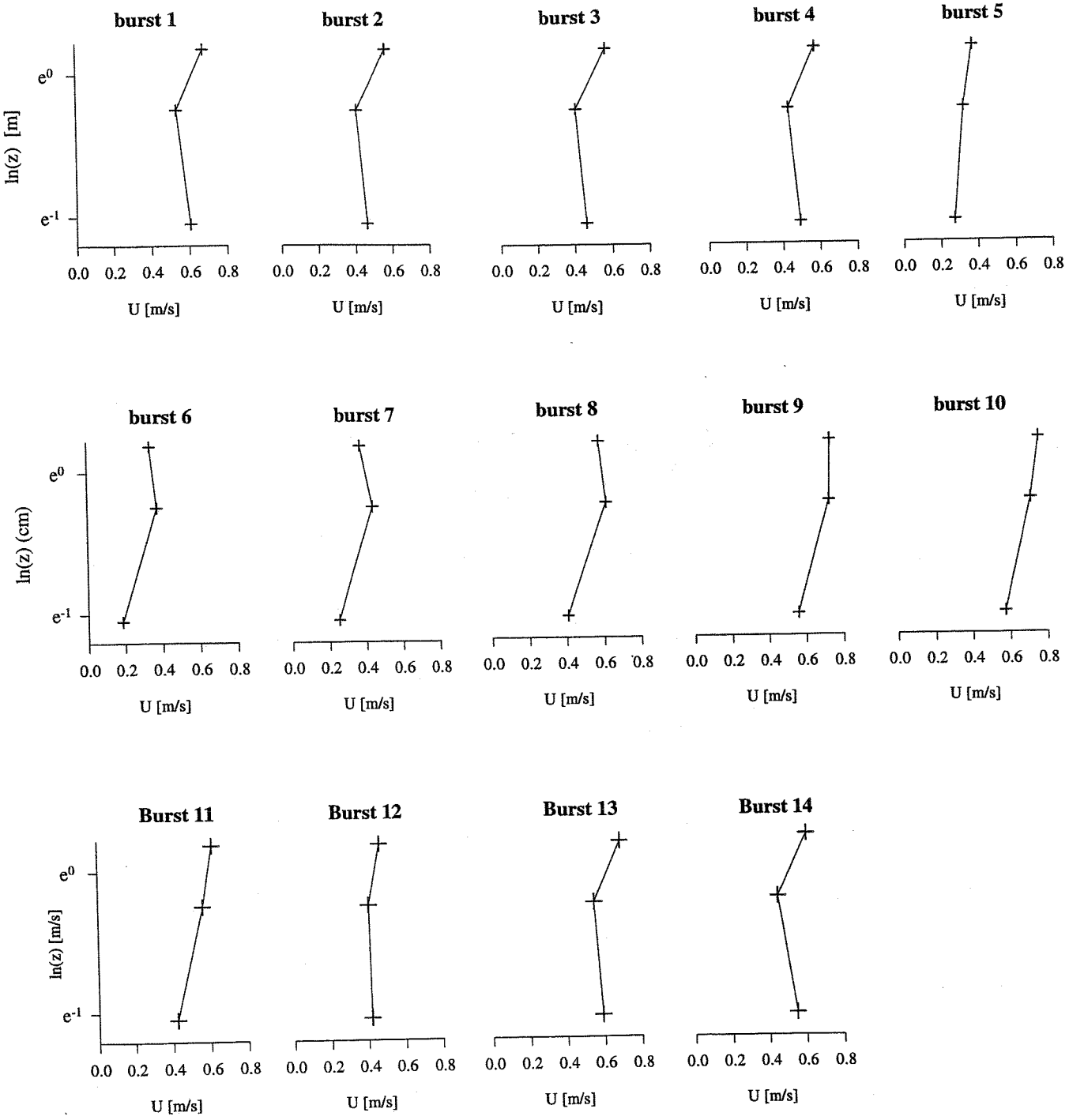

Figure A.2: Vertical profiles of horizontal velocity averaged over the first 10 min of every burst. Each burst is collected every hour (see Annexe 2).

Annexe 4

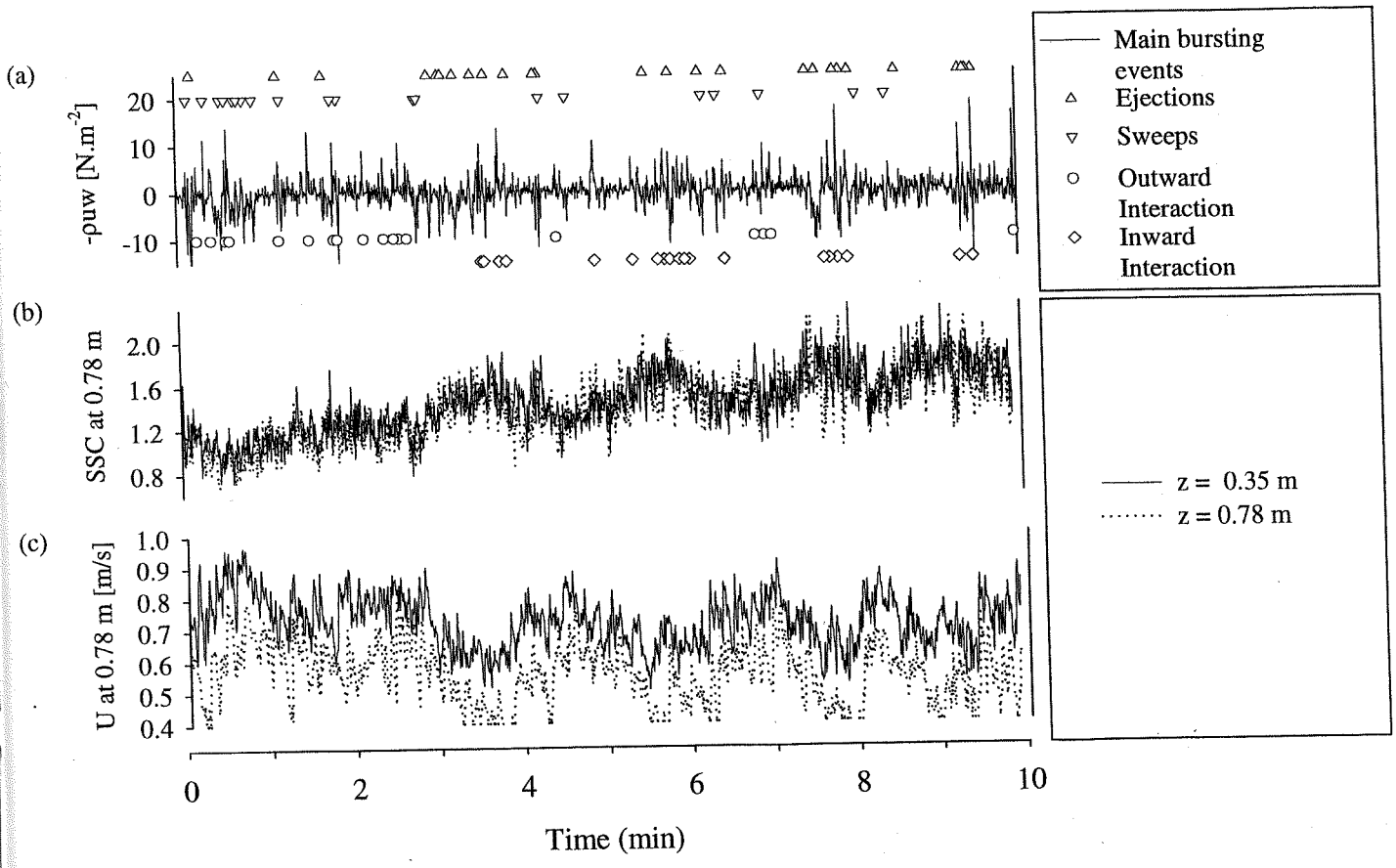

Figure A.3: Time-series of Reynolds stress (a), SSC (b) and horizontal velocity (c) collected 3 hours after low water (flood phase, burst n°9). The symbols indicate the occurrence of the maior bursting events.

Annexe 5

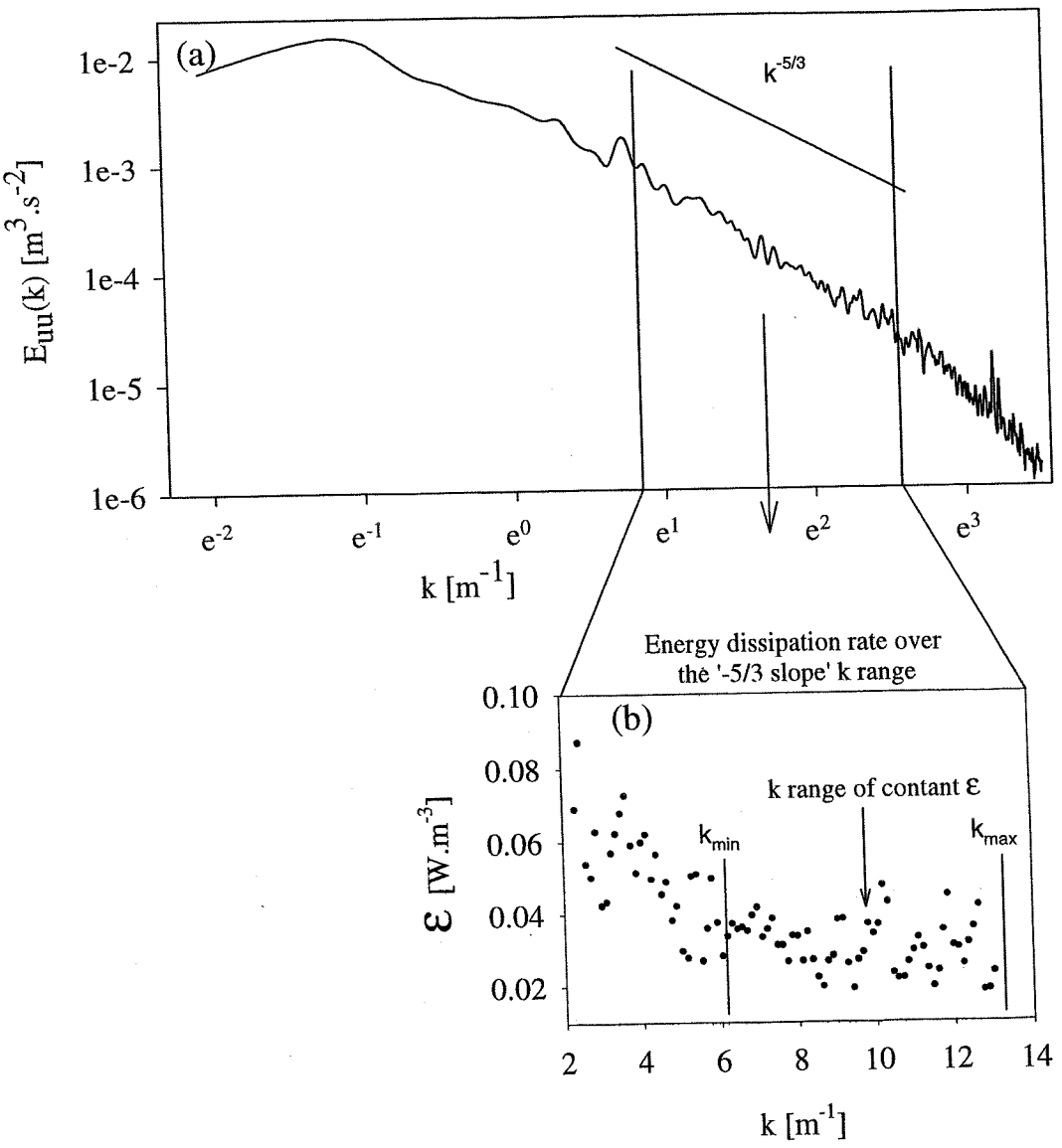

Figure A.4: Example (from burst 3) showing the method used to estimate the energy dissipation rate: (a) Selection of the wavenumber range k over which the velocity spectrum follows a '-5/3' slope; (b) further limitation of the k range used to average ε to the range over which ε remains approximately constant.

Annotations

ν	Kinematic viscosity of water $\nu = 1.3\times10^{-6}$ $m^2.s^{-1}$ at 10°C
H	Height of the bedform
d	Water depth
BBL	Bottom Boundary Layer
δ_{log}	Thickness of the logarithmic layer
δ_{BBL}	Thickness of the BBL
OI	Outward interaction (Bursting event)
II	Inward interaction (Bursting event)
$TKE = \frac{1}{2}\times q^2$	Turbulent kinetic energy per unit of mass
U_∞	Free-stream velocity, which corresponds to the velocity at the top of the BBL
τ	Shear stress (N/m^2 or Pa = 1/10× dynes/cm^2)
τ_0	Bed shear stress
τ_{cr}	Critical bed shear stress for sediment bedload transport
U_∞	Mean velocity of free stream flow (at the top of the BBL)
$\overline{q^2} = \overline{u^2} + \overline{v^2} + \overline{w^2}$	Total turbulent kinetic energy (in $m^2.s^{-2}$)
μ	Dynamic viscosity [$kg.m^{-1}.s^{-1}$]. $\mu = \rho\nu$
ρ	Density of water.
$Re_t = \frac{u_* z}{\nu}$	Turbulent Reynolds number
$Re_{\delta_{BBL}} = \frac{U_\infty \delta_{BBL}}{\nu}$	Flow Reynolds number

SOUTHAMPTON UNIVERSITY LIBRARY

USER'S DECLARATION

AUTHOR: LECOUTURIER, MAGALI TITLE: TURBULENCE AND MARCO-TURBULENCE IN THE BOTTOM BOUNDARY LAYER DOWNSTREAM OF LARGE-SCALE BEDFORMS; IMPLICATIONS FOR SEDIMENT TRANSPORT DATE: 2000

I undertake not to reproduce this thesis, or any substantial portion of it, or to quote extensively from it without first obtaining the permission, in writing, of the Librarian of the University of Southampton.

To be signed by each user of this thesis

DATE	SIGNATURE	ADDRESS